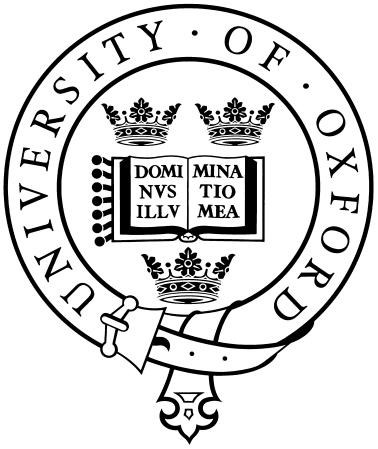
Generation of Uncorrelated Photon-Pairs in Optical Fibres

Offir Cohen
St. Catherine's College, Oxford



Submitted for the degree of Doctor of Philosophy
Michaelmas Term 2009/10

Supervised by
Prof. Ian A. Walmsley

Clarendon Laboratory
University of Oxford
United Kingdom

Abstract

Light, which is composed of discrete quanta, or photons, is one of the most fundamental concepts in physics. Being an elementary entity, the behaviour of photons is governed by the rules of quantum mechanics. The ability to create, manipulate and measure quantum states of light is not only useful in foundational tests of quantum theory, but also in a wide range of quantum technologies – which aim to utilize non-classical properties of quantum systems to perform tasks not possible with classical resources.

Only recently has it been possible to control the properties of number states of light, which have a fixed photon-number. Two-photon states are central to testing fundamental physical theories (such as locality and reality) and the implementation of quantum information technologies. The versatility of photon-pair states is enabled by the potential entanglement properties it can posses. Thus controlling the correlations between photons is crucial to both pure and applied physics.

To produce a single photon, a photon-pair state can be used. Detection of one photon indicates its twin's existence. Many applications, such as optical quantum computation, require pure indistinguishable single photons. Heralding single photons from a photon-pair will, in general, produce single photons in a mixed quantum state due to correlations within the pair.

A common approach to creating photon-pairs is through the nonlinear spontaneous four-wave mixing interaction in optical fibres. This thesis presents a theoretical and experimental implementation of a scheme to tailor the spectral correlations within the pairs. Emphasis is placed on engineering the two-photon state such that they are completely uncorrelated. Spatial entanglement is naturally avoided due to the discrete nature of the optical fibre modes. Spectral correlations are eliminated by careful choice of dispersion characteristics and conditions. The purity of the photons generated by this scheme is demonstrated by means of two-photon interference from independent sources. We measure a purity of $(85.9 \pm 1.6)\%$ with no spectral filtering, exhibiting the usefulness of this source for quantum technologies and applications.

Acknowledgements

First, I would like to thank Prof. Ian A. Walmsley for giving me this great opportunity to join his research group. Working under his supervision acquainted me the most recent research being carried out to date, enhanced my understanding of physics and taught me how to conduct research. His well equipped laboratories, together with his own wisdom and of those he assembled in the research group, provided ideal conditions to carry out novel experiments.

I owe particular thanks to Jeff Lundeen, who provided me with close and practical supervision from the moment I started my studies till he left Oxford. The discussions we had enriched my knowledge and understanding, his ideas and suggestions were crucial for my work, and he taught me everything I needed in order to be able to execute experimental work on my own.

I am grateful to Brian Smith, who took over Jeff's supervision, and gave me advice and help whenever I needed.

I'd like to thank the whole Ultrafast group, who accepted me warmly the moment I arrived in Oxford. This group of people formed a pleasant environment to do research, discuss physics as well as other issues, and also was a great frame for social activities, including drinking, punting, drinking, BBQ, drinking, skiing and more (drinking...). I am particularly thankful to the past and current Photons people: Peter Mosley, Graciana Puentes, Lijian Zhang, Xiaodan Yang, Hendrik Coldensrodt-Ronge and Nicholas Thomas-Peter for helping and discussing problems when I asked for it. I also want to thank those people who started their studies at the same time I did and went with me together the path of first year students: Tobias Witting, David McCabe and Philip Buster. I'd like to add and mention Adam Wyatt, Joshua Nunn, Virginia Lorenz, Klaus Reim, Ben Sussman, KC Lee, Duncan England, Jovana Petrovic, Matthijs Branderhorst and Dane Austin – all found to be very useful for discussions, advice and other help.

Special thanks go to my past housemates: Clare Lobb and Julie Taylor where both great during the year I lived with them. Mathias Rufino, Ralf Schneider and Halim Kusumaatmaja where excellent housemates and are wonderful friends. I am also thankful to all of those friends in Oxford for the pleasant time I had in their company. In addition to those who've already been mentioned, I'd like to specify Méabh Brennan, Stephen Galsworthy, Kristin Lohwasser, Sarah Boddy, Christina Fuhr, Arne Heydorn, Keiko Watanabe and everyone else who contributed to the good time I had in Oxford. I also thank Yachin Ivry, who shared with me fun time as Israelis living in England.

I'm thankful to all my friends in Israel who kept in touch despite the distance, and for making the efforts to meet me whenever I came for a visit. Particularly, I'd like to mention Niv Sinansky, Nir Rozenstock, Areyeh Ben Barak and Alex Derek, as well as the "Technion guys": Tomer Czyzewski, Yonathan Savir, Avi Amar and Nili Habshoosh. I am also pleased to mention the "Weizmann guys": Moti Fridman, Erez Oxman, Shani Sela, Lea Polachek, Michelle Levi and Marija Vucelja.

Last but not least, I want to thank my parents and both sisters for managing to bear me for such a long time.

Thanks everyone – with your support I had a pleasant (yet) useful time!

Contents

1 Introduction **1**

1.1 Overview 1

1.2 2-photon interference 4

1.3 Linear-optics quantum-computation 4

1.4 Single-photon generator 7

1.4.1 Single-emitter photon sources 8

1.4.2 Heralded photons 11

1.5 Thesis outline 18

2 SFWM in fibres **21**

2.1 Nonlinear optics 21

2.2 The quantum-mechanical formalism 23

2.3 The SFWM interaction 28

2.4 The photon-pair state generated in fibres 32

2.5 Spectral filtering to reduce correlations 40

2.6 The step-index model 42

2.7 Phase-matching in fibres 47
2.7.1 Standard silica fibres 48
2.7.2 Photonic-crystal fibres 49
2.8 Practical considerations for choosing a fibre 54
2.8.1 Detection bandwidth 55
2.8.2 Pump 57
2.8.3 Raman background 57
2.8.4 Fibre type 60

3 Factorable photon-pair state 61

3.1 Tailoring the spectral photon-pair properties 61
3.2 Identifying the group-velocity matching point 68
3.3 Altering the phase-matching conditions 71
3.3.1 Phase modulation 71
3.3.2 Polarization modulation instability 73
3.3.3 Effective index-difference 75
3.3.4 Cross phase modulation instability 78
3.4 Bandwidth and fibre length considerations 80

4 Characterizing fibres 83

4.1 Searching for a suitable fibre 83
4.2 Selected fibre: characteristics and model 90

5 Experimental purity demonstration 93

5.1 The HOM interferometer setup 93
5.1.1 Typical HOM setup 95
5.1.2 The setup 99
5.2 Spectral characterization 105
5.3 Results 107
5.3.1 The HOM-interference 107
5.3.2 Normalization 107

6 Effect of experimental parameters 113

6.1 Fibre length 113
6.2 Birefringence fluctuations 115
6.3 Pump power 116
6.4 Pump spectrum 118
6.4.1 Pump wavelength and bandwidth 118
6.4.2 Pump spectral envelope shape 119
6.5 Signal to noise considerations 123

7 Standard fibres 127

7.1 Model 129
7.2 Experimental validation 130
7.3 Factorability in standard fibres 131
7.4 Towards measuring purity 132
7.5 Observation of photon-pairs 136

8 Summary **139**

8.1 Outlook 140

8.1.1 Improving the source 140

8.1.2 Other media – planar waveguides 141

8.1.3 Beyond the single photon 143

8.2 Comparing SFWM with SPDC 147

8.3 Conclusions 149

A The polarization HOM interference **151**

Bibliography **155**

List of Figures

1.1 The anti-bunching effect 3

1.2 The bunching effect 5

1.3 SPDC and SFWM interactions 13

2.1 Typical joint spectral probability 39

2.2 Use of filters to reduce correlations 41

2.3 Step-index fibre 43

2.4 Cross-section image of photonic crystal fibres 50

2.5 Typical dispersion and phase-matching contour in PCFs 53

2.6 Raman scattering 57

2.7 Normalized Raman gain 59

3.1 Examples of factorable states 63

3.2 The horizontal phase-matching case 65

3.3 Optimized purity for given phase-matching angle 66

3.4 Phase-matching and factorability contour in PCFs 70

3.5 Phase-matching contours for various effective index differences . . . 77

4.1 Experimental setup for mapping the phase-matching contour 85

4.2 Typical spectrum of spontaneous generation in PCFs 86

4.3 Observed SFWM wavelengths in various PCFs 87

4.4 Experimental and theoretical phase-matching in the NL-1.8-750 fibre 91

4.5 Factorable joint spectral amplitude with the GV-matching scheme . 91

5.1 A general Hong-Ou-Mandel interferometer setup 96

5.2 Hong-Ou-Mandel interference setup 100

5.3 Dependence of the HOM-interference on purity 105

5.4 Pump and sidebands spectra 106

5.5 Experimental HOM-interference results 108

6.1 Phase-matching contour for longer fibre 114

6.2 Experimental results for longer fibre 115

6.3 Dependence of sidebands spectra on pump power 118

6.4 Calculated joint spectral probability for Gaussian pump spectrum . 120

6.5 Comparison between the theoretical and experimental sidebands spectra 122

7.1 Cross-section of polarization-maintaining standard fibre 129

7.2 Phase-matching in a standard birefringent fibre 131

7.3 Joint spectral amplitude in standard birefringent fibres 132

7.4 Theoretical joint spectral probability for fibre HB800G 134

7.5 HOM setup for standard birefringent fibre 135

7.6 Spectral SWFM gain in standard fiber Fibercore HB800G 137

8.1 Schematic of a planar waveguide 142

List of abbreviations

AHWP	achromatic half-wave plate
APD	avalanche photodiode
BPF	band-pass filter
BS	beamsplitter
BSMF	birefringent single-mode fibre
DM	dichroic mirror
DSF	dispersion shifted fibre
FPGA	field-programmable gate array
FWHM	full-width at half of maximum
FWM	four-wave mixing
GV	group velocity
GVD	group velocity dispersion
HOM	Hong-Ou-Mandel
HWP	half-wave plate
KLM	Knill, Laflamme and Milburn
LOQC	linear-optics quantum-computation
LPF	long-wavelength pass filter
MI	modulation instability
NF	notch filter
PBS	polarizing beamsplitter

PCF	photonic crystal fibre
PMI	polarization modulation instability
PMT	photo-multiplier tube
QWP	quarter-wave plate
SFWM	spontaneous four-wave mixing
SMF	single-mode fibre
SPDC	spontaneous parametric down conversion
SPF	short-wavelength pass filter
SPM	self phase modulation
SMI	scalar modulation instability
XPM	cross phase modulation
XPMI	cross phase modulation instability
ZGVD	zero group velocity dispersion

Chapter 1

Introduction

1.1 Overview

The theory of quantum-mechanics started forming in 1900 when Max Plank proved [1] the ability to solve the black-body radiation paradox by making the assumption that black-bodies emit and absorb radiation in discrete quantities. The energy of these quantities are proportional to the light frequency. Matching his theory with the experimentally observed spectra radiated by black-bodies, he found the (universal) proportionality factor, h, which acquired the title *Planck constant*.

In 1905 Albert Einstein continued this line and published his hypothesis [2] to explain the photoelectric effect: the electromagnetic radiation itself carries quanta of energy packets, later designated the name *photons*. The idea of light being a flux of particles had long been abandoned as it contradicted the well studied and understood Maxwell's electromagnetic theory. The wave-nature of light, which could

be observed in the interference pattern forming when two light sources are combined, was not questionable. Einstein suggested the incorporation of both viewpoints: light is composed of particles behaving in a wave-nature, a phenomenon called *wave-particle duality*.

In 1924, Louis de Broglie proposed, in his doctoral thesis, the applicability of the wave-particle duality also to electrons. He showed how this idea agreed with Bohr's hypothesis, according to which angular momentum was a quantized quantity. Two years later, Erwin Schrödinger put forward a wave-equation for the electron [3] – an equivalence to Maxwell's equations for the photon. At this point, the Schrödinger equation by itself resolved the black-body radiation as well as the photo-electric effect, without the need to rely on the existence of photons. It failed, however, to explain the spontaneous decay of excited atoms to lower energy states accompanied by emitted radiation. This spontaneous emission effect was believed to be "stimulated" by quantum fluctuations of the electromagnetic field in the absence of radiative energy, and the idea of quantized light was not abandoned but rather further investigated.

Many efforts in the field of quantum electrodynamics were carried by Roy J. Glauber, who's work provided a quantum-mechnical understanding of the matter-light interaction and the emission of light from various sources. His study is seen by many as the foundation of the *quantum-optics* field. The theory of quantum-optics promises the possibility of realizing electromagnetic states which behave in a way that cannot be explained by classical electromagnetism, revealing the need for the

quantum theory of light. The realization and observation of these states has become one of the major objectives of experimental quantum-optics.

The simplest non-classical radiation state is the single-photon, i.e., a quantum of energy that cannot be split. An experimental setup to confirm the realization of such a state is illustrated in Figure 1.1: the single-photon is sent through a beam-splitter, and two sensitive detectors are placed at the output arms. Classically, the energy outgoing from the beamsplitter is split between the two arms. According to quantum-mechanics however, the photon can be detected in either arm, but not in both together – thus, the two detectors never indicate coincidentally having detected energy flux. This phenomenon is called the *anti-bunching* effect. The first experimental demonstration of anti-bunching was done in 1977 [4], showing agreement with Einstein's photon hypothesis.

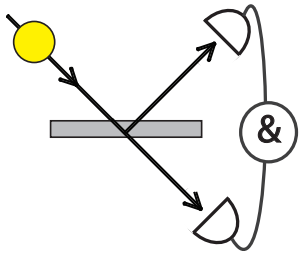


Figure 1.1 The anti-bunching effect: a single-photon is sent through a beamsplitter. Since the photon is a fundamental quantum of energy that cannot be split, it is either transmitted or reflected as a whole. Thus, no coincidence detection occurs at the transmission and reflection arms.

1.2 2-photon interference

Another optical non-classical phenomenon is the *photon bunching* effect taking place when two photons are interfered on a 50% beamsplitter, as illustrated in Figure 1.2. The case in which we find one photon at each of the output ports of the beamsplitter can be obtained either by having both photons transmitted or both reflected. If the two photons are identical in every degree of freedom (except that they impinge on the beamsplitter from different arms), these two options are indistinguishable, hence interfere. In a lossless beamsplitter, the reflected amplitude picks a $\pi/2$ phase respective to the transmitted amplitude [5], thus the amplitude of both photons being reflected acquires a minus sign with respect to the case in which they are transmitted, resulting in destructive interference. Consequently, the two photons cannot leave the beamsplitter at separate arms, rather, they bunch together to yield an outcome state in a superposition of both photons being in either arm together. This effect is referred to as the Hong-Ou-Mandel (HOM) interference [6].

1.3 Linear-optics quantum-computation

The understanding that the smaller systems get the more their behaviour become governed by the rules of quantum-machanics led Richard Feynman to speculate the development of computers employing quantum principles. In 1985, David Deutsch pioneered the field of *quantum computation* [7], proposing logic gates operating on quantum systems. It is believed that a computer harnessing superposition of states

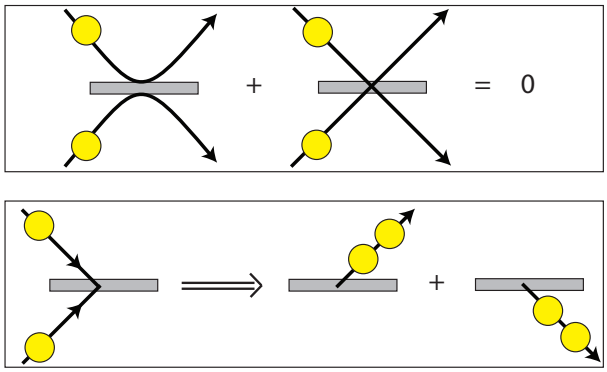


Figure 1.2 When two indistinguishable photons interfere on a 50% beamsplitter, the amplitude of both photons being reflected interferes destructively with the amplitude corresponds to both photons being transmitted (top), thus, the photons bunch together and leave the beamsplitter at the same arm (bottom).

and entanglement can outperform classical computers. The most significant basis for this assumption is the introduction of Shor's algorithm [8], demonstrating how quantum computation can factorize big numbers with reasonable resources; there is no classical equivalence to this algorithm and it is widely believed that such a classical algorithm does not exist at all (though no proof has been put forward).

The implementation of a quantum computer can, in principle, be made with any quantum system. One of the candidates to carry the basic unit of computation, the *qubit*, are photons. As photons barely interact with their environment, they are ideal for information transfer over large distances. On the other hand, interaction is exactly what needed in order to process data: logic gates require interaction between the qubits. It was therefore believed that optical quantum computation necessitated nonlinear interaction between single photons [9], and such interaction is beyond the ability of natural or currently synthesized media to mediate.

In 2001 Knill, Laflamme and Milburn (KLM)[10] astonished the scientific community with their publication proposing a scalable scheme for quantum gates based on linear-optics. The *linear-optics quantum-computation* (LOQC) scheme, which relies on the HOM interference, suggested probabilistic quantum gates acting on the input in the desired manner only with some (typically small) probability. However, ancillary input and output are used to determine and select only those correct outputs. Moreover, they introduced an error correction protocol that allowed one to carry out the computation on an offline input state and then use a teleportation-like procedure, commonly referred to as the *teleportation trick*, to get the requested input state into the post-computed circuit and obtain the corresponding output. Most remarkably, their teleportation protocol works in an almost deterministic way, bringing in the scalability of the scheme.

Since then, the idea of LOQC has developed rapidly. Theoretically, proposals for simplified or higher success probability gates[11–14] were put forward. In addition, another scheme, cluster-state quantum computation[15–18], was introduced. This technique allows offline preparation of the cluster state, while the computation is carried by measurements and local operations. It was shown to be advantageous over the original KLM scheme, but also inspired the application of its ideas to the circuit-based computation[19,20]. Experimentally, optical quantum gates were realized in various configurations[21–31]. Kok *et al.*[32] give a comprehensive review of LOQC.

While apparently simple to implement (linear optics is a well studied and known

field, and a range of various components is widely available) the LOQC schemes require three essential nontrivial resources: quantum memories, photon counting detectors, and single-photon generators.

The quantum memory is vital for the scalability – the correct answers of the gates need to be stored and retrieved at a later time in the computational procedure once the appropriate conditions are met (i.e. the output of other quantum-gates required for the continuation of the computation has arrived successfully). Research in this area resulted in several feasible proposals and demonstrations of state storage and retrieval [33–47].

The original KLM protocol also relies on photon-number resolving detection. Several methods to resolve photon-number have been recently presented [48–52], as well as efforts to reduce the need for detectors that can only distinguish between vacuum and non-vacuum states.

The third essential resource, the single-photon generator, is needed in order to provide photonic qubits. This thesis addresses the provision of a source that produces single photons.

1.4 Single-photon generator

A reliable source for single-photons on demand is vital for the implementation of any LOQC scheme. One might think that the most straightforward way to realize such a source is to attenuate classical light, preferably coherent like a laser beam, to the level of a single photon. However, a single-photon state is highly non-classical: the

photon-number statistics of classical light states is given by the Poissonian distribution, with only $1/e \approx 37\%$ as the maximal probability of finding a single photon [5] (i.e. when the average photon-number in the state is 1). Consequently, classical sources cannot be used in LOQC schemes.

To date, there are two main techniques to generate single-photons: one of them utilizes the photons spontaneously emitted from a single emitting system. The other technique, which is most commonly used nowadays, employs a process in which photons are created randomly but always in pairs; although a successful production of a photon-pair is probabilistic (and typically low), the detection of one photon announces the existence of its sibling, creating what is known as a *heralded* photon. Therefore, despite the inability of the scheme to produce single-photons on demand, it provides the information indicating those events at which a single photon exists. Using a quantum memory to store the heralded photon, this photon can be retrieved whenever necessary, realizing a deterministic photonic qubit source.

1.4.1 Single-emitter photon sources

Ideally, a single-photon source emits one photon, and only one photon, in a pure collimated wave-packet, whenever triggered. The implementation is done by preparing (deterministically) a single quantum system in an excited state. This system then spontaneously decays to the ground state, accompanied with the emission of a photon. Lounis and Orrit [53] review recent developments in the field of single-photon sources. Often, there is more than one decay channel, and the photon may be emit-

ted into one of many different modes, each of which is spread over a large solid angle. However, when put in a cavity, the quantum system and the cavity get coupled, forcing the emission to modes supported by the cavity.

Generation of single-photons has been demonstrated with trapped atoms in a cavity[54–57]. The single atoms are kept in the cavity by means of a dipole trap. This trap, however, can hold the atoms only for a short time, limiting the functionality of the source. Trapping duration of up to 30 seconds, using a two-dimensional optical-lattice, has recently been reported[57]. Ions, on the other hand, can be kept in a cavity for long time with a radio-frequency quadrupole trap. Indeed, single-photon sources with ions[58,59] have been demonstrated with operational duration of hours. While both the atomic and ionic schemes to generate single photons exhibit good efficiency, they suffer from highly complicated setup involving several laser beams and actively stabilized cavities.

It is possible to extend the above idea to molecules; the advantage of molecules is that they can be trapped on a substrate or as a defect in a solid, eluding the need for complicated dipole traps. However, molecules have many vibrational levels in addition to the electronic transitions. As a consequence, the electronic excitation of the molecule is accompanied by the creation of phonons, and the decay results in a range of emission wavelengths. Therefore, the wavelength of the emitted photon is not deterministic and varies from one emission to another. This problem could be overcome by putting the molecule in a cavity, but this is very difficult and has not been done so far. Low temperatures eliminate some of the emission prob-

lems with molecules, and single-photon emission from organic molecules has been demonstrated in cryogenic conditions [60,61]. Efforts have also been made at room temperature [62–65].

Another interesting option is the use of a colour centre – a defect in a crystal – as an emitter. The defect perturbs the energy levels around it, and a few colour centres possess photophysical properties adequate for single-photon emission. Demonstration of single-photon emission has been done with nitrogen-vacancy [66,67] and nickel-nitrogen [68] centres in diamonds. While these colour centres are very stable, they possess dark metastable states which limit the production yield.

Recent developments in the semiconductor industry have given rise to the ability to use semiconductor nanocrystals [69–71]. One of their greatest advantages is the possibility to grow a cavity along with the emitting structure – simplifying the manufacturing process as well as the experimental setup. However, their luminescent spectrum fluctuates, even at low temperatures.

Finally, we mention quantum dots [72–77]. Quantum dots have stable photophysical properties, and emit photons that are nearly Fourier-limited. Again, cryogenic conditions are required, which complicates the setup. The most severe problem of quantum dots as sources for single photons is the distinguishability between dots – every quantum dot has its own emission spectra. Thus, although efforts to resolve this problem are being carried out [77], these sources at present cannot be used for LOQC protocols.

1.4.2 Heralded photons

While a true single-photon source on demand is most likely to be realized with one of the above single emitters, to date, they all suffer from one or several of the following drawbacks: setup complexity, difficulty to duplicate the setup to implement identical sources, or low collection efficiency. Due to those drawbacks, most of the experiments with single-photons have harnessed a different type of source: heralded photons from *spontaneous parametric down conversion* (SPDC) [78].

Before explaining the process, let us consider the ensemble configuration: instead of deterministically exciting a single system, we can use an ensemble of emitters, each prepared in its excited level to a very low probability, but the overall preparation is high enough to observe the spontaneous emission. Nonetheless, in such a scheme, the probability for two sites to emit a photon, i.e. end up with two photons, is not low enough (Poissonian distribution), and does not beat classical sources. Such an ensemble, therefore, cannot be useful as a single-photon source.

The heralded-photon approach is to generate pairs of photons in the ensemble, employing the process in which the decay to the ground state is accompanied by the emission of two photons rather than a single one. Detecting one of the photons heralds the occurrence of such a process. The probability of generating more than one pair can be made arbitrarily low by low power interaction, at the expense of low generation rate of a single-pair. Such interaction takes place in optically nonlinear media. In the photonic picture, SPDC is described by a process in which one photon from an external electromagnetic field, the pump, is annihilated by the medium,

which then emits photon-pairs, called *daughters*. This process is mediated by the $\chi^{(2)}$ nonlinear susceptibility, conserves energy and therefore the frequencies of the daughter photons sum up to the pump frequency.

In recent years, this technique has been extended to *spontaneous four-wave mixing* (SFWM), where the nonlinear $\chi^{(3)}$ susceptibility of the medium mediates the conversion of *two* photons from the pump into two different photons, called *sidebands*. Energy conservation, again, requires that the frequency sum of the sidebands matches the frequency sum of the two pump photons. Both SPCD and SFWM processes, illustrated in Figure 1.3, usually generate photons distinguishable from each other (in spatial, polarization or frequency degrees of freedom) such that they can be separated. Traditionally, they are designated as *signal* and *idler*. Thus, one photon (e.g. the signal) can be detected without affecting the other – producing a single heralded photon (the idler).

Unlike the case of single emitters, here (in SPDC and SFWM) resonant interaction cannot be efficiently employed, because matter is highly absorptive at resonant wavelengths, resulting in losses in the external field as well as the generated photonic pair. We are therefore constraint to work with fields that are far from the material resonances, which implies low nonlinear interaction. Despite the above, SPDC and SFWM are the brightest single-photon sources to date, thanks to the enormous interaction ensemble.

The capability of SFWM to generate heralded single photons was first demonstrated experimentally in 2002 by Fiorentino *et al.*[79] in dispersion shifter fibres

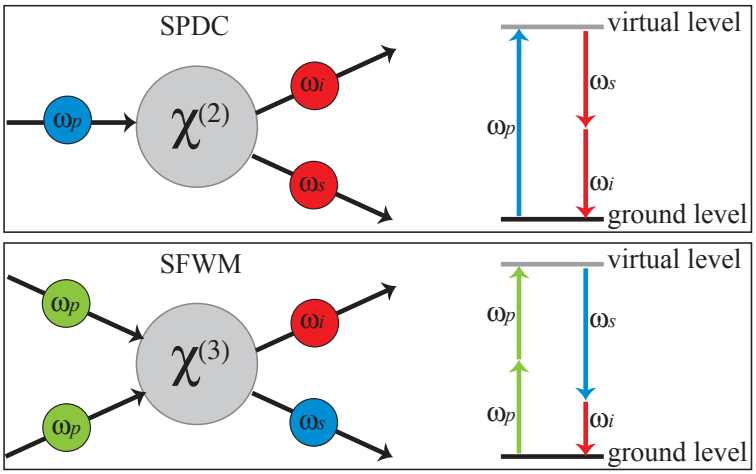


Figure 1.3 Top: the spontaneous parametric downconversion. One pump photon, with frequency ω_p, interacts with the $\chi^{(2)}$ nonlinearity of the medium, and two daughter photons are created, designated as the signal (ω_s) and idler (ω_i). Bottom: the spontaneous four-wave mixing interaction. Two photons from the pump interact with the $\chi^{(3)}$ nonlinearity to create two sideband photons.

(DSFs), with signal and idler at telecom wavelengths. In 2004 Sharping *et al.*[80] demonstrated the generation of photon-pairs at visible wavelengths in a photonic crystal fibre (PCF). With improved techniques to implement SFWM both in DFS[81] and PCFs[82], it became clear that fibre sources for photon-pairs are highly efficient. Efforts by Chen *et al.*[83] showed large sensitivity of the sideband wavelengths to small pump frequency tuning. Specifically, they showed that the photon-pair could be generated hundreds of nanometers away from the pump. This feature was employed by Rarity *et al.* to generate photon-pairs with reduced Raman contamination[84], and to implement the technique for generation in the visible bandwidth[85] with high efficiency detectors. Further theoretical and experimental investigation of these results are published by Alibart *et al.*[86]. The high efficiency and util-

ity of fibre-based photon-pair sources allowed the implementation of experiments demonstrating the creation of polarization entangled photons [87–89], non-classical two-photon interference [89,90] and creation of hyperentanglement [91].

Past experiments concentrated on the individual properties of the generated photons, with efforts to meet requirements of specific applications – e.g. generating the photons at the telecom band to reduce loss in optical networks, creating photon-pairs at the visible wavelengths where efficient detectors exist, or creating the sidebands far detuned from the pump to reduce Raman background. While these demonstrations show the high potential of the fibre-based sources, little efforts were put on engineering the joint properties of the photons. As we explain in the following, the correlations within a photon-pair plays a significant role in many applications.

The general form of a photon-pair state is given by

$$|\psi\rangle = \iint d\omega_s \, d\omega_i \, f(\omega_s, \omega_i) |\omega_s\rangle |\omega_i\rangle, \tag{1.1}$$

where $|\omega_s\rangle|\omega_i\rangle$ is a photon-pair state in which the signal is at angular frequency ω_s and the idler at ω_i. $f(\omega_s, \omega_i)$ is the *joint spectral amplitude*. For simplicity, we consider only the spectral degree of freedom. The amplitude dictates the nature of the correlations between the photons. For the purpose of implementing a heralded pure single-photon source, it is crucial for the photons to be uncorrelated, as explained in the following: according to the Schmidt-decomposition procedure, the state in Eq.

(1.1) can be written in the form:

$$|\psi\rangle = \sum_n \sqrt{\lambda_n}|s_n\rangle|i_n\rangle \ , \tag{1.2}$$

where the Schmidt coefficients $\{\lambda_n\}$ are non-negative numbers obeying the normalization condition $\sum_n \lambda_n = 1$, $\{|s_n\rangle\}$ and $\{|i_n\rangle\}$ are orthonormal states sets of the signal and idler photons, respectively. In this representation, the density matrix of the state is given by

$$\rho \ = \ \sum_{n\,m} \sqrt{\lambda_n \lambda_m}|s_n\rangle\langle s_m| \otimes |i_n\rangle\langle i_m| \ . \tag{1.3}$$

As we use the signal photon solely for heralding purposes, we are actually interested in the idler-photon subsystem state (or *vice-versa*). In order to resolve the state of a subsystem, we need to trace over the degrees of freedom of the rest of the system. Here, we trace over the signal-photon's degrees of freedom, leaving the idler-photon in the density matrix:

$$\pi_i = Tr_s[\rho] = \sum_n \lambda_n |i_n\rangle\langle i_n| \ . \tag{1.4}$$

Conversely, the density matrix of the signal photon is:

$$\pi_s = Tr_i[\rho] = \sum_n \lambda_n |s_n\rangle\langle s_n| \ . \tag{1.5}$$

Generally, the density matrices π_s and π_i represent mixed states. These states are pure if and only if the signal and idler photons are not correlated, mathematically

expressed as

$$f(\omega_s, \omega_i) = g_s(\omega_s) g_i(\omega_i) \ , \tag{1.6}$$

i.e., the amplitude is factorable. In this case, the Schmidt decomposition results in

$$\begin{gathered} \lambda_1 = 1 \quad , \quad \lambda_{n\neq 1} = 0 \\ |s_1\rangle = \int d\omega_s \, g_s(\omega_s) |\omega_s\rangle \quad , \quad |i_1\rangle = \int d\omega_i \, g_i(\omega_i) |\omega_i\rangle \end{gathered} \tag{1.7}$$

with the signal and idler pure wavefunctions $|s_1\rangle$ and $|i_1\rangle$, respectively. In general, one quantifies the purity of the signal (or idler) photons as

$$p = Tr[\pi_s^2] = Tr[\pi_i^2] = \sum_n \lambda_n^2 \ . \tag{1.8}$$

For pure photons $p = 1$, while $p \to 0$ as the photon's state becomes more mixed. For a given joint amplitude $f(\omega_s, \omega_i)$, the density matrices are given by:

$$\begin{aligned} \pi_s &= \int d\omega_s d\omega_s' d\omega_i f(\omega_s, \omega_i) f^*(\omega_s', \omega_i) |\omega_s\rangle\langle\omega_s'| \ , \\ \pi_i &= \int d\omega_s d\omega_i d\omega_i' f(\omega_s, \omega_i) f^*(\omega_s, \omega_i') |\omega_i\rangle\langle\omega_i'| \ , \end{aligned} \tag{1.9}$$

and the purity is evaluated as:

$$p = \int f(\omega_1, \omega_2) f^*(\omega_3, \omega_2) f(\omega_3, \omega_4) f^*(\omega_1, \omega_4) d\omega_1 d\omega_2 d\omega_3 d\omega_4 \ . \tag{1.10}$$

Unfortunately, the photon-pairs produced in the SPDC and SFWM are typically highly correlated due to energy and momentum conservation contraints, and the

resultant heralded photon, being in a mixed state, is not useful for the application of the LOQC schemes. The common way to eliminate the correlations is to use spectral and spatial filters, i.e., post-select only pairs with low correlations. This, however, leads to a degradation in the detection rate and, possibly, in the heralding efficiency as well (depending whether the heralded photon is filtered or not). U'Ren *et al.*[92] have shown theoretically that the spectral correlations between the photons can be avoided by choosing appropriate group-velocity matching conditions in SPDC. This scheme has recently been implemented experimentally in a bulk KDP crystal[93,94], demonstrating a remarkably efficient heralding (up to 44%) of highly pure photons (about 95%). However, a degree of spatial correlation still exists, requiring spatial filtering to eliminate it. Generating photon-pairs in a waveguide that supports only one spatial mode, such as single-mode fibres or planar waveguides, circumvents the spatial type of correlations within the creation process. Therefore, the production of spectrally uncorrelated photon-pairs in such waveguides is appealing.

The loss in fused-silica waveguides is typically very low. Consequently, the most commonly used waveguides are those made of silica, which mediates the nonlinear interaction in fibres. The dominant nonlinearity in amorphous materials like glass is the four-wave mixing interaction, which is typically weaker than the three-wave mixing in crystals, as it depends on higher order of the input amplitude: while the generation probability in SPDC depends linearly on pump power, in SFWM this probability depends on the square of pump power. Nonetheless, as fibres confine the coupled light into a small area (several microns in diameter), the intensity of the

light during its propagation in the fibre is kept high along the whole length. This is especially true in *photonic-crystal fibres* (PCFs), where the mode field diameter can be less than 2 μm. Therefore, the generation rate of photon-pairs in fibres is higher than SPDC in bulk crystals [82,86], and eliminates spatial correlations. In addition, it is possible with current technology to fabricate PCFs with a wide variety of dispersion characteristics, allowing a huge freedom in choosing the phase-matching conditions. It is this very freedom that allows the realization of photon-pair sates with tailored spectral properties. Specifically, uncorrelated photon-pairs can be generated in birefringent fibres.

This thesis is about the realization of generated uncorrelated photon-pairs in birefringent optical fibres. The theoretical and experimental study is presented in the following chapters.

1.5 Thesis outline

The thesis is presented in 8 chapters. Chapter 2 reviews briefly the spontaneous four-wave mixing scattering in optical fibres and the resultant photon-pair joint spectral amplitude, which serves as the theoretical background for this thesis. It also discusses the experimental constraints, including the Raman scattering in fibres. In Chapter 3 we present our theoretical study for the generation of uncorrelated photon-pairs in photonic-crystal fibres. Chapter 4-6 are devoted to the experimental investigation of the theoretical findings, demonstrating highly pure heralded photons: in Chapter 4 we experimentally identify a suitable fibre to conduct our work

with, Chapter 5 demonstrates the purity of the generated heralded photons, and in Chapter 6 the significance and influence of various parameters is studied. In Chapter 7 we propose to extend our technique to standard optical fibres, and provide theoretical and experimental evidences to the reality of this possibility. Chapter 8 summarizes, gives an outlook to future work and concludes the thesis.

Chapter 2

SFWM in fibres

In this chapter we present the theoretical background for this thesis, concentrating on the SFWM interaction in fibres. We start with a short introduction to nonlinear optics followed by the quantum electrodynamics formalism. We then explain the SFWM interaction and the way it occurs in a guiding configuration. Derivation of the general form of the produced photon-pair state through SFWM in fibres is followed. A simple fibre model is reviewed to demonstrate the conditions in which SFWM takes place. The chapter ends by pointing out experimental challenges that need to be considered when implementing this process as a photon-pair source.

2.1 Nonlinear optics

When an electromagnetic wave propagates through a medium, it interacts with the charges of that medium. To the lowest order, this interaction is reduced to the dipole interaction, where we assume that at each point $\vec{r}$ inside the matter there is a time

(t) dependent dipole $\vec{P}(\vec{r},t)$. The effect of the dipole on the radiation is given by the wave equation derived from Maxwell's equations:

$$\frac{\partial^2}{\partial t^2}\vec{E}(\vec{r},t) - c^2\nabla^2\vec{E}(\vec{r},t) = -\frac{1}{\epsilon_0}\frac{\partial^2}{\partial t^2}\vec{P}(\vec{r},t)\ , \tag{2.1}$$

where $\vec{E}(\vec{r},y)$ is the electric field and ϵ_0 is the permittivity of the vacuum.

The dipole polarization arises due to its response to the applied electromagnetic field. In essence, the response can be complicated, but for transparent (at the relevant wavelengths) materials, it's normally very weak, and can be expanded in power series:

$$\frac{1}{\epsilon_0}P_i(\vec{r},t) = \chi^{(1)}_{ij}E_j(\vec{r},t) + \chi^{(2)}_{ijk}E_jE_k(\vec{r},t) + \chi^{(3)}_{ijkl}E_j(\vec{r},t)E_k(\vec{r},t)E_l(\vec{r},t) + ...\ , \tag{2.2}$$

where the subscript indices tag the Cartesian component of the polarization or the field, and Einstein summation convention is implied for repeating indices. $\chi^{(n)}$, which is assumed here to be uniform within the medium, is the n order susceptibility tensor. Substituting Eq. (2.2) in (2.1) yields an equation, generally nonlinear, for the electric field propagation. The linear susceptibility $\chi^{(1)}$ is responsible for the dispersion, the higher order terms provide the nonlinear contribution. Note that in Eq. (2.2) we regarded the interaction as instantaneous, i.e., the polarization responded instantaneously to the applied field and no history is accumulated. This assumption is not strictly correct, and we will not apply it to the *linear* susceptibility, because such instantaneous linear response implies no dispersion, while phenomenologically

we know that media index of refraction is wavelength dependent. However, for our calculations, as long as the nonlinear susceptibility does not vary appreciably within the bandwidth of the involved fields, the flat spectral response is applicable for frequencies far detuned from the material resonances.

Symmetries in the medium force constraints on the components of the susceptibilities [95]. For example, looking at $\chi^{(2)}$, if we invert the electric field, i.e. $E_j \to -E_j$ and $E_k \to -E_k$, the response of the polarization stays intact, meaning that it has a preferable direction to respond. This can only happen in materials which are asymmetric under inversion. While some crystals, called *non-centrosymmetric crystals*, may bear such asymmetry, amorphous materials like glass do not, and the 2nd. order nonlinearity vanish for them. Thus, the three-wave mixing, mediated by $\chi^{(2)}$, is usually the dominant interaction in non-centrosymmetric crystals, and in glass the leading nonlinear term is the four-wave mixing ($\chi^{(3)}$).

2.2 The quantum-mechanical formalism

The quantization of the electromagnetic field is part of the general quantum-field theory. In this theory, the ground state is the vacuum, represented as $|0\rangle$ to emphasize that no particles (quanta of energy) exist. All of the manipulations to the electromagnetic field are applied through the annihilation operator $a_{\vec{e}}(\vec{k})$ and its Hermitian-conjugate, the creation operator $a^{\dagger}_{\vec{e}}(\vec{k})$. The latter creates a quantum excitation – photon – in a monochromatic plane-wave form with wave-vector $\vec{k}$ and polarization along the unit vector $\vec{e}$. The photon's polarization is always orthogonal

to the propagation direction, given by the wave-vector, hence $\vec{e} \cdot \vec{k} = 0$. The annihilation operator removes such a photon from the state. This set of operators obey the commutation relations:

$$\begin{aligned} \left[a_{\vec{e1}}(\vec{k}_1)\,,\, a_{\vec{e2}}(\vec{k}_2)\right] &= 0\,, \\ \left[a^{\dagger}_{\vec{e1}}(\vec{k}_1)\,,\, a^{\dagger}_{\vec{e2}}(\vec{k}_2)\right] &= 0\,, \\ \left[a_{\vec{e1}}(\vec{k}_1)\,,\, a^{\dagger}_{\vec{e2}}(\vec{k}_2)\right] &= \delta(\vec{k}_1 - \vec{k}_2)\vec{e1} \cdot \vec{e2}\,. \end{aligned} \tag{2.3}$$

The eigenvalues of the *number density operator*, $n_{\vec{e}}(\vec{k}) = a^{\dagger}_{\vec{e}}(\vec{k})a_{\vec{e}}(\vec{k})$, are the number of photons in the mode represented by the wave-vector $\vec{k}$ and polarization $\vec{e}$. The energy, or Hamiltonian, of the electromagnetic field is

$$H_{\mathrm{EM}} = \iiint d^3k \sum_{\vec{e}} \hbar\omega_{\vec{k}} a^{\dagger}_{\vec{e}}(\vec{k})a_{\vec{e}}(\vec{k})\,, \tag{2.4}$$

where the angular frequency is given by $\omega_{\vec{k}} = c|\vec{k}|$, c is the speed of light in free space, and the summation is over two orthogonal polarizations. Thus, the energy of a single photon is given by its frequency times Planck constant, while the total energy is a summation over the quanta of energy in the field. If we consider the propagation inside a medium, we can generalize to include the linear interaction between the electromagnetic field and the matter, thus, $\omega_{\vec{k}}$ is given by the dispersion in the medium, and may depend also on the polarization of the field. When light travels from one (stationary) medium to another, its frequency does not change, but the wave-vector does. It is therefore sometimes more convenient to use the

angular frequency as the characteristic of a photon. In this notation, which we use throughout this thesis, the commutation relations are given by:

$$\begin{aligned} [a_\mu(\omega_1)\,,\, a_\nu(\omega_2)] &= 0\,, \\ \left[a^\dagger_\mu(\omega_1)\,,\, a^\dagger_\nu(\omega_2)\right] &= 0\,, \\ \left[a_\mu(\omega_1)\,,\, a^\dagger_\nu(\omega_2)\right] &= \delta(\omega_1-\omega_2)\delta_{\mu,\nu}\,, \end{aligned} \tag{2.5}$$

where the subscripts μ and ν are mode-indices tagging different modes within the corresponding frequency, e.g., in free space or dielectric media, they will be associated with direction of propagation and polarization, while in a waveguide they denote different propagating modes for the specific frequency. The Hamiltonian of the free electromagnetic field is then rewritten as

$$H_{\text{EM}} = \int d\omega \sum_\mu \hbar\omega a^\dagger_\mu(\omega) a_\mu(\omega)\,. \tag{2.6}$$

The above creation and annihilation operators are related to waves spread over the infinite space. In practice, physical processes create radiation in volume-limited wave-packets. Such a field can be represented as a superposition of the monochromatic waves, and the general form of the annihilation operator of a mode designated by, say, s, is then given by:

$$A_s = \int d\omega \sum_\mu f_{s,\mu}(\omega) a_\mu(\omega)\,, \tag{2.7}$$

where the amplitude $f_{s,\mu}(\omega)$ satisfies the normalization $\sum_\mu \int d\omega f_{s,\mu}(\omega) f^*_{s,\mu}(\omega) = 1$.

A single-photon in the pure mode s is, then

$$|1_s\rangle = A_s^\dagger|0\rangle = \int d\omega \sum_\mu f_{s,\mu}^*(\omega) a_\mu^\dagger(\omega)|0\rangle \ . \tag{2.8}$$

A state with n photons at the s mode, called *Fock state*, is given by

$$|n_s\rangle = \frac{1}{\sqrt{n!}} A_s^{\dagger n}|0\rangle \ . \tag{2.9}$$

Using the field operators, the photon-pair state in Eq. (1.1) is written as

$$|\psi\rangle = \iint d\omega_s \, d\omega_i \, f(\omega_s, \omega_i) a^\dagger(\omega_s) a^\dagger(\omega_i)|0\rangle \ , \tag{2.10}$$

where the mode-index is implicit in accordance with Eq. (1.1).

Finally, Glauber showed [96] how this quantum formalism coincides with the well-studied classical electromagnetism, by introducing the *coherent-state*, commonly referred to as *classical state* or *Glauber state*: he described a classical electromagnetic wave, in a mode s (Eq. (2.7)) as

$$|\alpha\rangle = e^{\alpha A_s^\dagger}|0\rangle = e^{-\frac{|\alpha|}{2}} \sum_{n=0}^{\infty} \frac{\alpha^n}{\sqrt{n!}}|n_s\rangle \ , \tag{2.11}$$

where α represents the complex amplitude of the (classical) field, with $|\alpha|^2$ being the mean (expectation value of the) photon-number in the mode, i.e. $< n_s >= \langle\alpha|A_s^\dagger A_s|\alpha\rangle = |\alpha|^2$. A significant feature of the coherent state is being an eigenstate of the annihilation operator with eigenvalue α. In addition, for strong enough field,

it is also nearly an eigenstate of the creation operator: the normalized state resulting from the action with the creation operator on the coherent state is given by

$$|\xi\rangle = \frac{A_s^\dagger|\alpha\rangle}{\sqrt{\langle\alpha|A_s A_s^\dagger|\alpha\rangle}} \,. \tag{2.12}$$

The overlap of this state with the original coherent state is

$$|\langle\alpha|\xi\rangle|^2 = \frac{|\alpha|^2}{|\alpha|^2+1} = 1 - O\left(\frac{1}{|\alpha|^2}\right) \,. \tag{2.13}$$

Hence, for a light beam with large average photon-number ($|\alpha|^2 \gg 1$) the creation operator keeps the coherent state intact. The associated eigenvalue is $\langle\alpha|A_s^\dagger|\alpha\rangle = \alpha^*$. In summary, the classical state has the properties:

$$A_s|\alpha\rangle = \alpha|\alpha\rangle \qquad , \tag{2.14a}$$

$$A_s^\dagger|\alpha\rangle \cong \alpha^*|\alpha\rangle \qquad \text{(for } |\alpha|^2 \gg 1\text{)}. \tag{2.14b}$$

Since all of the field observables can be expressed in terms of the creation and annihilation operators, the coherent state is (nearly) an eigenstate of the observables, with eigenvalues corresponding to the classical values. For example, The Hamiltonian of quantum-electrodynamics contains terms with the electric and magnetic field operators. Thus, when it acts on a coherent state, one can replace the operators with the classical values, and the evolution, given by Schrödinger equation, gives rise to the classical evolution with Maxwell equations. Thus, the coherent state bridges

the gap between quantum and classical mechanics.

2.3 The SFWM interaction

As SFWM involves interaction of low photon-number, it cannot be explained by strictly classical means, and a quantum description is required. Let us first go back to the nonlinear interaction: substituting Eq. (2.2) in Eq. (2.1), retaining only the linear and $\chi^{(3)}$ terms, we obtain:

$$\frac{\partial^2}{\partial t^2}\left(\epsilon_{ij}E_j + \chi^{(3)}_{ijkl}E_jE_kE_l\right) - c^2\nabla^2 E_i = 0\ . \tag{2.15}$$

where $\epsilon_{ij} = \epsilon_0(I+\chi^{(1)}_{ij})$ is the permittivity tensor in the medium and I is the identity tensor. Thus, the four-wave mixing, mediated by $\chi^{(3)}$, couples four fields.

This classical treatment is usually used to construct a phenomenological quantum Hamiltonian[5]. Since we're only interested in the electromagnetic field's degrees of freedom, and disregard the state of the medium, our effective Hamiltonian is of the form:

$$H = H_{\text{EM}} + H_{\text{NL}}\ , \tag{2.16}$$

where H_{EM}, given by Eq. (2.6), accounts for up to the linear interaction, and H_{NL} is the nonlinear term. In FWM, it is given by

$$H_{\text{NL}} = \epsilon_0\chi^{(3)}_{ijkl}\iiint d^3r\, E_i(\vec{r})E_j(\vec{r})E_k(\vec{r})E_l(\vec{r})\ . \tag{2.17}$$

Normally, we prefer to see the field $\vec{E}(\vec{r})$ as a superposition of several modes, and we're interested in the energy exchange between these defined modes. For example, the field may be constructed of four bands centred at four different wavelengths, and we want to follow the evolution of each individual bandwidth in the presence of FWM interaction. As another example, we may wish to look at the interaction between orthogonal polarizations. Indeed, in this thesis, we are interested in the coupling between an external pump and generated signal and idler at frequencies far detuned from the pump. They may also differ in polarization. We thus tag the modes as p for pump, s for signal and i for idler.

In the Schrödinger representation, the state $|\psi(t_0)\rangle$ at time t_0 evolves to time $(t_0 + t)$ as

$$|\psi(t_0 + t)\rangle = U(t_0 + t, t_0)|\psi(t_0)\rangle \ , \tag{2.18}$$

where $U(t_0+t, t_0)$ is the *evolution operator* given by the solution to the Schrödinger equation

$$i\hbar\frac{d}{dt}U(t_0 + t, t_0) = H(t)U(t_0 + t, t_0) \ , \tag{2.19}$$

with the initial condition $U(t_0, t_0) = \mathbb{1}$ (identity operator). Generally, solving this equation is difficult, due to the nonlinearity. However, the nonlinear interaction Hamiltonian normally contributes little to the overall energy. We can therefore employ perturbation theory to find the influence of the interaction on the initial state. This is usually easier to do in the interaction picture, in which the state

$|\psi(t_0+t)\rangle$ is represented as

$$|\psi(t_0+t)\rangle_0 = U_0^\dagger(t_0+t,t_0)|\psi(t_0+t)\rangle \ , \tag{2.20}$$

with

$$U_0(t_0+t,t_0) = e^{\frac{-i}{\hbar}H_{EM}t} \tag{2.21}$$

is the "free" evolution operator, i.e., the evolution if there were no interaction. t_0 is assumed to be the time at which the interaction is switched on. We then define the *scattering operator* as

$$\mathbb{S}(t_0+t,t_0) = U_0^\dagger(t_0+t,t_0)U(t_0+t,t_0) \ , \tag{2.22}$$

and the time-dependent *interaction Hamiltonian*

$$H_{int}(t_0+t) = U_0^\dagger(t_0+t,t_0)H_{NL}U_0(t_0+t,t_0) \ . \tag{2.23}$$

It follows, from the above definitions with the Schrödinger equation, that the scattering operator is given by:

$$\mathbb{S}(t_0+t,t_0) = \mathcal{T}\exp\left[\frac{1}{i\hbar}\int_{t_0}^{t_0+t} d\tau\, H_{int}(\tau)\right] \ , \tag{2.24}$$

where $\mathcal{T}$ indicates that time-ordering is applied.

Every operator A in the Schrödinger picture is transformed to the interaction

representation with time dependency as

$$A_0(t_0+t) = U_0^\dagger(t_0+t,t_0)AU_0(t_0+t,t_0)\ . \tag{2.25}$$

For the rest of this thesis, we work in the interaction picture, assume all states are given in this representation and we drop the explicit notation. The transformation to Schrödinger picture is carried by applying an evolution in free space, which doesn't affect the state's properties we're looking at in this thesis.

Using Eq. (2.17), the FWM interaction Hamiltonian in a fibre with length L is given by[86]

$$H_{int}(t) = \epsilon_0\chi^{(3)}\iint dx\,dy\int_0^L dz\,E_p^2(x,y,z,t)E_s(x,y,z,t)E_i(x,y,z,t)\ , \tag{2.26}$$

where $\chi^{(3)}$ is the relevant susceptibility for the associated type of interaction, x, y and z are spatial coordinates, z is along the propagation direction in the fibre. The electric-field operators are

$$E_\mu(x,y,z,t) = \int d\omega\sqrt{\frac{\hbar\omega}{2\epsilon(\omega)V}}a_\mu(\omega)e^{i(k_\mu(\omega)z-\omega t)} + \text{h.c.}\ , \tag{2.27}$$

where $\mu = p,s,i$, $k_\mu(\omega)$ is the effective wave-vector of the μ mode in the fibre, $\epsilon(\omega)$ is the permittivity in the interaction medium, V is the quantization volume and the integration is over the bandwidth associated with the μ mode.

Note that in essence, the nonlinear Hamiltonian contains terms of the form E_μ^4

and $E_\mu^2 E_\nu^2$ (with $\nu \neq \mu$). The first term, describing a nonlinear interaction of a mode with itself, affects the phase of the field. Hence it is called *self phase modulation* (SPM). The SPM can be seen as a process in which two photons from the same mode are annihilated and created by the medium. The second mentioned nonlinear term gives rise to *cross phase modulation* (XPM), in which a mode's phase is affected by the interaction with another field. In the photonic picture, the XPM describes the annihilation of two photons from two different modes and the creation of two photons into these modes. Both SPM and XPM do not exchange energy between modes. For the time being, we assume that their effect is negligible, but will consider them later.

In this chapter we study how the signal and idler modes, initially in the vacuum state, evolve when a pump propagates in fibres.

2.4 The photon-pair state generated in fibres

According to classical electromagnetism, FWM can generate a radiation field in a new mode by extracting energy from three other electromagnetic modes (some or all of them may be degenerate). This is done by the nonlinear response, which lets the dipoles in the medium oscillate at frequencies different from the ones of the applied fields. For example, suppose the applied field oscillates at an angular frequency ω, $E(t) = E_0 \cos(\omega t)$. The third order nonlinear response causes polarization

oscillations as

$$P(t) = \chi^{(3)} E_0^3 \cos^3(\omega t) = \frac{\chi^{(3)}}{4} E_0^3 \left(3\cos(\omega t) + \cos(3\omega t)\right) , \tag{2.28}$$

i.e., the polarization evolution has a component oscillating at angular frequency 3ω. This oscillation causes the emission of electromagnetic radiation at that frequency – three times larger than the applied one, a process called *third harmonic generation*.

The classical FWM description does not support the conversion of two modes into new empty ones, because two fields cannot create the (third order) nonlinear oscillations of the dipoles, i.e., the term $E_p^2 E_s$ vanishes (because $E_s = 0$) and so $E_p^2 E_i$, leading to no dipole oscillations at either the idler or signal modes, respectively. Quantum mechanics, however, does allow the process to occur spontaneously. The mechanism driving such an emission to empty modes is similar to the spontaneous decay of atoms to the ground state. In a semi-classical description, the (empty) signal and idler modes are considered to be seeded by quantum vacuum fluctuations.

Assuming a classical undepleted pump, one can substitute the field operator $E_p(x, y, z, t)$ in Eq. (2.26) with the classical field. Using Eq. (2.27), carrying out the integral over the spatial coordinates, and retaining only the terms which create

(and annihilate) sideband photons, one obtains:

$$\begin{aligned} H_{int}(t) &= \frac{\epsilon_0 \chi^{(3)} \hbar}{2V} \int d\omega_{p1} \int d\omega_{p2} \int d\omega_s \int d\omega_i \left\{ \mathcal{I}_{(\omega_{p1},\omega_{p2},\omega_s,\omega_i)} \times \right. \\ & \sqrt{\frac{\omega_s \omega_i}{\epsilon(\omega_s)\epsilon(\omega_i)}} \mathcal{E}_p(\omega_{p1}) \mathcal{E}_p(\omega_{p2}) e^{-i(\omega_{p1}+\omega_{p2}-\omega_s-\omega_i)t} e^{-i\frac{L\Delta k}{2}} \times \\ & \left. L\mathrm{sinc}\left(\tfrac{L\Delta k}{2}\right) a_s^\dagger(\omega_s)\, a_i^\dagger(\omega_i) \right\} + h.c. \,, \end{aligned} \tag{2.29}$$

here, and for the rest of this thesis, μ is associated with a mode supported by the fibre, $\mathcal{I}_{(\omega_{p1},\omega_{p2},\omega_s,\omega_i)} = \iint dx\, dy\, e_p(x,y,\omega_{p1}) e_p(x,y,\omega_{p2}) e_s^*(x,y,\omega_s) e_i^*(x,y,\omega_i)$ is the spatial overlap of the interacting fields, $e_\mu(x,y,\omega)$ is the transverse amplitude of the μ mode normalized as $\iint dx\, dy\, |e_\mu(x,y,\omega)|^2 = 1$, $\mathcal{E}_p(\omega)$ is the spectral amplitude of the pump, and the vector-mismatch is given by

$$\Delta k(\omega_{p1},\omega_{p2},\omega_s,\omega_i) = k_p(\omega_{p1}) + k_p(\omega_{p2}) - k_s(\omega_s) - k_i(\omega_i) \,. \tag{2.30}$$

Thus, the sinc function in the Hamiltonian constitutes the momentum-conservation.

Starting with the vacuum $|\psi(t_0)\rangle = |0\rangle$ in the signal and idler modes (external pump field in the pump mode), the evolution of the state is given by:

$$|\psi(t_0+t)\rangle = \mathbb{S}(t_0+t,t_0)|0\rangle \,. \tag{2.31}$$

We consider low pump power, such that the evolution can be expanded in a pertur-

bative way. Thus, to the first order, the evolving state can be written as:

$$|\psi(t_0+t)\rangle = |0\rangle + \frac{1}{i\hbar}\int_{t_0}^{t_0+t} d\tau\, H_{int}(\tau)|0\rangle\ . \tag{2.32}$$

Substituting Eq. (2.29) in (2.32) and carrying the integral over time, we obtain:

$$\begin{aligned} |\psi(t)\rangle \quad = \quad & |0\rangle + \\ & \int d\omega_{p1}\int d\omega_{p2}\int d\omega_s \int d\omega_i \left\{ \kappa \mathcal{E}_p(\omega_1)\mathcal{E}_p(\omega_2)\times \right. \\ & \left. e^{-i\frac{\Delta\omega t}{2}}\, t\,\mathrm{sinc}\left(\tfrac{\Delta\omega t}{2}\right) e^{-i\frac{L\Delta k}{2}}\, L\mathrm{sinc}\left(\tfrac{L\Delta k}{2}\right) a_s^\dagger(\omega_s)\, a_i^\dagger(\omega_i) \right\}|0\rangle\ , \end{aligned} \tag{2.33}$$

where

$$\kappa = \frac{\epsilon_0 \chi^{(3)}}{2iV}\mathcal{I}(\omega_p,\omega_p,\omega_s,\omega_i)\sqrt{\frac{\omega_s\omega_i}{\epsilon(\omega_s)\epsilon(\omega_i)}}\ , \tag{2.34}$$

and $\Delta\omega = \omega_{p1} + \omega_{p2} - \omega_s - \omega_i$ is the angular frequency mismatch expressing the energy difference between the incoming photons and outgoing ones (up to the reduced Planck constant $\hbar$). The application of the external pump field switches on the interaction. The interaction Hamiltonian is non-zero only during the propagation of the pump in the fibre; it vanishes before the pump pulse reaches the fibre as well as after it emerges out of the fibre. Thus, taking $t_0 \to -\infty$ and $t \to +\infty$ (long scattering duration) contributes to the evolution only during the pump's propagation in the finite length of the fibre, hence does not affect the description of the physical process we're examining. This simplifies Eq.(2.33), so that only terms with $\Delta\omega = 0$ contribute to the final photonic state with conserved energy between the

electromagnetic fields. Let's assume that there are frequencies for which the energy and momentum are conserved, i.e.,

$$2\omega_p^0 - \omega_s^0 - \omega_i^0 = 0 \tag{2.35a}$$

$$\Delta k(\omega_p^0, \omega_p^0, \omega_s^0, \omega_i^0) = 0\,. \tag{2.35b}$$

Taking into account the aforementioned long scattering duration, Eq. (2.33) turns to:

$$\begin{aligned} |\psi(t)\rangle = {} & |0\rangle + \\ & \kappa L \mathcal{E}_0^2 \int d\omega_s \int d\omega_i \int d\omega_{p1} \left\{ e^{-\left(\frac{\omega_{p1}-\omega_p^0}{\sigma_p}\right)^2} e^{-\left(\frac{\omega_s+\omega_i-\omega_{p1}-\omega_p^0}{\sigma_p}\right)^2} \times \right. \\ & \left. e^{-i\frac{L\Delta k}{2}} \mathrm{sinc}\left(\tfrac{L\Delta k}{2}\right) a_s^\dagger(\omega_s)\, a_i^\dagger(\omega_i) \right\} |0\rangle \end{aligned} \tag{2.36}$$

where we consider a Gaussian spectral pump envelope

$$\mathcal{E}_p(\omega) = \mathcal{E}_0 e^{-\left(\omega-\omega_p^0\right)^2/\sigma_p^2} \tag{2.37}$$

centered at ω_p^0 with bandwidth (half width $1/e$ of amplitude) of σ_p and peak field $\mathcal{E}_0$. κ is a slowly varying function thus was evaluated at the central angular frequencies ω_μ^0 ($\mu = p, s, i$). The above assumed pump is referred to as *single-* or *degenerate-pump configuration*, emphasizing that the two pump fields are composed of a single laser pulse with single pump spectral peak.

Upon detection of the idler (or signal) photon, the projected state does not

include the vacuum, thus, the resulting state is the photon-pair as in Eq. (1.1) with the joint spectral amplitude:

$$\begin{aligned} f(\omega_s,\omega_i) &= \mathcal{N}\sqrt{\tfrac{2}{\pi\sigma_p^2}}\int d\omega_{p1}\left\{e^{-\left(\frac{\omega_{p1}-\omega_p^0}{\sigma_p}\right)^2}e^{-\left(\frac{\omega_s+\omega_i-\omega_{p1}-\omega_p^0}{\sigma_p}\right)^2}\times\right. \\ &\left. e^{-i\frac{L\Delta k}{2}}\operatorname{sinc}\left(\tfrac{L\Delta k}{2}\right)\right\}, \end{aligned} \tag{2.38}$$

where $\mathcal{N}$ is a normalization constant. We define the displacement frequencies $\nu_{s,i} = \omega_{s,i} - \omega_{s,i}^0$ and apply the integration transformation $\Omega = \omega_{p1} - \omega_p^0 - (\nu_s + \nu_i)/2$ in Eq. (2.38), to obtain

$$\begin{aligned} F(\nu_s,\nu_i) &= \mathcal{N}\sqrt{\tfrac{2}{\pi\sigma_p^2}}\times \\ &\int d\Omega\, e^{-\left(\frac{\nu_s+\nu_i}{2}+\Omega\right)^2/\sigma_p^2}e^{-\left(\frac{\nu_s+\nu_i}{2}-\Omega\right)^2/\sigma_p^2}e^{-i\frac{L\Delta k}{2}}\operatorname{sinc}\left(\tfrac{L\Delta k}{2}\right)\ , \end{aligned} \tag{2.39}$$

where $F(\nu_s,\nu_i) = f(\omega_s^0+\nu_s, \omega_i^0+\nu_i)$, and the vector-mismatch is defined here as

$$\begin{aligned} \Delta k(\nu_s,\nu_i,\Omega) &= k_p\left(\omega_p^0+\tfrac{\nu_s+\nu_i}{2}+\Omega\right)+k_p\left(\omega_p^0+\tfrac{\nu_s+\nu_i}{2}-\Omega\right) \\ &\quad -k_s(\omega_s^0+\nu_s)-k_i(\omega_i^0+\nu_i)\ . \end{aligned} \tag{2.40}$$

The vector-mismatch in Eq. (2.40) can be approximated by a first order Taylor expansion about the presumed zero, yielding

$$\begin{aligned} \Delta k(\nu_s,\nu_i,\Omega) &\cong k_p'\left[\tfrac{\nu_s+\nu_i}{2}+\Omega\right]+k_p'\left[\tfrac{\nu_s+\nu_i}{2}-\Omega\right]-k_s'\nu_s-k_i'\nu_i \\ &= (k_p'-k_s')\nu_s+(k_p'-k_i')\nu_i\ , \end{aligned} \tag{2.41}$$

where $k_\mu' = dk_\mu/d\omega|_{\omega=\omega_\mu^0}$. The above approximation is valid when the modes in-

volved in the SFWM experience a negligible dispersion. The resulting joint amplitude is then

$$\begin{aligned} F(\nu_s,\nu_i) &= \mathcal{N}\sqrt{\tfrac{2}{\pi\sigma_p^2}}e^{-i\frac{\tau_s\nu_s}{2}}e^{-i\frac{\tau_i\nu_i}{2}}\operatorname{sinc}\left(\tfrac{\tau_s\nu_s+\tau_i\nu_i}{2}\right)\times \\ &\qquad \int d\Omega\, e^{-\left(\frac{\nu_s+\nu_i}{2}+\Omega\right)^2/\sigma_p^2}e^{-\left(\frac{\nu_s+\nu_i}{2}-\Omega\right)^2/\sigma_p^2} \\ &= \mathcal{N}\sqrt{\tfrac{2}{\pi\sigma_p^2}}e^{-i\frac{\tau_s\nu_s}{2}}e^{-i\frac{\tau_i\nu_i}{2}}\operatorname{sinc}\left(\tfrac{\tau_s\nu_s+\tau_i\nu_i}{2}\right)e^{-\left(\frac{\nu_s+\nu_i}{\sqrt{2}\sigma_p}\right)^2}\times \\ &\qquad \int d\Omega\, e^{-\frac{2\Omega^2}{\sigma_p^2}}\ , \end{aligned} \tag{2.42}$$

with

$$\begin{aligned} \tau_s &= L(k_p'-k_s') \\ \tau_i &= L(k_p'-k_i') \end{aligned} \tag{2.43}$$

are the group delays introduced during the propagation in the fibre between the signal (τ_s) or idler (τ_i) and the pump. Thus, the joint spectral amplitude is evaluated to be[97]

$$F(\nu_s,\nu_i) = \left[\mathcal{N}e^{-i\frac{\tau_s\nu_s}{2}}e^{-i\frac{\tau_i\nu_i}{2}}\right]\alpha(\nu_s,\nu_i)\phi(\nu_s,\nu_i)\ , \tag{2.44a}$$

where

$$\alpha(\nu_s,\nu_i) = e^{-\left(\frac{\nu_s+\nu_i}{\sqrt{2}\sigma_p}\right)^2}\ , \tag{2.44b}$$

$$\phi(\nu_s,\nu_i) = \operatorname{sinc}\left(\frac{L\Delta k(\nu_s,\nu_i,\Omega=0)}{2}\right) \cong \operatorname{sinc}\left(\frac{\sin(\theta_{si})\nu_s-\cos(\theta_{si})\nu_i}{\sigma_{si}}\right)\ , \tag{2.44c}$$

and we have defined

$$\sigma_{si} = \left[\frac{2}{\sqrt{\tau_s^2 + \tau_i^2}}\right] \ , \ \theta_{si} = -\arctan(\tau_s/\tau_i) \ . \tag{2.45}$$

σ_{si} dictates, then, the width of the *phase-matching function* $\phi(\nu_s, \nu_i)$, while θ_{si} states its orientation. Figure 2.1 illustrates the joint spectral probability $|F(\nu_s, \nu_i)|^2$ according to Eqs. (2.44): the pump envelope $|\alpha(\nu_s, \nu_i)|^2$ is always oriented at an angle of -45^o, and the phase-matching function $|\phi(\nu_s, \nu_i)|^2$ was chosen with $\sigma_{si} = \sigma_p/5$ and orientation angle $\theta_{si} = -70^o$. The resultant joint spectral probability shows high correlations: any knowledge about the signal frequency bounds the idler to a specific central wavelength, and *vice-versa*. Consequently, the purity of the signal (or idler) is low, and the numerical calculations (using Eq. (1.10)) yield purity $p = 0.3559$. This kind of correlation is indeed typical in SPDC[98,99]. It has to be eliminated before one can utilize the process in schemes that rely on a HOM-interference.

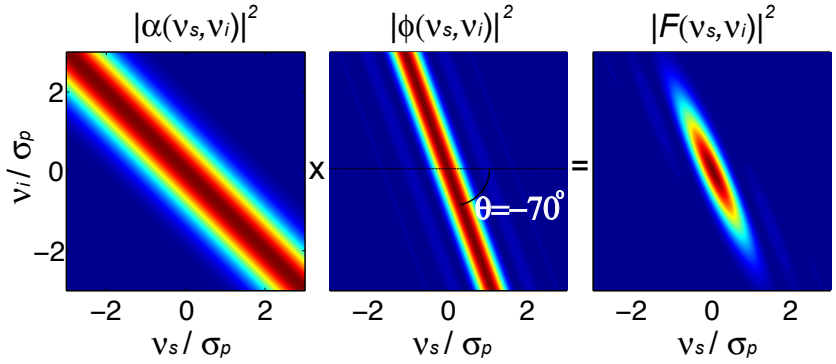


Figure 2.1 Pump envelope (left) and phase-matching (middle) functions for $\sigma_{si} = \sigma_p/5$ and $\theta_{si} = -70^o$. Their product (right), according to Eq. (2.44a) is the joint spectral probability.

2.5 Spectral filtering to reduce correlations

The most common way to avoid the correlations between the signal and idler photons is to spectrally filter one or both photons, and hence selecting only these photons with low correlations. Qualitatively, the idea is to choose such a narrowband idler (or signal) that it practically consists of a single spectral mode, and therefore cannot be correlated. Thus, the narrower the filter bandwidth, the lower the correlations and the purer each of the photons. However, narrowing the filter bandwidth means a reduction in the probability that the photon is transmitted through it, reducing the efficiency of the generation. Figure 2.2 illustrates the way the filtering scheme works. We assume a Gaussian filter applied to the idler photon. Upon transmission of the idler through the filter, the joint spectral amplitude is multiplied by the filter amplitude $\exp(-(\nu_i/\sigma_F)^2)$ (up to a normalization constant $\mathcal{N}$), where σ_F is the filter bandwidth, resulting in the filtered amplitude:

$$F_{filtered}(\nu_s, \nu_i) = \mathcal{N} F(\nu_s, \nu_i) \times e^{-(\nu_i/\sigma_p)^2} \ . \tag{2.46}$$

Using a filter with $\sigma_F = \sigma_p/5$, the purity of the state originally given by the joint spectral amplitude shown in Figure 2.1 is boosted to above 92%, and to 98% with $\sigma_F = \sigma_p/10$. This is however on the expense of losing the vast majority of the generated photons: in the former case, only about 17% of idler photons are transmitted through the filter, and in the latter less than 9% are. Often, one filters both the signal and idler arms. This allows less tight filters to achieve a decent purity. For example,

by using a bandpass filter for both sidebands with bandwidth $\sigma_F = \sigma_p/2$ the purity reaches 95%. However, although such a scheme may be experimentally advantageous (it is not always possible to find commercially available narrow enough bandpass filters), it does not provide any gain in terms of efficiency. For the aforementioned filtering, less than 15% of the pairs are transmitted coincidentally. Moreover, this technique degrades the heralding efficiency, as the detection of one photon does not guarantee its sibling has made it through the filter (in the case of filtering only one sideband, the heralding efficiency is unaffected if this sideband is used as the heralding photon). We conclude, then, that the use of spectral filters increases the purity of the heralded photons but harms appreciably the generation rate.

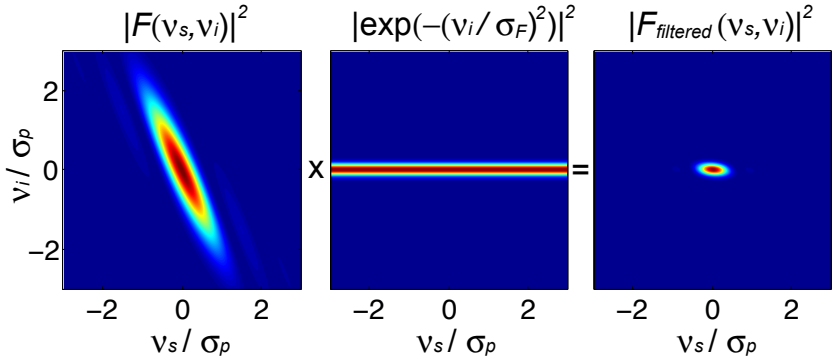


Figure 2.2 Filtering as a method to reduce correlations between the signal and idler. The joint spectral probability as obtained at the conditions depicted in Figure 2.1 (left), the filter transmission function with bandwidth $\sigma_F = \sigma_p/5$, and the resulting filtered joint probability (right). The use of this filter increases the purity from less than 36% to over 92%, but on the expense of losing about 83% of the pairs.

The degradation in the photon-pair production rate by itself might not be a significant fault in using a filter, as it is possible to compensate for the loss, e.g. by

increasing the pump power or extending the fibre length. However, doing so impairs the source as a reliable generator of heralded single-photons, as explained in the following: the photon-pair generation probability depends on the typical interaction strength, which can be incorporated into a parameter $\epsilon \ll 1$. The interaction may produce many photon-pairs in each pump pulse, with a probability to produce n pairs proportional to ϵ^n. Therefore, the first order – the one photon-pair – is the leading non-vacuum state. But, if we wanted to match the filtered generation rate with the one we would obtain if unfiltered, for example, in the case depicted in Figure 2.2, we would need to increase ϵ by about a factor of $5-10$. This means that the generation of two pairs would increase by a factor of $25-100$. Indeed, it has been observed that by increasing the pump power, higher photon-number generation harms appreciably the HOM-interference[89,90]. Therefore, when making a choice of a filter, one needs to compromise between purity, generation rate and higher-order contributions, while a scheme that produces factorable states intrinsically in the generation process increases immensely the reliability of the source as a heralded pure single-photon generator.

2.6 The step-index model

The central frequencies ω_s^0 and ω_i^0 at which phase-matching occurs, as well as the nature of the phase-matching function $\phi(\nu_s, \nu_i)$, depend on the dispersion of the fibre. A theoretical study of the phase-matching requires an adequate model for the propagation of light in fibres. In this section we describe a simple yet useful model.

An optical fibre is a thin glass or plastic waveguide in which light is confined by means of total internal reflection to within an area called the *core* of the fibre. Light travels through the fibre with small losses at bends and curves. The simplest model to describe a fibre is to assume a long cylindrical core with radius a, made of dispersive material with frequency (ω) dependent index of refraction $n_1(\omega)$. The core is suspended in a *cladding* made of a material with lower refractive index $n_2(\omega) < n_1(\omega)$, as illustrated in Figure 2.3. This model is called the *step-index model*, given after the shape of the index profile. The wave propagates along the core in the z direction, with an evanescent part in the cladding. We assume the cladding is large enough such that no medium beyond it takes part in the guiding.

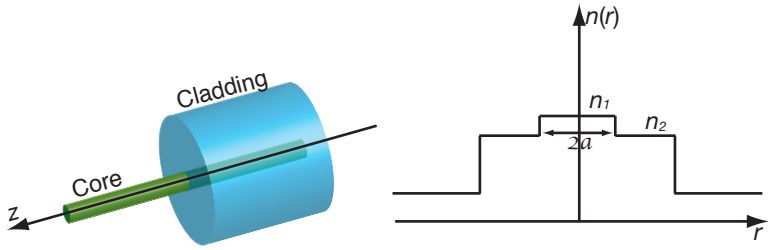


Figure 2.3 The step-index fibre: A core with radius a and refractive index n_1 is suspended in a cladding with refractive index n_2, such that $n_1 > n_2$.

By solving Maxwell's equations in the core and cladding, matching the solutions at the contact surface and looking at only solutions which propagate along the fibre with no loss (i.e. all of the energy flows in the z direction rather than out of the core), one finds that the effective propagation wave-vector β along the fibre is given

by the solution to the equation[100]:

$$\left(\frac{J_l'(ha)}{haJ_l(ha)}+\frac{K_l'(qa)}{qaK_l(qa)}\right)\left(\frac{n_1^2J_l'(ha)}{haJ_l(ha)}+\frac{n_2^2K_l'(qa)}{qaK_l(qa)}\right) = \left[\left(\frac{1}{qa}\right)^2+\left(\frac{1}{qa}\right)^2\right]\left(\frac{l\beta}{k_0}\right)^2 , \tag{2.47}$$

where $l = 0, 1, 2, 3, \ldots$, $q^2 = \beta^2 - n_2^2k_0^2$, $h^2 = n_1^2k_0^2 - \beta^2$, $k_0 = \omega/c$, c is the speed of light in vacuum, J_l and K_l are the Bessel function of the first kind and the modified Bessel function of the second kind respectively, of order l. This equation is quadratic in $J_l'(ha)/haJ_l(ha)$ and hence two classes of solutions arise, conventionally designated as EH and HE modes. Using mathematical identities, Eq. (2.47) turns to:

EH modes:

$$\frac{J_{l+1}(ha)}{haJ_l(ha)} = \left(\frac{n_1^2-n_2^2}{2n_1^2}\right)\frac{K_l'(qa)}{qaK_l(qa)} + \left(\frac{l}{(ha)^2}-R\right) , \tag{2.48a}$$

HE modes:

$$\frac{J_{l-1}(ha)}{haJ_l(ha)} = -\left(\frac{n_1^2-n_2^2}{2n_1^2}\right)\frac{K_l'(qa)}{qaK_l(qa)} + \left(\frac{l}{(ha)^2}-R\right) , \tag{2.48b}$$

where

$$R = \left[\left(\frac{n_1^2 - n_2^2}{2n_1^2} \right)^2 \left(\frac{K_l'(qa)}{qaK_l(qa)} \right)^2 + \left(\frac{l\beta}{n_1 k_0} \right)^2 \left(\frac{1}{(ha)^2} + \frac{1}{(qa)^2} \right)^2 \right]^{1/2} . \quad (2.48c)$$

For every l and class of modes (EH or HE), there might be several solutions β. For each such solution, one defines the effective index $n_{eff} = \beta/k_0$. The different modes are designated by EH_{lm} and HE_{lm}, where m is the sequential number of the solution in descending order of the associated values of n_{eff}. This index satisfies $n_2 < n_{eff} < n_1$.

A key feature of fibres of this kind is that the HE_{11} mode always exists. In addition, the other modes might have no propagating solutions, and in this case the fibre is said to be *single-mode*, as it supports only one spatial mode. Therefore, HE_{11} is also called the *fundamental mode* and the dispersion of single-mode fibres is given by the solution to Eqs. (2.48) for HE mode with $l = 1$ and for each angular frequency ω, yielding $\beta(\omega)$. Experimentally, one usually measures the *group velocity dispersion* (GVD) $\beta_2 = d^2\beta/d\omega^2$ or the *dispersion parameter* $D(\lambda)$ given by

$$D(\lambda) = \frac{d\beta_1}{d\lambda} = -\frac{2\pi c}{\lambda^2}\beta_2 , \quad (2.49)$$

where $\lambda = 2\pi c/\omega$ is the vacuum wavelength, $\beta_1(\lambda) = d\beta/d\omega|_{2\pi c/\lambda} = 1/v_g$ and v_g is the *group velocity* (GV) of that wavelength in the waveguide. The regime in which $D(\lambda) < 0$ is called *normal dispersion*, where the long wavelengths travel with GV higher than the short wavelengths. Conversely, $D(\lambda) > 0$ is the *anomalous*

dispersion regime.

It is common to look at the fibre dispersion as a composition of two parts: *material dispersion* and *waveguide dispersion*. The former refers to the wavelength dependency of n_1 and n_2, and the latter to the wavelength dependency of n_{eff} even in the absence of material dispersion. The waveguide dispersion always has an associated cutoff wavelength λ_c for which the fibre is single-mode for wavelengths $\lambda > \lambda_c$.

The use of a fibre supporting only a single mode for the pump and sideband wavelengths ensures that stresses on the fibre or imperfections in its manufacture do not result in a depletion of these waves to other spatial modes, thus affecting the phase-matching in an unknown way. However, requiring a fibre to guide only a single-mode in addition to other dispersion specifications enhances the complexity of fibre design (and might turn out to be impossible). The spatial profile of the fundamental mode is almost Gaussian[101] and hence is the mainly excited mode when a laser light is coupled into the fibre, even if the fibre can support several modes[102]. The sidebands can, in essence, be produced in a different spatial mode, provided these modes are supported by the fibre and the four-photon wavefunction overlap is good[103–105]. However, we assume here that all photons propagate in the fundamental mode, as this is the only mode guaranteed to be supported by a fibre waveguide. The fibre dispersion $k(\omega) = \beta(\omega)$ is taken, therefore, as given by the closest solution to $n_2\omega/c$ of Eqs. (2.48b) and (2.48c) with $l = 1$.

2.7 Phase-matching in fibres

The photons generated in SFWM in fibres, for a given pump with central frequency ω_p^0, are centered at the solution of the phase-matching equations (2.35). These solutions define the signal and idler angular frequencies, ω_s^0 and ω_i^0 respectively, as functions of the pump. Note that the phase-matching is trivially satisfied for $\omega_p^0 = \omega_s^0 = \omega_i^0$, giving rise to SPM. However, we are not interested in this case as it does not produce photon-pairs that can be isolated from the pump. One of the most commonly used ways to characterize a fibre is by specifying its *zero group velocity dispersion* (ZGVD) wavelengths λ_{ZGVD} at which $D(\lambda_{\mathrm{ZGVD}}) = 0$. One reason for the importance of λ_{ZGVD} is that solutions to the phase-matching equations typically exist only for pumps in the vicinity of these wavelengths [86,87,97,106], as explained by the following argument: the wave-vector can be expanded in Taylor series about the pump frequency ω_p^0, thus

$$k(\omega) = \sum_{n=0}^{\infty} \frac{1}{n!} \beta_n \left(\omega - \omega_p^0\right)^n \ , \tag{2.50}$$

where $\beta_n = d^n k / d\omega^n|_{\omega_p^0}$. Defining the detuning of the sidebands from the pump $\Omega_{si} = \omega_s^0 - \omega_p^0 = \omega_p^0 - \omega_i^0$, the phase-matching Eqs.(2.35) are written as:

$$-2 \sum_{n=1}^{\infty} \frac{1}{(2n)!} \beta_{2n} \Omega_{si}^{2n} = 0 \ . \tag{2.51}$$

For small enough detuning Ω_{si}, the main contribution to the above series comes from the lowest order term involving only the GVD (β_2). However, this term vanishes only for zero detuning. Therefore, phase-matching solutions can only exist when higher order terms become comparable to the β_2 term. This happens for pump close to λ_{ZGVD}.

We consider two commonly available fibres: the "standard" silica fibres and *photonic crystal fibres* (PCFs). A brief description of both is followed.

2.7.1 Standard silica fibres

Standard optical fibres are widely used in the telecommunications industry and other fields as low loss flexible waveguides. These fibres are usually made of silica threads. The core, cladding or both are doped with low concentration (typically less than 1%) of a dopant which changes the refractive index of the pure silica. Germanium dioxide and aluminium oxide are usually used to increase the core index, while the cladding is commonly doped with fluorine, boron trioxide or rare earth metals to decrease the index. As was mentioned earlier, the effective propagation index in fibres always lies between the refractive indices of the core and cladding. In standard fibres, the index contrast between the doped and pure silica is so low that the waveguiding configuration affects only slightly the dispersion. Hence, normally $\lambda_{ZGVD} \approx 1.3\,\mu m$ around the ZGVD wavelength of pure silica, and can be shifted towards longer wavelengths[107] by changing the core size, type and concentration of dopant as well as the index transition profile between core and cladding (i.e. beyond the simple

step-index profile). This means that solutions to the above phase-matching equation exist only for a pump in the infrared.

2.7.2 Photonic-crystal fibres

Photonic crystal fibres, commonly also referred to as *microstructured fibres*, are fibres with a periodic cross-section structure. Such a fibre was first fabricated in 1996 [108] by a group of researchers at the University of Southampton headed by Philip Russell. These type of fibres have attracted a lot of attention due to the versatility of the structures that can be manufactured, giving a huge flexibility in controlling the modes propagating through them and dispersion of these modes [108–110]. Particularly, their ZGVD wavelengths can be shifted towards the visible light. One class of these fibres are the highly nonlinear ones, made of silica, with air-holes in the cladding cross-section. A scanning electron microscope image of the cross-section of such fibres is illustrated in Figure 2.4. The light is guided in the silica core, while the air-holes contribute to an effective cladding refractive index. This configuration realizes a fibre with high index contrast between the core and cladding, confining the guided light to within the small diameter of the core (typically about 2 μm). As a result, high intensity light propagates over a long distance, giving rise to a long and strong nonlinear interaction.

The effective index $n_{eff}(\omega)$ in a PCF can be relatively accurately modeled using the step-index model [102,111], with a d diameter of core having a refractive index of

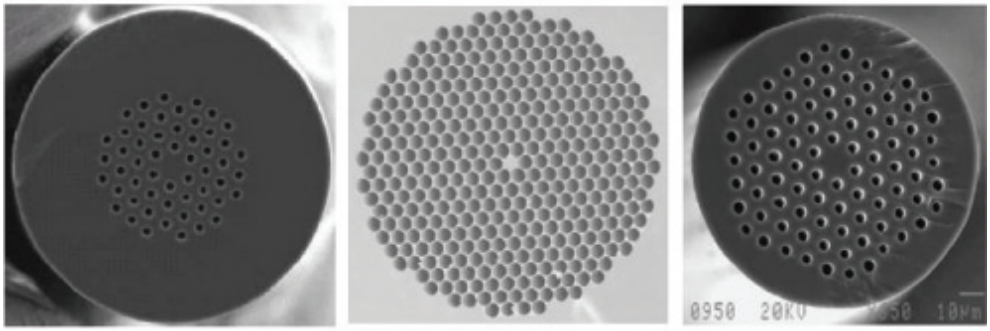


Figure 2.4 examples of scanning electron microscope images of PCFs ($10\,\mu$m $\times$ $10\,\mu$m). The core is the "missing hole" at the centre, and the periodic structure of air-holes acts as the cladding. The versatility in the structures that can be manufactured supplies high flexibility in producing fibres with various guiding characteristics. Images are taken from the website of KAIST: http://fiber.kaist.ac.kr/home.htm

silica $n_{silica}(\omega)$ and cladding refractive index of

$$n_{cladding}(\omega) = r + (1 - r)n_{silica}(\omega) \,, \tag{2.52}$$

where r is the air filling fraction in the cladding. Thus, d and r characterize the fibre within this model. The index of pure silica is well approximated by the Sellmeier equation[112] – an empirical relationship, based on the resonances of the medium, that relates the light frequency to the refractive index of the bulk material. It is applicable for frequencies far enough from those resonances, and given by:

$$n(\omega) = \sqrt{1 + \sum_{j=1}^{m} \frac{B_j \omega_j^2}{\omega_j^2 - \omega^2}} \,, \tag{2.53}$$

where the parameters B_j and ω_j are obtained experimentally by fitting a measured

dispersion curve, usually with $m = 3$. For bulk fused silica, these parameters are found to be[113]:

$$\begin{aligned} &B_1 = 0.6961663 \quad B_2 = 0.4079426 \quad B_3 = 0.6961663 \\ &\lambda_1 = 68.4043\,\text{nm} \quad \lambda_2 = 116.2414\,\text{nm} \quad \lambda_3 = 9896.161\,\text{nm}\,, \end{aligned} \tag{2.54}$$

where $\lambda_j = 2\pi c/\omega_j$.

Taking all the constituents of the step-index model, calculating the effective index n_{eff} for a specific wavelength λ with associated angular frequency $\omega = 2\pi c/\lambda$, in a PCF with core diameter d and air filling fraction r, is done with the following steps:

1. Calculate the refractive index $n_{silica}(\omega)$ for this wavelength using the Sellmeier equation Eq. (2.53) with (2.54).

2. Define $n_1 = n_{silica}(\omega)$ as the core index and calculate $n_2 = r + (1-r)n_{silica}(\omega)$ as the cladding index.

3. Find (numerically) the greatest β that solves Eq.(2.48b) with (2.48c), after substituting $a = d/2$, $l = 1$, $q^2 = \beta^2 - n_2^2 k_0^2$, $h^2 = n_1^2 k_0^2 - \beta^2$, $k_0 = \omega/c$ and the core and cladding indices calculated in step (2).

4. calculate the effective index for the chosen wavelength as $n_{eff}(\lambda) = \beta\lambda/2\pi$.

Solving Eq. (2.48b) (in step (3)) is computationally consuming and inefficient when one needs to calculate the index for a large number of wavelengths. We avoid excessive use of the above procedure by calculating the effective index only for N

different wavelengths equally separated within our working range 400 to 3000 nm. Thus, we obtain a set of wavelengths $\{\lambda_i\}$ with their associated index $n_{eff}(\lambda_i)$. We then fit the calculated refractive indices with a polynomial of order p,

$$n_{fit}(\lambda) = \sum_{j=0}^{p} C_j \left(\frac{\lambda - \mu_1}{\mu_2} \right)^j , \tag{2.55}$$

where μ_1 and μ_2 are, respectively, the mean value and standard-deviation of the set $\{\lambda_i\}$, and C_j are the fitting coefficients. We found that taking $N = 1000$ and $p = 30$ was satisfactory for us.

For a given fibre, one needs to calculate n_{eff} only N times for $\{\lambda_i\}$ with steps (1)-(4). Then fit the data with a polynomial to obtain the $\{C_j\}$ coefficients. Once this is done, the effective index in the fibre can be quickly calculated using Eq. (2.55), as well as the wave-vector

$$k(\omega) = \frac{\omega}{c} n_{fit} \left(\frac{2\pi c}{\omega} \right) . \tag{2.56}$$

It is also easy to calculate the derivatives $\beta_n = d^n k / d\omega^n$ utilizing the polynomial coefficients.

Using the conservation constraints Eqs. (2.35), the angular frequency ω_i^0 at which the idler is created, for a given pump centered at ω_p^0, is given by the solution to

$$2k(\omega_p^0) - k(\omega_i^0) - k(2\omega_p^0 - \omega_i^0) = 0 . \tag{2.57a}$$

The signal central frequency is then evaluated by

$$\omega_s^0 = 2\omega_p^0 - \omega_i^0 \ . \tag{2.57b}$$

To illustrate the usage of the model, we choose a nonlinear PCF with typical parameters of $d = 1.8\,\mu m$ and $r = 0.45$. We calculate the dispersion parameter $D(\lambda)$ for the desired range of wavelengths, plotted in Figure 2.5 (left). The ZGVD wavelengths are found at 784 nm and 1497 nm.

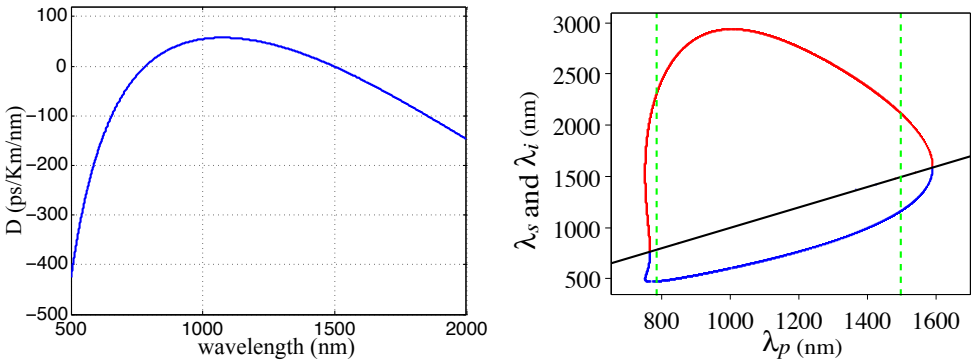


Figure 2.5 Plots based on the step-index model for a silica PCF with core diameter $d = 1.8\,\mu$m and cladding air filling fraction $r = 0.45$. Left: the dispersion parameter D as a function of wavelength. The ZGVD wavelengths are 784 nm and 1497 nm. Right: the phase-matching contour for this fibre. The green dashed vertical lines mark ZGVD wavelengths, and the black line corresponds to $\lambda_s = \lambda_i = \lambda_p$ which trivially obeys the conservation constraints.

Figure 2.5 (right) also shows the phase-matching contour, which presents the solutions to Eqs. (2.57). The procedure to plot this curve is as follows: create a grid Z who's horizontal axis corresponds to pump frequencies and the vertical to

signal-idler frequencies. Then calculate

$$Z(\omega_p^0, \omega^0) = 2k(\omega_p^0) - k(\omega^0) - k(2\omega_p^0 - \omega^0) \; . \tag{2.58}$$

A contour of $Z = 0$ results in a plot of the phase-matching solutions to Eqs. (2.57). One may also multiply the elements of Z by $(1 - \mathrm{sign}(\omega_p^0 - \omega^0))$ to obtain only the idler solutions (top red) or by $(1 + \mathrm{sign}(\omega_p^0 - \omega^0))$ for the signal solutions (bottom blue).

Both the dispersion and the phase-matching curves are typical, and the major differences between various PCFs are a shift and scale according to their ZGVD points.

2.8 Practical considerations for choosing a fibre

The realization of a useful photon-pair source depends on the availability of equipment to implement and make use of it: a laser that can pump at the correct wavelength, optical elements such as mirrors, polarizing and non-polarizing beamsplitters *etc.* with good functionality at the relevant wavelengths. Particularly important is the existence of efficient single-photon detectors at the sideband wavelengths. Moreover, one also needs to take into account contamination from Raman scattering which degrades the reliability of the source as photon-pairs producer. In the following we list the restrictions that limited the fibre characteristics we considered.

2.8.1 Detection bandwidth

Every experiment or application with single photons demands detectors capable of signaling the existence of fundamental quanta of energy. Unlike detectors or meters for macroscopic fluxes, present (electric) current amplifiers cannot be employed in the quantum regime, because of the intrinsic noise in the amplification. Single-photon sensitive detectors, therefore, work in the avalanche regime, where a single photon stimulates a chain reaction that multiply the current to a macroscopic level. Thus, the detection of a photon is indicated by an electric pulse, with a large number of electrons that varies from event to event.

Ideally, a photon detector: 1) Has high quantum efficiency, i.e., the probability of a photon to trigger the detector is high. 2) Low dark counts – the probability for false signaling is low. Dark counts are usually caused by thermal excitations, quantum tunneling and also trapped carriers leftover from a previous detection, called after-pulsing. 3) Response time – the detector fires shortly after the photon passes through it, with small jitter time. 4) Short recovery time – shortly after the detection, the detector is ready to detect another photon.

There are two types of single-photon detectors commercially available to date. Those are the photo-multiplier tube (PMT) and avalanche photodiode (APD).

A PMT is based on the acceleration of electrons in a vacuum chamber. An incident photon releases an electron from a photocathode, which is then accelerated towards a higher potential dynodes. Upon striking the first dynode, the highly energetic electron releases more electrons, which are accelerated towards a subsequent

dynode. Several dynodes are used to multiply the current to a macroscopic magnitude by the time they reach the anode. The quantum efficiency of PMT is about 30% at its peak efficient wavelength ($\sim 300\,\text{nm}$), they can work at a repetition rate up to a few MHz, the jitter on the rise time is on the scale of a ns, and the dark counts can be on the order of 100 or even less per second.

APDs are diodes operated in the so called *Geiger mode*: the diode is biased by a reverse voltage above its breakdown voltage. An incident photon creates an electron-hole pair. These carriers are accelerated by the applied voltage, triggering an avalanche consisting of thousands or even millions of carriers. The APD then needs to be reset to stop the the current and prepare it for the next detection, a process referred to as *quenching*. There are three semiconductor types on which commercial APDs are based: silicon APDs are suitable for the detection in the visible wavelength region, germanium-based APDs are useful for the second telecommunication window ($1.3\,\mu\text{m}$) and InGaAs/InP APDs can operate at the third window ($1.55\,\mu\text{m}$). To date, the best detectors are the silicon-based APDs, with detection efficiency capable of exceeding 60% with about a hundred of dark counts per second (and even less), typical 300 ps rise time spread and count rate of up to few MHz. These properties make them the most desirable detectors for single-photon resolution. Their detection efficiency is relatively high (above 20%) over the bandwidth $450 - 900$ nm.

The usefulness of the silicon APD as a single-photon detector drove us to design our source to generate photon-pairs within this APD's detection bandwidth.

2.8.2 Pump

As we'll see in the following chapter, the choice of pump, including its bandwidth and central wavelength, is one of the most important resources used in this thesis. Tunability, therefore, is essential. In order to produce both sidebands inside the APDs' detection bandwidth, the pump itself must lie within this bandwidth. The above requirements raised the mode-locked femtosecond Titanium-Sapphire laser as our best candidate, operating at wavelengths around 800 nm. Specifically, the system we had could be tuned between $770 - 830$ nm. The bandwidth of ~ 20 nm ccould be narrowed down using filters.

2.8.3 Raman background

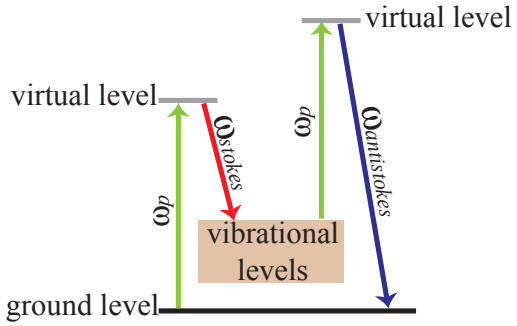


Figure 2.6 The Raman scattering. Stokes: a photon with frequency ω_p is scattered, transferring energy to the vibrational levels of the medium and ends up with frequency $\omega_{stokes} < \omega_p$. Anti-Stokes: A photon with frequency ω_p acquires energy from the vibrational levels and shifts to the frequency $\omega_{antistokes}$.

In addition to the parametric process of FWM, another dominant interaction in fibres is Raman scattering[114], a phenomenon discovered by the Indian physicist Sir

Chandrasekhara Raman. This interaction couples the electromagnetic field and the vibrational levels of the medium – optical phonons, as illustrated in Figure 2.6. In the quantum picture, a pump photon with angular frequency ω_p is absorbed, another photon, called the *Stokes photon* with frequency $\omega_{stoke} < \omega_p$ is created along with a phonon with energy $\hbar\omega_{phonon} = \hbar(\omega_p - \omega_{stokes})$. Once the vibrational levels of the medium are populated, the pump interacts with the existing phonons to create what is called *anti-Stokes photons* with frequency $\omega_{antistokes} = \omega_p + \omega_{phonon}$. If the pump power is low enough, the probability for the Raman interaction to take place is low and hence one needs to consider the spontaneous Raman-scattering: only one pump photon interacts with the medium to create a Stokes photon. The energy of optical phonons is almost independent of their momentum, meaning that phase-matching can always be satisfied as the phonon "can pick up" the required momentum. Therefore, the Stokes photons are created red-shifted relative to the pump by an angular frequency Ω which is independent of the pump wavelength, with probability proportional to the state-density of the $\omega_{phonon} = \Omega$ energy level. The normalized Raman gain $g_R(\Omega)$ for fused silica is shown in Figure 2.7[115]. A significant feature of this gain is that it extends over a large frequency bandwidth (up to 40 THz) with several overlapping peaks, as opposed to crystalline materials where the Raman gain shows narrow isolated peaks. This is attributed to the spread of the molecular vibrational frequencies into bands that overlap, which is a typical energy level structure of amorphous materials like fused silica.

In essence, the first order perturbation regime can bring a pump photon and

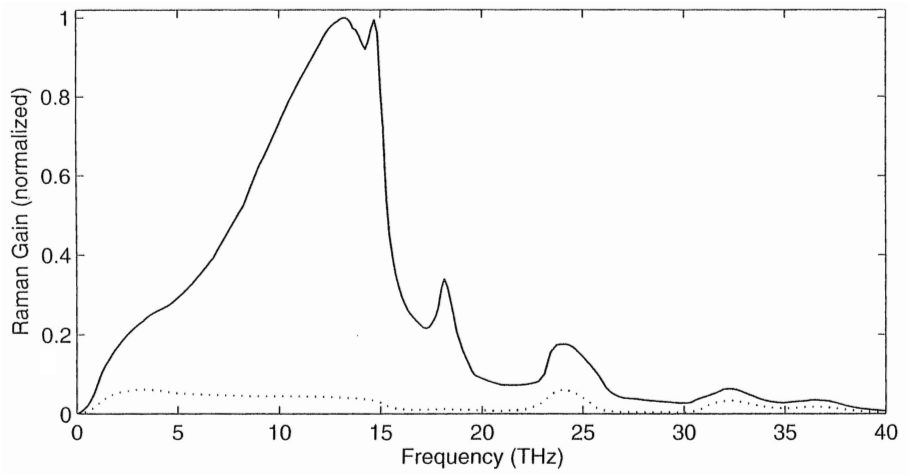


Figure 2.7 Normalized Raman gain ($g_R(\Omega)$) for fused silica (measured at room temperature) as a function of the detuning from the pump frequency. The solid line indicates the gain polarized parallel to the pump, while the dashed line is for orthogonal polarization (reprinted from Reference [112], with permission from Elsevier).

an existing phonon to interact and create anti-Stokes photons. Moreover, existing phonons can stimulate the emission of Stokes photons. The probability of a certain site to generate an *anti-Stokes* photon with angular frequency shift Ω is proportional to the phonon population [116] $n(\Omega)$ at that site. The generation of *Stokes* photons with this shift is proportional to $(n(\Omega)+1)$. The difference between the two processes probabilities stems from the ability of the Stokes emission to occur spontaneously even in the absence of phonons. The medium's vibrational levels are thermally populated and given by Bose-Einstein statistics: $n(\Omega) = [\exp(\hbar\Omega/KT) - 1]^{-1}$ where K is Boltzmann constant and $T \approx 300\,\mathrm{K}$ is the room temperature. For detuning $\Omega > 20\,\mathrm{THz}$, $n(\Omega) < 0.05$, and any process which relies on existing phonons is negligible compared with the spontaneous Raman. It follows, then, that the vast majority of Raman photons are created spontaneously, hence appear at the idler arm.

It is therefore desirable to have the idler created far enough from the pump, i.e. such that $\omega_p^0 - \omega_i^0 > 40$ THz, where the Raman gain is insignificant. For pump wavelength at around 800 nm, this means about 100 nm shifted idler from the pump. It has been shown that one can decrease the Raman background by immersing the fibre in liquid nitrogen[117] or liquid helium[118,119], cooling it to 77 K and 4 K respectively, hence suppressing the population of thermal phonons and stimulated Raman with it. However, the approach is practically difficult to implement with relatively short fibre lengths of about or less than 1 m.

2.8.4 Fibre type

Standard fibres are very cheap compared to their PCF counterpart, their manufacturing industry is quite mature and reliable, and in addition their dispersion is well known (close to pure silica for any practical purpose we consider here). However, their nonlinearity is typically a lot weaker than in PCFs due to larger core and small index contrast that extend the mode transverse profile over a larger area, resulting in lower intensity. Moreover, no phase-matching normally occurs using them in the restricted bandwidth we require. Hence, we first concentrate on generating factorable photon-pair states in PCFs. We'll later study the implementation of our approach in standard fibres.

Chapter 3

Factorable photon-pair state

This chapter, whose main results are published in Reference [97], investigates theoretically the conditions under which the photon-pairs generated in optical fibers are factorable. We use the step-index model as our resource to model the dispersion in PCFs, and spot the practical difficulties in realizing the desired conditions. We then investigate different configurations of SFWM and find that the model predicts the possibility of generating experimentally realizable uncorrelated photon-pairs in birefringent PCFs.

3.1 Tailoring the spectral photon-pair properties

Eqs. (2.44) have the same form as the joint amplitude obtained for SPDC [98], hence, the approach taken in Reference [92] towards tailoring the joint spectrum of the downconverted photons in SPDC is applicable for SFWM, and we follow here the treatment developed there.

Note that the spectral correlations appear in $\alpha(\nu_s, \nu_i)$ and $\phi(\nu_s, \nu_i)$, the former expresses the energy conservation constraint while the latter expresses momentum conservation. The group delays τ_s and τ_i depend on the fibre length and dispersion, and it is those properties (along with the pump bandwidth σ_p) that can be controlled. In other words, we utilize the ability to manipulate the momentum in fibres, and hence its conservation constraint, to factorize the joint spectral amplitude. In order to understand the effect of the phase-matching on the correlations, it is useful to further simplify the joint amplitude by approximating the sinc function as a Gaussian with the same full-width half-maximum (FWHM):

$$\mathrm{sinc}(x) \approx e^{-bx^2} \ , \ b = 0.193 \ . \tag{3.1}$$

With this approximation, Eqs. (2.44) turn into

$$\begin{aligned} F(\nu_s, \nu_i) \ = \ & \mathcal{N} \left[e^{-i\frac{\sin\theta_{si}}{\sigma_{si}}\nu_s} e^{-\left(\frac{1}{\sqrt{2}\sigma_p} + \frac{\sqrt{b}\sin\theta_{si}}{\sigma_{si}}\nu_s\right)^2} \right] \times \\ & \left[e^{i\frac{\cos\theta_{si}}{\sigma_{si}}\nu_i} e^{-\left(\frac{1}{\sqrt{2}\sigma_p} - \frac{\sqrt{b}\cos\theta_{si}}{\sigma_{si}}\nu_i\right)^2} \right] \times \\ & \exp\left(- \left(\frac{1}{\sigma_p^2} - \frac{b\sin(2\theta_{si})}{\sigma_{si}^2} \right) \nu_s \nu_i \right) \ . \end{aligned} \tag{3.2}$$

Hence, the correlations – the non-factorable term in the third line – vanish when

$$\frac{1}{\sigma_p^2} - \frac{b\sin(2\theta_{si})}{\sigma_{si}^2} = 0 \ . \tag{3.3}$$

Assuming we can choose a pump bandwidth to our will, factorability is accomplish-

able if and only if

$$0^o \leq \theta_{si} \leq 90^o \, . \tag{3.4}$$

In terms of the group delays, condition (3.4) is written as $\tau_s \tau_i \leq 0$, i.e., the group delays carry opposite signs, meaning that one sideband need to lag after the pump, while the other travels with group-velocity (GV) greater than the pump.

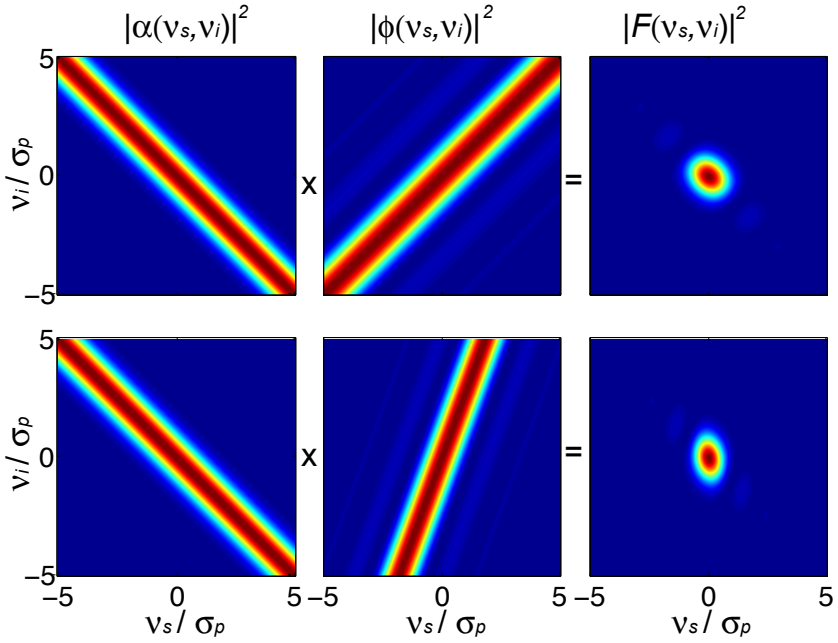


Figure 3.1 Joint spectral probabilities with low correlations, showing the pump envelope (left), phase-matching function (middle) and their product corresponding to the joint probability (right) for the cases $\theta_{si} = 45^o$ with $\sigma_{si} = 0.5425\sigma_p$ (top) and $\theta_{si} = 70^o$ with $\sigma_{si} = 0.4168\sigma_p$ (bottom). The corresponding purity is $p = 0.8552$ and $p = 0.8600$, respectively.

Figure 3.1 illustrates joint probabilities with low correlations: the top subsets show the pump envelope, phase-matching function and the resultant joint probability for $\theta_{si} = 45^o$, while at the bottom the case $\theta_{si} = 70^o$ is shown. In both cases σ_{si}

was optimized to produce maximal purity. In the former case, $\sigma_{si} = 0.5425\sigma_p$ and the corresponding purity $p = 0.8552$, in the latter case the optimization yielded $\sigma_{si} = 0.4168\sigma_p$ with $p = 0.8600$.

Note that the purity associated with the amplitude in Eqs. (2.44) depends on the goodness of approximating the sinc function as a Gaussian, and for each given angle $0 < \theta_{si} < 90^o$ a maximal purity $p < 1$ can be obtained. The angles $\theta_{si} = 0^o$ and $\theta_{si} = 90^o$ are special, though: in these cases, $\phi(\nu_s, \nu_i)$ acts in the same way a filter acts on the idler or signal, respectively (but introduces no loss). As $\phi(\nu_s, \nu_i)$ becomes narrower with respect to $\alpha(\nu_s, \nu_i)$, i.e. $\sigma_{si}/\sigma_p \to 0$, the idler ($\theta_{si} = 0^o$) or signal ($\theta_{si} = 90^o$) spectra become narrower, approximately a single spectral mode, and thus avoid correlations. For example, Figure 3.2 shows the case with $\theta_{si} = 0^o$ and $\sigma_{si} = \sigma_p/10$, resulting in associated purity of 0.9453. The purity increases to 0.9725 with narrower phase-matching function $\sigma_{si} = \sigma_p/20$. One might find the temporal domain argument more intuitive here: temporally, $\theta_{si} = 0^o$ expresses the regime in which the signal travels with the same GV as the pump. The idler, which travels at a different GV, is created at the location of the pump but then drifts away. The displacement between the idler and the pump depends on the location inside the fibre at which the sidebands are created: if they are generated at the beginning of the fibre, then the idler is maximally displaced from the pump by the time delay τ_i. If, on the other hand, the creation occurs at the output end of the fibre, then the idler emerges at the same location as the pump. Thus, the temporal degree of freedom of the idler photon, in the above GV-matching case, encodes the information about

the location at which the SFWM interaction has taken place with a resolution equal to the temporal duration of the pump. Conversely, the signal photon emerges from the fibre with the pump irrespective of where it was created, bearing no information on the whereabout of the interaction. This particular imbalance in the information sharing – one photon "knows everything" while the other "knows nothing" is in essence lack of correlations between the ("knowledge" of the) two photons.

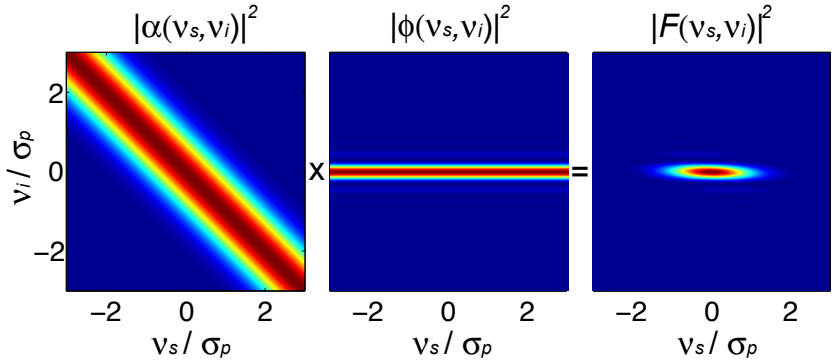


Figure 3.2 The joint spectral probability for $\theta_{si} = 0^o$ and $\sigma_{si} = \sigma_p/10$. The corresponding purity is $p = 0.9453$.

In Figure 3.3 the maximal purity that can be obtained for each orientation θ_{si} is plotted. The corresponding phase-matching width σ_{si} is also shown. Since the horizontal ($\theta_{si} = 0^o$) and vertical ($\theta_{si} = 90^o$) orientations provide the potential of reaching 100% purity, we opt to concentrate on the experimental realization of such cases.

The main contribution to the impurity in the cases other than the horizontal and vertical orientations arises from the sidelobes related to the sinc function (see Figure 3.1). These sidelobes, however, contain only a small fraction of the total flux:

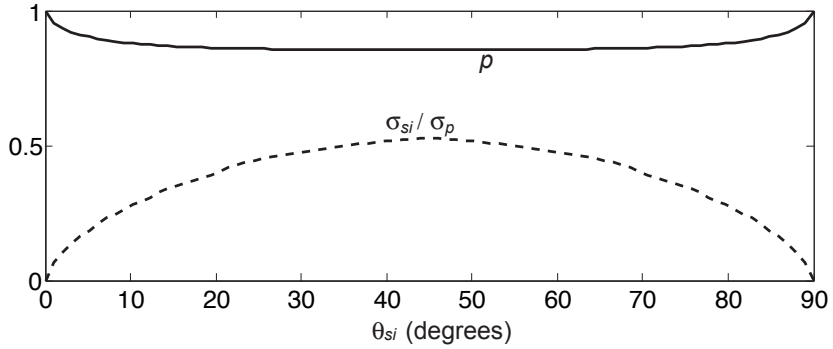


Figure 3.3 The maximal purity (solid curve) that can be obtained by optimizing the phase-matching function width (dashed curve), assuming the amplitude given by Eqs. (2.44).

the joint spectral probability is given by

$$P(\nu_s,\nu_i)=\frac{|\tilde{\alpha}\left(\nu_s+\nu_i\right)|^2|\tilde{\phi}\left(\left(\sin\theta_{si}\nu_s-\cos\theta_{si}\nu_i\right)/\sigma_{si}\right)|^2}{\int_{-\infty}^{\infty}\int_{-\infty}^{\infty}|\tilde{\alpha}(\nu_s+\nu_i)|^2|\tilde{\phi}\left(\left(\sin\theta_{si}\nu_s-\cos\theta_{si}\nu_i\right)/\sigma_{si}\right)|^2d\nu_s d\nu_i}\ , \tag{3.5}$$

where

$$\tilde{\alpha}(\nu_s+\nu_i)=\alpha(\nu_s,\nu_i) \tag{3.6}$$

and

$$\tilde{\phi}\left(\left(\sin\theta_{si}\nu_s-\cos\theta_{si}\nu_i\right)/\sigma_{si}\right)=\phi(\nu_s,\nu_i)=\mathrm{sinc}\left(\left(\sin\theta_{si}\nu_s-\cos\theta_{si}\nu_i\right)/\sigma_{si}\right)\ . \tag{3.7}$$

By applying the transformation $x=\nu_s+\nu_i$ and $y=(\sin\theta_{si}\nu_s-\cos\theta_{si}\nu_i)/\sigma_{si}$, the joint probability turns to:

$$\tilde{P}(x,y)=\frac{|\tilde{\alpha}\left(x\right)|^2|\tilde{\phi}\left(y\right)|^2J}{\int_{-\infty}^{\infty}\int_{-\infty}^{\infty}|\tilde{\alpha}(x)|^2|\tilde{\phi}\left(y\right)|^2Jdxdy}\ , \tag{3.8}$$

where $J = |(\cos\theta_{si} + \sin\theta_{si})/\sigma_{si}|$ is the Jacobian of the transformation. As it does not depend on x or y, it cancels in the numerator and denominator. The central lobe area is bounded by the pump bandwidth across the x-variable direction, while along the y direction it is bounded by the zeros of the sinc function adjacent to the origin, i.e. $y = \pm\pi$. Hence, the probability of finding the photon-pair within the central lobe is given by:

$$\int_{-\infty}^{\infty} dx \int_{-\pi}^{\pi} dy \tilde{P}(x,y) = \frac{\int_{-\pi}^{\pi} dy |\tilde{\phi}(y)|^2}{\int_{-\infty}^{\infty} dy |\tilde{\phi}(y)|^2} = \frac{\int_{-\pi}^{\pi} dy \,\mathrm{sinc}^2(y)}{\int_{-\infty}^{\infty} dy \,\mathrm{sinc}^2(y)} \cong 0.903 \,. \tag{3.9}$$

Thus, the central lobe contains (more than) 90% of the total flux. If one restricts oneself only to photon-pair states in this lobe, the joint spectral amplitude is evaluated with the phase-matching function

$$\phi(\nu_s, \nu_i) = \begin{cases} \mathrm{sinc}\left(\frac{\sin\theta_{si}\nu_s - \cos\theta_{si}\nu_i}{\sigma_{si}}\right), & \left|\frac{\sin\theta_{si}\nu_s - \cos\theta_{si}\nu_i}{\sigma_{si}}\right| < \pi \\ 0, & \text{otherwise} \end{cases} \tag{3.10}$$

and the corresponding purity for $\theta_{si} = 45^o$ with $\sigma_{si} = 0.5425\sigma_p$ (same configuration as the top subsets in Figure 3.1) is $p = 0.9854$. However, in practice one cannot choose which pairs to select, but can pick specific signal and idler bandwidths independently by spectrally filtering. Filtering the original joint amplitude (with the sidelobes) at both arms using a rectangular spectral filter with transmission window bandwidth of $3\sigma_p$, the purity increases to $p = 0.98$ (from the unfiltered value of $p < 0.86$) while loosing only 6% of the total flux [97].

As was already stated, condition (3.4) is satisfied whenever the pump travels at GV between the signal and idler's velocities. Specifically, the horizontal case is obtained when the signal GV matches the pump. The vertical case is obtained when GV-matching occurs between the idler and pump. In the following section, we describe a method of identifying the pump wavelength at which GV-matching occurs.

3.2 Identifying the group-velocity matching point

Finding the GV-matching point requires precise knowledge of the fibre dispersion. Measuring the dispersion is relatively complicated and typically not accurate enough for our purpose. It is experimentally easy, however, to measure the sideband wavelengths as a function of the pump, and here we describe how one can extract from the phase-matching contour the point of GV-matching: for a given central pump frequency x, the central signal and idler frequencies are given by the solutions to Eqs. (2.35). Those conditions can be combined to form the equaiton:

$$2k_p(x) - k_s(2x - y) - k_i(y) = 0 \,, \tag{3.11}$$

where y is the idler central frequency. The signal frequency $2x - y$ is implied by energy conservation. k_μ ($\mu = p, s, i$ for pump, signal and idler respectively) is the effective wave-vector of the propagating mode. This notation does not restrict the involved fields to be of the same mode – they could differ either spatially [120,121] or

in polarization[122]. We'll see later how the use of the different polarization modes provides us with a flexibility crucial to implement our scheme.

Eq. (3.11) forms the implicit function $y(x)$. Differentiating it with respect to x yields:

$$2k_p'(x) - \left[2 - y'(x)\right] k_s'(2x - y) - y'(x)k_i'(y) = 0 \,, \tag{3.12}$$

where $k_\mu'(z) = (dk_\mu(w)/dw)|_{w=z}$ and y' is the derivative of y. Rearranging this equation and using the definitions in Eqs. (2.45) with (2.43), the above phase-matching equation can be written as

$$y'(x) = \frac{2}{1 + \cot\theta_{si}} \,. \tag{3.13}$$

Factorability is possible for $0^o \leq \theta_{si} \leq 90^o$, when the slope of the idler frequency satisfies $0 \leq y'(x) \leq 2$. Similarly, the curve of the signal central wavelength $z(x) = 2x - y(x)$ satisfies

$$z'(x) = \frac{2}{1 + \tan\theta_{si}} \,, \tag{3.14}$$

and again, $0 \leq z'(x) \leq 2$ correspond to an orientation of the phase-matching function capable of showing factorability. Specifically, $y'(x) = 0$ (and implied $z'(x) = 2$) corresponds to the case where GV-matching occurs between the signal and pump, while $z'(x) = 0$ (and implied $y'(x) = 2$) is where the idler GV matches the pump.

Thus, by looking at the phase-matching contour, we can identify the GV-matching wavelengths by spotting the point where one of the sideband wavelengths is indepen-

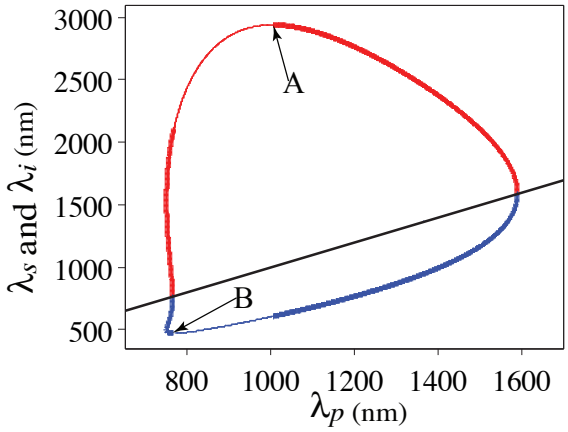


Figure 3.4 Phase-matching contour for a PCF with core diameter $d = 1.8\,\mu$m and cladding air filling fraction $r = 0.45$. Top (red) and bottom (blue) curves correspond, respectively, to the idler and signal phase-matching wavelengths. The GV-matching between the pump and signal (idler) is indicated by point A (B), where the idler (signal) wavelength is independent of the pump. Thin sections indicate points at which factorability is possible ($0^o \leq \theta_{si} \leq 90^o$).

dent, to first order, of the pump. Figure 3.4 presents the phase-matching contour for a fibre with core diameter $d = 1.8\,\mu$m and air filling fraction $r = 0.45$ (same fibre-parameters as in Figure 2.5). We can identify two GV-matching points: at point A the pump, signal and idler wavelengths are 1002 nm, 604 nm and 2939 nm respectively. The idler wavelength at this point is independent of the pump and the signal GV matches the pump. Point B, with the respective wavelengths 769 nm, 470 nm and 2108 nm, is where the GVs of idler and pump are equal. However, the idler produced at both of these points is far beyond the APDs detection bandwidth, and hence useless for our purpose. Unfortunately, this is the case for any reasonable PCF; for example, in a fibre with the parameters $d = 1.15\,\mu$m and $r = 50\%$, the signal and idler can be created at 684 nm and 905 nm, respectively, with the signal

GV matching the pump. Nonetheless, manufacturing a PCF with such a small core diameter is not technologically available. Moreover, the wavelengths at which the sidebands are created are very sensitive to these parameters: a 1% change in either of them shifts the SFWM sidebands by 30 nm. Thus, this method cannot satisfy all of our requirements to implement a factorable photon-pair state. Recently, however, this technique was implemented, with an appropriately selected fibre, to realize a factorable photon-pair source producing the signal at the visible wavelength while the idler at the telecom ($\sim 1550\,\mathrm{nm}$) [123]. Such a source is ideal for applications requiring the transmission of one photon over a long distance: the telecom photon can be transmitted using low loss telecommunications fibres, while the visible is detected efficiently with silicon based APDs.

3.3 Altering the phase-matching conditions

The difficulty of implementing an experimentally useful (high detection efficiency) uncorrelated photon-pair source using this scheme requires the consideration of a different technique that manipulates the phase-matching condition in Eqs. (2.35). In the following, we consider several possible ways to alter this condition and the solutions of the equation.

3.3.1 Phase modulation

So far our argument and considerations of the phase-matching curves did not take into account SPM and XPM. Both effects manipulate the phase of the involved

fields, and the phase-matching condition is altered accordingly. The intensity of the sidebands is so low (only just above zero average photon-number) that they cannot affect the phase of themselves or other fields. The strong pump, on the other hand, can experience SPM as well as induce XPM on the sidebands. The XPM interaction is twice as strong as the SPM[112], and the phase-matching condition which takes into account these effects has an additional nonlinear (power dependent) term:

$$2k(\omega_p^0) - k(\omega_s^0) - k(\omega_i^0) - 2\gamma P_0 = 0 \,, \tag{3.15}$$

where P_0 is the pump peak power, γ is the nonlinear parameter defined as

$$\gamma = \frac{3\omega_p \chi^{(3)}}{8ncA_{eff}} \,, \tag{3.16}$$

n is the linear index of the pump, $\chi^{(3)}$ is the relevant FWM susceptibility, A_{eff} is the effective mode area which is assumed to be the same for all of the interacting fields and defined as

$$A_{eff} = \frac{\left(\iint I(x,y)\,dx\,dy\right)^2}{\iint I^2(x,y)\,dx\,dy} \,, \tag{3.17}$$

$I(x,y)$ is the spatial field intensity profile and the integration is over the cross-section. The nonlinear term in Eq. (3.15) gives us a power dependent control over the phase-matching. For low enough power, the aforementioned term is negligible and the phase-modulation can be ignored.

Typical values of the nonlinear parameter of highly nonlinear commercial fibres

are about $\gamma = 100\,[\text{W km}]^{-1}$.

3.3.2 Polarization modulation instability

Up to this point we have assumed that all of the interacting fields are propagating in the same mode and differ only in wavelength. However, if the relevant fields differ in their modes, the typical form of the phase-matching curve (as in Figure (3.4)) is no longer valid. Since only single-mode fibres can strictly guarantee the absence of spatial correlations between the signal and idler, we're determined to raise and use a scheme to generate uncorrelated photon-pairs in such fibres. We therefore concentrate and employ the polarization degree of freedom to introduce the different propagating modes (as opposed to the spatial degree of freedom).

In circularly symmetric fibres, the dispersion does not depend on the polarization, and no manipulation to the phase-matching curve is applied by polarization considerations. Birefringent fibres are manufactured with this symmetry broken, realizing a polarization dependent dispersion.

The nonlinear interaction is mediated by the fused-silica material of which the core is made. Let's denote by $\chi^{(3)}_{ijkl}$ the nonlinear susceptibility of the medium, where i, j, k, l are either x or y, indicating two orthogonal directions. In isotropic materials and non-resonant electronic interaction, which is the case of pure silica, the susceptibility satisfies[95]

$$\chi^{(3)}_{xxyy} = \chi^{(3)}_{xyxy} = \chi^{(3)}_{xyyx} = \chi^{(3)}_{yyxx} = \chi^{(3)}_{yxyx} = \chi^{(3)}_{yxxy} = \frac{1}{3}\chi^{(3)}_{xxxx} = \frac{1}{3}\chi^{(3)}_{yyyy}\,. \tag{3.18}$$

All of the other terms vanish due to symmetry.

There are two pump configurations that can be considered in respect to the polarization: in the first, the pump is aligned with one of the principal axes of the birefringent fibre, and in the second configuration the pump is rotated by 45^o with respect to those axes, realizing two orthogonally polarized pumps with degenerate spectra. Suppose the pump is aligned with one of those axes, call it x. The sidebands then can be created co-polarized with the pump via the $\chi^{(3)}_{xxxx}$ nonlinear susceptibility, a SFWM process called *scalar modulation instability* (SMI), or, they can be created orthogonally polarized to the pump with the interaction mediated by $\chi^{(3)}_{yyxx}$, $\chi^{(3)}_{yxyx}$ and $\chi^{(3)}_{yyxy}$. This type of SFWM is referred to as *polarization modulation instability* (PMI)[124]. Since the nonlinear susceptibility responsible for PMI is 3 times smaller than the one for SMI, the total production rate is typically suppressed by a factor of 9 (the photon-pair amplitude is proportional to the susceptibility while the probability is the amplitude squared). In addition, the XPM that the sidebands experience in the PMI setup is also suppressed by a factor of 3. Thus, the phase-matching contour equation in PMI is given by[111]:

$$2k_x(\omega_p^0) - k_y(\omega_s^0) - k_y(\omega_i^0) + \frac{2}{3}\gamma P_0 = 0 \ , \tag{3.19}$$

where k_x and k_y are the wave-vectors of the x and y polarized fields. The fibre birefringence, typically frequency dependent, is defined as:

$$\Delta n(\omega) = (k_x(\omega) - k_y(\omega))\frac{c}{\omega} \ . \tag{3.20}$$

With this definition, Eq. (3.19) may be rewritten as

$$2k(\omega_p^0) - k(\omega_s^0) - k(\omega_i^0) + 2\Delta n(\omega_p^0)\frac{\omega_p^0}{c} + \frac{2}{3}\gamma P_0 = 0 \,, \tag{3.21}$$

where $k(\omega) = k_y(\omega)$ is the wave-vector of the polarization along the sidebands axis.

The principal axes of birefringent fibres are referred to as the *slow axis* and *fast axis* – the former has a higher effective index than the latter. Thus, $\Delta n(\omega_p^0) > 0$ means the pump is launched to propagate along the slow axis, while $\Delta n(\omega_p^0) < 0$ means that it is coupled into the fast axis.

3.3.3 Effective index-difference

Let's define an effective index-difference as:

$$\Delta n_{eff}(\omega) = \begin{cases} -\frac{\gamma P_0 c}{\omega}, & \text{for SMI} \\ \Delta n(\omega) + \frac{\gamma P_0 c}{3\omega}, & \text{for PMI} \end{cases} \tag{3.22}$$

Using this definition, which treats the nonlinear term as an effective induced index, we can rewrite Eqs. (3.15) and (3.21) in an equivalent form as:

$$2k(\omega_p^0) - k(\omega_s^0) - k(\omega_i^0) + 2\Delta n_{eff}(\omega_p)\frac{\omega_p^0}{c} = 0 \,. \tag{3.23}$$

Note that the power dependency in Δn_{eff} always contributes a negative term in SMI or positive in PMI, while the birefringence can be either positive or negative – allowing more flexibility.

In order to understand how Δn_{eff} affects the phase-matching solutions, we look at the manipulated equation Eq. (2.51) given by the Taylor expansion of the wave-vector about the pump frequency:

$$-2\sum_{n=1}^{\infty}\frac{1}{(2n)!}\beta_{2n}\Omega_{si}^{2n}+2\Delta n_{eff}(\omega_p^0)\frac{\omega_p^0}{c}=0\ . \tag{3.24}$$

When the pump is far from the ZGVD wavelength, the main contribution comes from the lowest order – the β_2 term, thus

$$\Omega_{si}\approx\sqrt{\frac{2\Delta n_{eff}\omega_p^0}{\beta_2 c}}\ . \tag{3.25}$$

Hence, while for $\Delta n_{eff}=0$ there are no phase-matching solutions (apart from the zero detuning), nonzero effective index-difference gives rise to new solutions at pump wavelengths where the β_2 and Δn_{eff} bear the same sign. The detuning of the sidebands from the pump is proportional to the square-root of the effective index-difference. Note that for pump close to the ZGVD wavelength ($\beta_2\to 0$), higher order terms are significant and need to be taken into account.

Figure 3.5 shows the phase-matching contour for the fibre depicted in Figure 3.4 with various values of Δn_{eff}. As expected, $\Delta n_{eff}\neq 0$ creates new phase-matched solutions with sidebands which are relatively close to the pump and their detuning increases with the value of Δn_{eff}. These new solutions emerge either between the two ZGVD wavelengths or outside this region – depending on the sign of Δn_{eff}, in accordance with Eq. (3.25). Most importantly for us – there are points where GV

matching occurs in the new solutions!

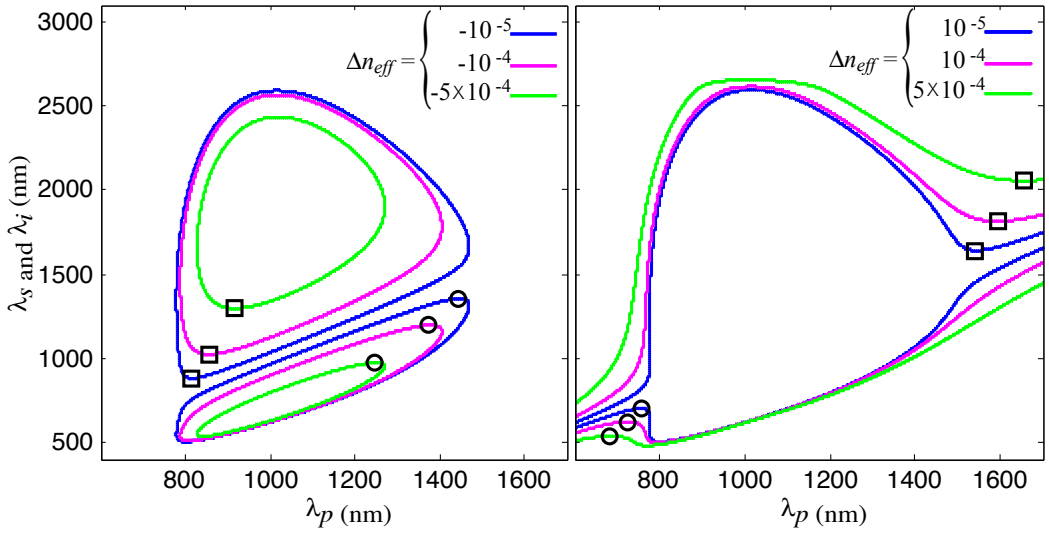


Figure 3.5 The phase-matching contours for various negative (left) and positive (right) values of Δn_{eff}, with the fibre parameters depicted in Figure 3.4. Points where additional GV-matching occurs (thanks to nonzero Δn_{eff}) are marked: Circles – the signal gain curve is flat and idler-pump GV-matching occurs. Rectangles – the idler gain is flat indicating GV-matching between signal and pump.

We see then that the greater the magnitude of Δn_{eff} the farther the sidebands are detuned from the pump. Therefore we require it to be big enough to create an idler photon beyond the Raman gain, but small enough in order to keep the sidebands within the detection bandwidth. Typical pump powers used for SFWM in PCFs[82,86,88–90,125–127], including this thesis, give a nonlinear contribution to Δn_{eff} up to the order of 10^{-6}. This contribution is too small to rely on to create enough detuning from the pump, and low pump power is essential to keep the nonlinear processes in the spontaneous regime. Moreover, the derivation of the nonlinear term in the phase-matching function, which is commonly used in the literature, actually

assumes a monochromatic pump and is just generalized for the pulsed case[112]. Hence, it does not take into account correctly the time dependency of SPM and XPM due to the temporal variation of the pump envelope as well as the walk-off between the sidebands and the pump. Even if we used an accurate model that incorporates these effects, we would need to maintain low power fluctuations to ensure reliability of a scheme employing the nonlinear term, which is experimentally challenging.

Due to the above argument, we opt to use low enough pump power to keep the phase modulation term negligible, and employ birefringence as our resource for the effective index difference.

3.3.4 Cross phase modulation instability

When the pump is launched into *both* the x and y axes of the fibre, the SFWM which utilizes this configuration, known as *cross phase modulation instability* (XPMI), creates orthogonally polarized sidebands[125]. The phase-matching equation for this case is (neglecting the power dependent contribution)

$$k_x(\omega_p^0) + k_y(\omega_p^0) - k_x(\omega_s^0) - k_y(\omega_i^0) = 0 \,, \tag{3.26}$$

where we define the the signal as polarized along the x-axis and the idler along the y-axis. Using the definition of the birefringence in Eq. (3.20) and assuming

$\Delta n(\omega_i^0) \cong \Delta n(\omega_p^0) = \Delta n$, this phase-mismatch is written as:

$$2k(\omega_p^0) - k(\omega_s^0) - k(\omega_i^0) + \Delta n \frac{\omega_p^0 - \omega_i^0}{c} = 0 \, . \tag{3.27}$$

The contribution of the birefringence term, proportional to the detuning $\omega_s^0 - \omega_p^0$, is typically a lot smaller than the one in Eq. (3.21) as the latter is proportional to $2\omega_p^0$. Therefore, XPMI creates sidebands with smaller detuning with respect to PMI. In terms of generation efficiency, the XPMI with a given total pump power is the same as in PMI[116]. One problem that can arise by pumping with two polarizatoins is a temporal walk-off between the pumps: their group velocities differ by $\Delta n/c$. Typical birefringence is $\Delta n = 3 \times 10^{-4}$, and with a typical fibre length of $L = 1\,\mathrm{m}$, the temporal delay between the two pumps reaches 1 ps. Thus, if the pump duration is on this order, the temporal walk-off needs to be taken into account within the calculations of the joint spectral amplitude, and Eqs. (2.44) are no longer valid. Moreover, if the duration of the pump pulses is less than the temporal walk-off, the SFWM interaction between the orthogonal components ceases when there is no overlap between the two pulses – before they exploit the whole fibre length.

This configuration, then, imposes complications with no apparent gain, and hence we opt to restrict ourselves to experimental implementation with a single pump.

3.4 Bandwidth and fibre length considerations

The condition for a factorable photon-pair state, according to Eq. (3.3), is given by:

$$L = \frac{1}{\sigma_p}\sqrt{\frac{2}{b\left(k'_p(\omega_p^0) - k'_s(\omega_s^0)\right)\left(k'_i(\omega_p^0) - k'_p(\omega_s^0)\right)}}\ , \tag{3.28}$$

i.e., the required fibre length is inversely proportional to the pump bandwidth. Seemingly, one is free to choose any set of L and σ_p satisfying the above condition. However, we need to remember that this relationship relies on the validity of Eqs. (2.44) as a good approximation to the joint spectral amplitude, which was derived assuming the fields involved in the SFWM experience negligible dispersion. All of these fields' bandwidths are of the order of σ_p or a lot narrower than that in the case of approaching the horizontal or vertical phase-matching function ($\theta_{si} \to 0^o$ or 90^o). Thus, we can treat σ_p as a typical bandwidth or at least upper bound. The requirement for Eqs. (2.44) to hold is then:

$$k''_\mu(\omega_\mu^0)L\sigma_p^2 = \zeta << 1\ , \tag{3.29}$$

for $\mu = s, i, p$. As ζ becomes smaller the purity reaches asymptotically the one implied by the joint spectral amplitude in Eqs. (2.44). Since ζ is quadratic with σ_p, narrowing the pump bandwidth and extending the fibre length by the same factor, such that Eq. (3.28) is maintained, decreases the value of ζ and improves the approximation.

In the horizontal phase-matching function case ($\theta_{si} = 0^o$), in addition to $\zeta << 1$ we also require $\sigma_{si}/\sigma_p \to 0$ so the purity reaches unity. That means:

$$\left[L\sigma_p|k_p'(\omega_p^0) - k_i'(\omega_i^0)|\right]^{-1} = \xi << 1 \; . \tag{3.30}$$

We can therefore always narrow the bandwidth followed by an appropriate extension of the fibre length such that both ζ (improve the approximation) and ξ (enhance the purity) decrease. Note that greater GV mismatch between the pump and idler can also increase the purity. The above argument is obviously also valid in the $\theta_{si} = 90^o$ case, with signal and idler interchanged.

To conclude, the theoretical calculations show that the longer the fibre the purer the state of the created photons, provided that the pump bandwidth is chosen appropriately.

Chapter 4

Characterizing fibres

In Chapter 3 we have shown a model for PCFs from which we learned that GV-matching conditions can be satisfied by pumping a birefringent fibre close to its ZGVD wavelength. In this chapter we characterize PCFs in order to identify an experimentally suitable fibre for the generation of factorable photon-pair state.

4.1 Searching for a suitable fibre

Typical PCFs normally exhibit significant "natural" birefringence due to asymmetries in the holes pattern or stresses in the glass. These asymmetries raise a typical residual birefringence of[102,106,111] $10^{-5} - 10^{-4}$. A deliberate birefringence can be added by defecting the pattern or manufacturing the PCF with an asymmetric core. This intentional birefringence is typically $10^{-4} - 10^{-3}$.

Based on the calculations made with the fibre parameters depicted in Figure 3.5, we expect a birefringence greater than 10^{-4} to produce idler photons shifted

from the pump by at least 140 nm at GV-matching point, which is very beneficial to avoid Raman background. However, the typical birefringence of birefringent PCFs is even larger, and when pumping at wavelengths longer than 770 nm (the shortest wavelength to which our laser system can be tuned) the idler is beyond the detection bandwidth of our detectors. Therefore, we had to opt for lower birefringence and hence rely on the residual one. Unfortunately, the magnitude of this birefringence is not specified by the manufacturer of the commercially available PCFs, and though the fibre model helps in choosing good candidates and ruling out others, only measurements and experimental investigation could provide definite information about the ability of a specific fibre to generate a factorable photon-pair state.

Table 4.1 The PCFs for which phase-matching measurements were taken with their specifications as given by Crystal-Fibre. SM = single-mode. The fibre NL-PM-750 is a (deliberately) birefringent (polarization maintaining) PCF.

Fibre name	Core Diameter (μm)	short λ_{ZGVD} (nm)	long λ_{ZGVD} (nm)	SM cut-off wavelength (nm)	γ@780 nm $(\mathrm{W\,km})^{-1}$
NL-2.3-790	2.3	790	—	—	80
NL-1.7-785	1.7	785	—	675	106
NL-1.8-730	1.8	730	1585	1085	100
NL-1.8-750	1.8	750	1250	600	102
NL-PM-750	1.8	750	1250	690	102

We purchased various PCFs from Crystal-Fibre, all have ZGVD wavelengths at around 780 nm. These fibres and provided specifications are listed in Table 4.1. We set out to measure the central wavelengths of the sidebands generated by these fibres as a function of the central pump wavelength. A schematic of the experimental setup is illustrated in Figure 4.1: the bandwidth of our mode-locked 76 MHz rep-

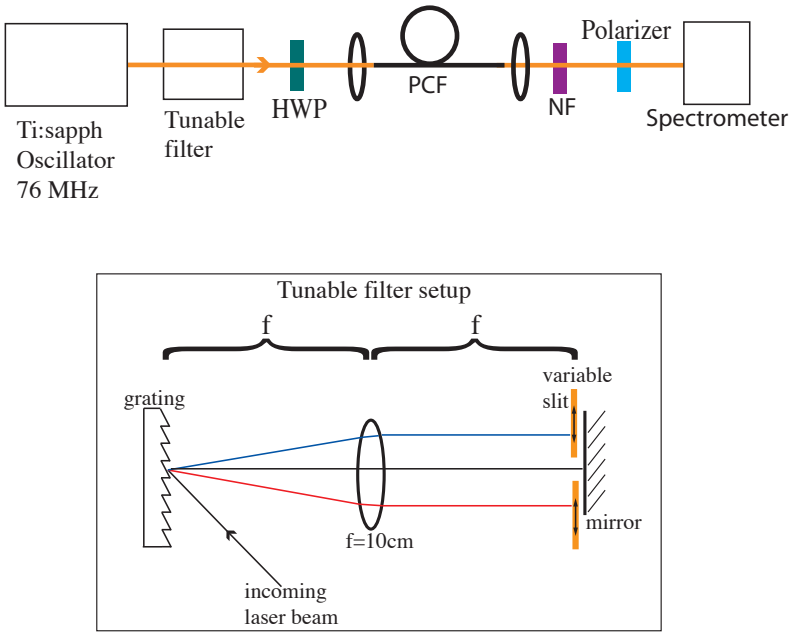


Figure 4.1 The setup used to observe and measure the sideband wavelengths as the pump wavelength is scanned. Top: the output of the oscillator is filtered by a tunable filter to a bandwidth of about 4 nm. Its linear polarization is aligned, using a half-wave plate (HWP), with one of the principal axes of a PCF sample, focused and coupled into the fibre. At the output the beam is collimated, the pump is rejected by a notch-filter (NF) and a polarizer is used to select the polarization analyzed by the spectrometer. Bottom box: a top view of the tunable filter setup, composed of a folded 4f imaging line and a grating. The tunable slit selects the wavelength and bandwidth. The mirror is slightly tilted, reflecting the (filtered) beam downwards which is then picked with a lower mirror (not shown).

etition rate and 50 fs pulse coherent length Titanium:Sapphire laser is filtered by a tunable grating-based filter that is used to tune the pump wavelength and bandwidth. The pump polarization is rotated by a half-wave plate (HWP) to align it with the principal axes of the PCF. A microscope objective focuses the light to couple it into the PCF, and an identical objective collimates the output. A notch-filter (Semrock NF01-785U-25, 39 nm FWHM blocking bandwidth at 785 nm) eliminates the pump light. A polarizer selects the polarization to be analyzed by a spectrometer –

either parallel to the pump (SMI) or orthogonal (PMI). We used a home-built highly efficient spectrometer covering the bandwidth $600-1000\,\text{nm}$. The pump bandwidth is set to $3-4\,\text{nm}$, the narrowest which allows enough pump power, about 1 mW, to produce observable sidebands gain. The scanning range was bounded at the short wavelengths by the tunability of the laser and by the notch-filter bandwidth at the long wavelengths. An example of the nonlinear spectral gain is shown in Figure 4.2.

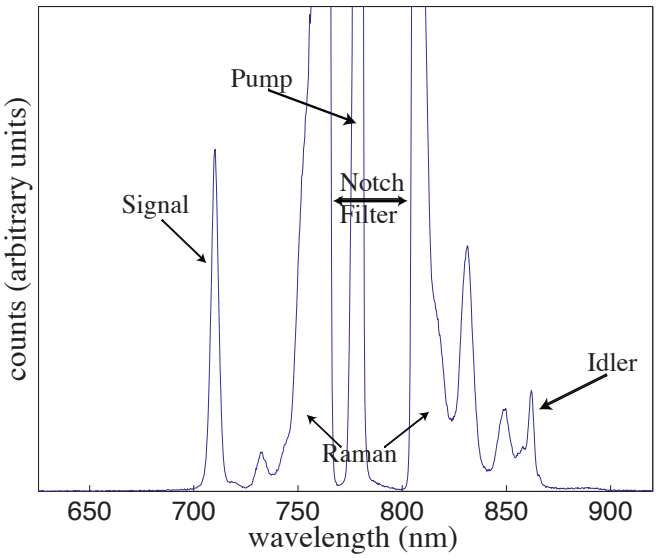


Figure 4.2 The spectral gain in 40 cm of the NL-1.8-750 PCF (taken with the Andor Spectograph), pumping at 778.5 nm with bandwidth of 4 nm and typical power of 1 mW. The signal appears at 710 nm and the idler at 861.5 nm

The phase-matching measurements are plotted in Figure 4.3. $ff \rightarrow ff$ and $ff \rightarrow ss$ indicate that two photons of the pump aligned on the fast axis are scattered to generate sidebands polarized along the fast and slow axes, respectively. $ss \rightarrow ff$ and $ss \rightarrow ss$ indicate the same with pump polarized along the slow axis. Due to Raman background and imperfection of the spectrometer alignment, the idler

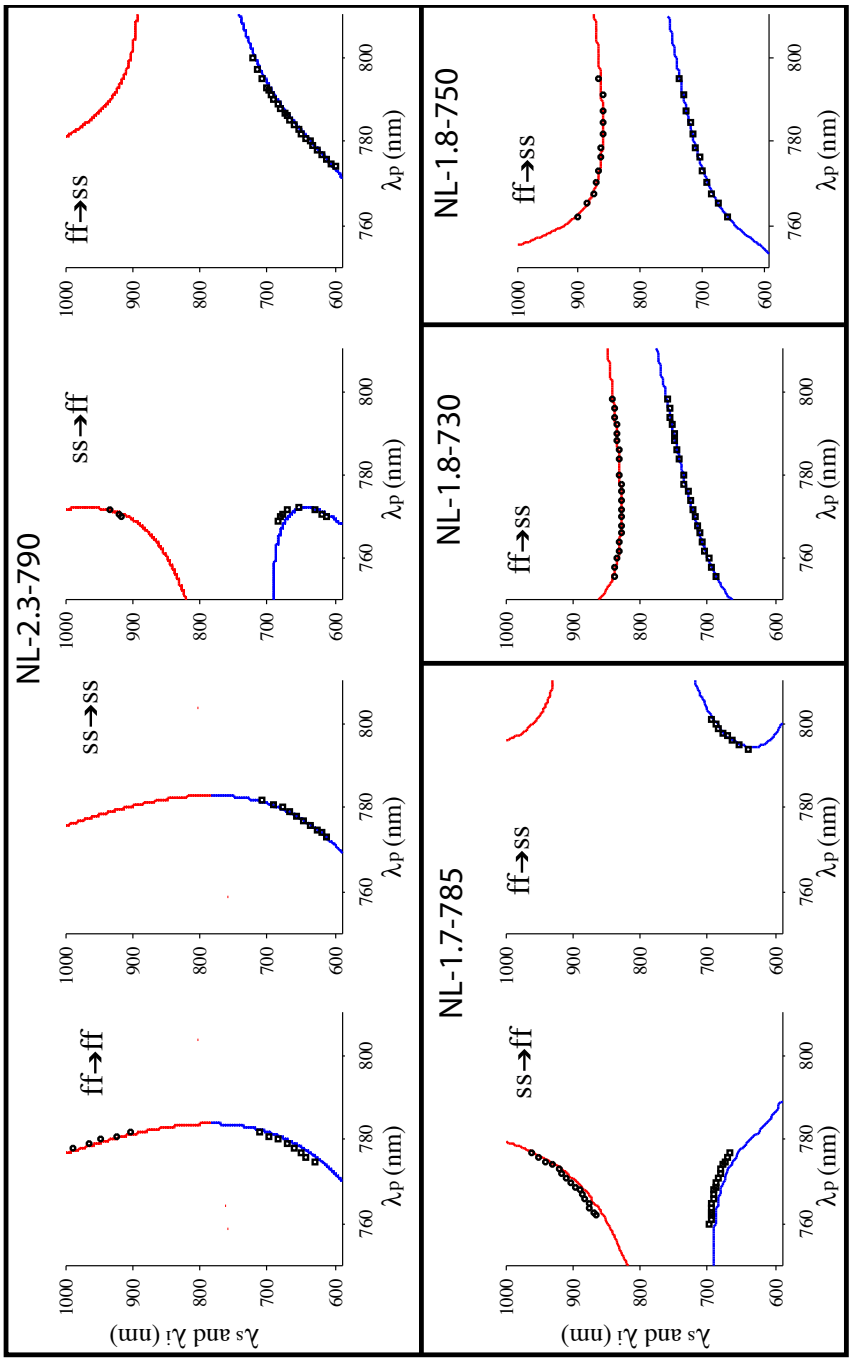


Figure 4.3 Phase-matching contours for the tested PCFs. Rectangles (signal) and circles (idler) present experimental data. The solid curves show the theoretical fits.

photons were not always identified on the spectrometer. However, using the observed signal and measured pump wavelengths, we calculate the idler wavelength, providing all the information required for identifying a GV-matching point. We later purchased an Andor Spectograph (SR-163) with attached CCD camera (IDus DV420A-0E) with which the spectrum in Figure 4.2 and data presented for the fibre NL-1.8-750 were taken.

For each fibre we examined all polarization possibilities, i.e., we looked for sidebands generated both in SMI and PMI for each pump polarization. The presented plots are only for those processes in which sidebands could be observed, i.e., phase-matching occurred within the detection bandwidth. No SFWM was observed in the fibre NL-PM-750 within the pumping wavelength range, this is due to the fact that the pump is too far from the ZGVD wavelength for SMI phase-matching, and the birefringence is too big ($\Delta n > 3 \times 10^{-4}$) for the PMI to produce sidebands in the detection range.

The plots also show theoretical fits (top red curve corresponds to idler wavelengths and bottom blue to signal wavelengths), using a birefringent variation of the step-index model[102,111] to calculate the theoretical dispersion in birefringent fibres. In this model, each principal axis is modeled independently. Thus, d_{fast} and d_{slow} are the core diameter parameters for the fast and slow axes respectively, and their associated air filling fraction parameters are r_{fast} and r_{slow}. The fitting parameters are listed in Table 4.2.

As can be seen, NL-1.8-730 and NL-1.8-750 exhibit GV-matching within the

Table 4.2 Fitted fibre parameters for to the data shown in Figure 4.3. d_{spec} is the core diameter as specified by the manufacturer. Δn is the birefringence (at 785 nm) implied by the fibre parameters.

Fibre name	d_{spec} (μm)	d_{fast} (μm)	d_{slow} (μm)	r_{fast} (%)	r_{slow} (%)	Δn ($\times 10^{-5}$)
NL-2.3-790	2.3	2.2766	2.2797	66.78	67.64	1.7
NL-1.7-785	1.7	1.5906	1.5910	42.57	42.74	1.5
NL-1.8-730	1.8	1.7268	1.7277	53.78	53.95	0.9
NL-1.8-750	1.8	1.7488	1.7507	50.50	51.10	1.4

pump scanning bandwidth. For both fibres this matching occurs between the signal and pump. In the former phase-matching contour, the idler measurements show a minimum at $\lambda_p \approx 775\,\text{nm}$, and in the latter this occurs at $\lambda_p \approx 785\,\text{nm}$. Since the pump is at an anomalous dispersion wavelength ($D(\lambda_p) > 0$), we deduce that the idler lags after it.

When both signal and idler can be identified in the spectral measurements, we estimate the error in their central wavelength by finding the discrepancy between the measured data and energy conservation: the latter requires

$$\frac{2}{\lambda_p} = \frac{1}{\lambda_s} + \frac{1}{\lambda_i}\,, \tag{4.1}$$

where λ_p, λ_s and λ_i are the (free space) central wavelengths of the pump, signal and idler, respectively. Due to experimental errors, the measured data does not necessarily agree with this theoretical prediction, and we can estimate the error on the measured signal ($\Delta\lambda_s$) and idler ($\Delta\lambda_i$) wavelengths as the discrepancy with

energy conservation:

$$\Delta\lambda_s = \left| \left(\frac{2}{\lambda_p} - \frac{1}{\lambda_i} \right)^{-1} - \lambda_s \right| \quad , \quad \Delta\lambda_i = \left| \left(\frac{2}{\lambda_p} - \frac{1}{\lambda_s} \right)^{-1} - \lambda_i \right| . \tag{4.2}$$

These errors are typically less than 3 nm for the measurements taken with the home-built spectrometer, and less than 1 nm with the Andor Spectograph.

4.2 Selected fibre: characteristics and model

Out of the two PCFs with observed GV-matching points, we chose to generate the photons and test their purity with the fibre NL-1.8-750, as both our laser and some optical parts perform better at the wavelength 785 nm than 775 nm. A detailed plot of the phase-matching curve of this fibre is presented in Figure 4.4.

We calculate the joint spectral amplitude $f(\omega_s, \omega_i)$ by solving numerically Eq. (2.38) with (2.30) using the model dispersion. We assume a 50 fs pump pulse with central wavelength $\lambda_p = 783$ nm – the wavelength at which, according to the model, GV-matching occurs. The pump spectrum is taken as sharply cut to within a (zero to zero spectrum) bandwidth $\Delta\lambda_p = 8$ nm. The sharp cut, which simulates the tunable filter we used, is expressed mathematically by setting the integration range to $[2\pi c/(\lambda_p + \Delta\lambda_p/2), 2\pi c/(\lambda_p - \Delta\lambda_p/2)]$ in Eq. (2.38), where c is the speed of light in vacuum. The resulting joint spectral probability $|f(\omega_s, \omega_i)|^2$ is plotted in Figure 4.5. Using Eq. (1.10), we evaluate the theoretical purity of the heralded photons as $p = 86\%$.

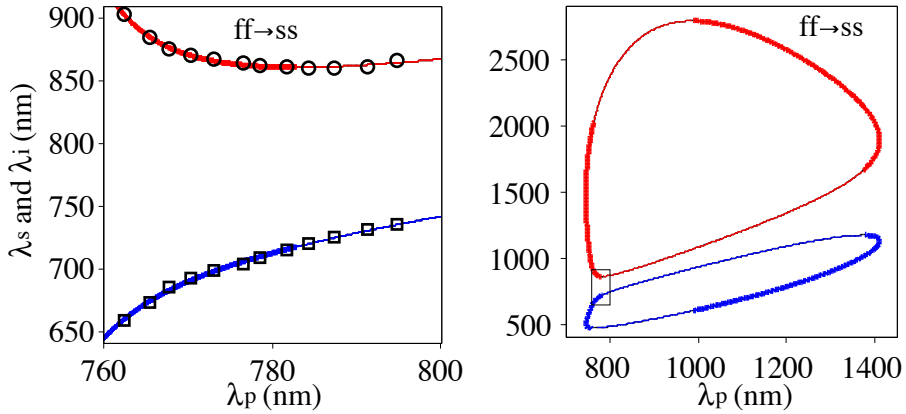


Figure 4.4 Phase-matching curve for the fibre **NL-1.8-750**. Left: measured signal (rectangles) and idler (circles) central wavelengths. The discrepancy between the measured data and energy conservation is less than 1 nm. Blue bottom (red top) curve is a plot of the fitted signal (idler) wavelength according to the fibre model. Right: A wide view of the phase-matching contour according to the model (the rectangle indicates the zoomed area in left figure). Thin lines indicate sections where factorability is possible, particularly, the join of thick and thin lines indicate GV-matching.

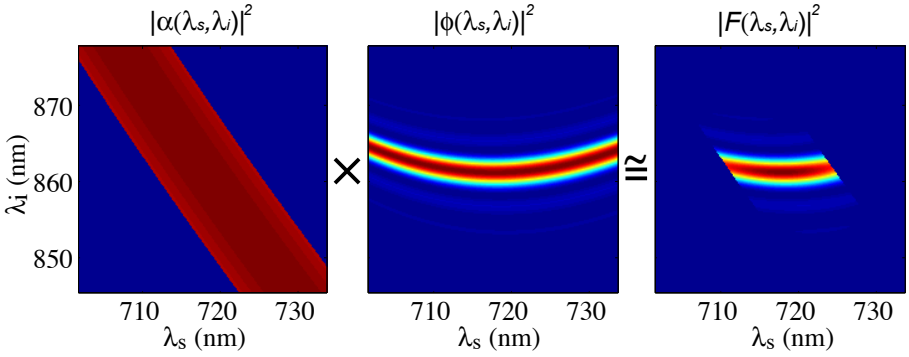


Figure 4.5 Calculated pump envelope (left), phase-matching function (middle) and the joint spectral probability (right) for our modeled fibre NL-1.8-750. The pump wavelength is set to 783 nm with sharply cut edges bandwidth of 8 nm. The associated purity is $p = 86\%$.

Chapter 5

Experimental purity demonstration

In the previous chapter we have identified a PCF with dispersion characteristics appropriate for our scheme to generate uncorrelated photon-pairs. This chapter presents the experimental measurement of the heralded photon's purity.

The most significant outcomes of this work are published in Reference [126]. Similar results were obtained by Halder *et al.* [127] independently.

5.1 The HOM interferometer setup

In Chapter 1 we introduced the HOM interference and explained how two pure indistinguishable photons bunch when mixed on a beamsplitter. In practice, however, two photons are not perfectly identical or pure, and the HOM experiment is a good

means to quantify the degree to which they are. Suppose that one photon is in the pure state $|\psi_1\rangle$ and the other in $|\phi_1\rangle$. The similarity between the photons is given by the state overlap, or the probability to find them in the same state, given by $p_1 = |\langle\psi_1|\phi_1\rangle|^2$. The probability that they are totally distinguishable is given by $(1-p_1)$. If the photons are perfectly identical, then they bunch, and no coincidence detection can occur at the output ports of the beamsplitter. If, on the other hand, their wave-packets are orthogonal, then they leave the beamsplitter at either the same or different arms, with 50% for each option. We conclude then, that the probability to find the photons at different ports after the interference, given they are in the above states, is $(1-p_1)/2$.

In general, the photons are in mixed states: there is a probability q_n of finding the first photon in the state $|\psi_n\rangle$ and probability r_m to find the second in the state $|\phi_m\rangle$, $\{|\psi_n\rangle\}$ and $\{|\phi_m\rangle\}$ are two orthogonal sets of states. Their density matrices are given by:

$$\begin{aligned} \rho_1 &= \textstyle\sum_n q_n |\psi_n\rangle\langle\psi_n| \,, \\ \rho_2 &= \textstyle\sum_m r_m |\phi_m\rangle\langle\phi_m| \,. \end{aligned} \tag{5.1}$$

Thus, the probability of finding the two photons in the specific states $|\psi_n\rangle$ and $|\phi_m\rangle$ is $q_n \times r_n$, and once they are found in these particular states, the overlap between them is $|\langle\psi_n|\phi_m\rangle|^2$. Summing over all possibilities, the probability that the two

photons are indistinguishable is:

$$\begin{aligned} p &= \sum_{nm} q_n r_m |\langle\psi_n|\phi_m\rangle|^2 \\ &= \sum_{nm} q_n r_m \langle\psi_n|\phi_m\rangle\langle\phi_m|\psi_n\rangle \\ &= \sum_{nml} q_n r_m \langle\psi_n|\phi_m\rangle\langle\phi_m|\psi_l\rangle\langle\psi_l|\psi_n\rangle \\ &= \sum_l \langle\psi_l| \left(\sum_n q_n |\psi_n\rangle\langle\psi_n|\right) \left(\sum_m r_m |\phi_m\rangle\langle\phi_m|\right) |\psi_l\rangle \\ &= Tr\left(\rho_1 \rho_2\right) \ , \end{aligned} \tag{5.2}$$

where in the third line we make use of the completeness of the $\{|\psi_l\rangle\}$ basis. Throughout this thesis, unless stated differently, we assume $\rho_1 = \rho_2$, i.e., the two photons are identical (but not necessarily pure). In this case, p is said to be the *purity* of the photons. The probability of finding the two photons on different output ports of the HOM interferometer is generalized to $(1-p)/2$.

5.1.1 Typical HOM setup

Before we describe the setup used in our experiment, let's examine a typical form of the HOM setup, a schematic of which is illustrated in Figure 5.1 (a). Two photons (normally from identical sources) are interfered on a 50% beamsplitter. A coincidence detection implies something about the impurity of the photons. In order to get statistically meaningful results, the experiment is repeated many times, N_{exp}. The number of coincidences N_{coin} is recorded. Hence, the probability for coincidence detection is N_{coin}/N_{exp}, and the purity can be deduced as $p = 1 - 2(N_{coin}/N_{exp})$. This, however, is correct only if the purity is the only source for the lack of coin-

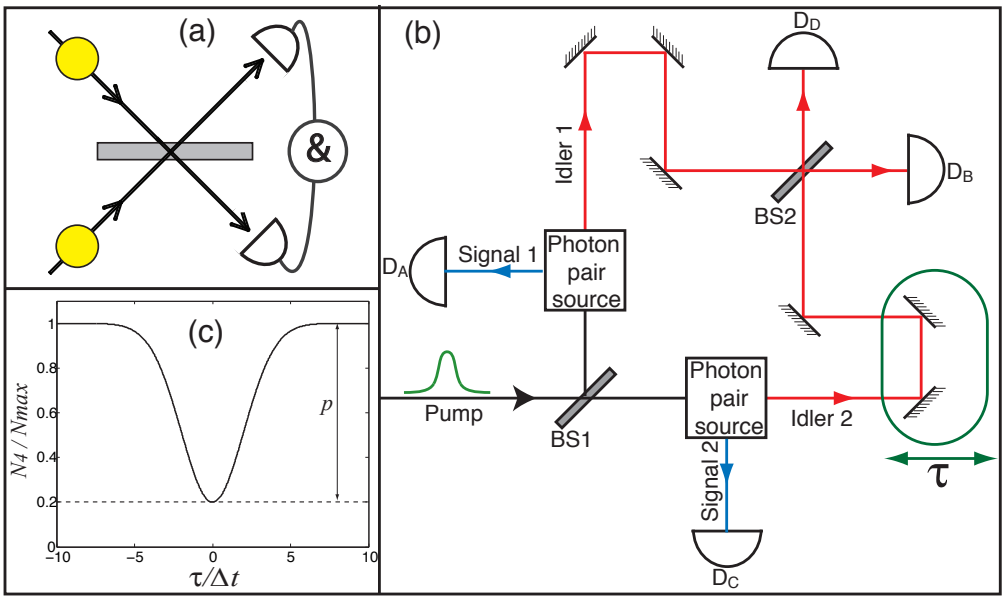


Figure 5.1 A typical setup for a HOM interferometer. (a) The general idea: two photons interfered on a 50% beamsplitter, and coincidence events are noted. (b) A typical HOM setup with SPDC or SFWM photon-pair sources. The pump pulse is split into two on a beamsplitter (BS1) to pump two identical sources. Coincidence detections at D_A and D_C herald the existence of two spatially separated idler photons. One of them (Idler 2) experiences a variable time delay. Then both heralded photons interfere on BS2, followed by coincidence detection at D_B and D_D. The four-fold coincidence events $N_4(\tau)$ are counted for given number of pump pulses N_{trials} and a time delay τ. (c) An example (with $p = 80\%$) plot of the four-fold coincidence as a function of τ. The width of the interference curve is given by the idler coherence length Δt. The visibility is the purity of the photons.

cidence detections. In practice, unsuccessful preparation of a single photon, losses occurring before and after the interference, and the poor efficiency of the single photon detectors, all contribute to the lack of coincidences even if the interfered photons are totally distinguishable. It is therefore unreliable to infer the purity just from the above statistics, and one needs to account for the aforementioned setup imperfections. A common HOM setup [89,93,127] with SPDC or SFWM is illustrated

in Figure 5.1 (b). Two (nominally identical) sources are pumped by a train of pulses to generate probabilistically photon-pairs. Each pump pulse is considered as a single trial, and N_{trials} pump pulses are used to form an experimental ensemble. The Hamiltonian describing the process in which two sources are pumped is given by

$$H(t) = H_1(t) + H_2(t) \,, \tag{5.3}$$

where H_1 and H_2 are of the form of Eq. (2.29) with corresponding field operators $a_{1\mu}$ and $a_{2\mu}$ ($\mu = s$ or i for signal and idler, respectively) associated with the modes created by the two different sources. In general, the two Hamiltonians may also differ in the pump envelope $\mathcal{E}_p(\omega) \rightarrow \mathcal{E}_{1p}(\omega)$ and $\mathcal{E}_{2p}(\omega)$ in H_1 and H_2, but here we assume a pump equally split between the sources. The scattering operator is evaluated as:

$$\mathbb{S} = \mathcal{T} \exp\left[\int_{-\infty}^{+\infty} (H_1(t) + H_2(t))\, dt\right] \,. \tag{5.4}$$

Assuming a vacuum input state, the emerging state from the nonlinear interaction is $|\psi\rangle = \mathbb{S}|0\rangle$. The lowest order non-vacuum outcome is then

$$|\psi\rangle = \iint d\omega_s d\omega_i f(\omega_s, \omega_i) \frac{1}{\sqrt{2}} \left(a_{1s}^\dagger a_{1i}^\dagger + a_{2s}^\dagger a_{2i}^\dagger\right) |0\rangle \,. \tag{5.5}$$

Thus, to the first order, pumping two separated sources creates a photon-pair in a rail-entangled state. However, for the purpose of HOM-interference, we are interested in the generation of two pairs, i.e. the second order expansion. This is done by

post-selecting coincidence detection events of signal photons at the detectors D_A and D_C in Figure 5.1 (b), which herald the generation of two pairs at the two separated sources. The idler photons then interfere on a 50% beamsplitter, and detectors D_B and D_D count coincidences after the interference. The number of four-fold coincidences N_4 (i.e. all of the detectors fire coincidentally) for fixed N_{trials} is recorded. The indistinguishability between the interfered idler photons suppresses N_4, which is proportional to the probability $(1-p)/2$. In order to know by how much it is suppressed, while taking into account losses, distinguishing information between the idler photons is imposed, usually by means of time delay: the time at which one of the idler photons arrives at the beamsplitter is scanned by changing its path length. When the two photons are temporally separated, they are totally distinguishable and no bunching effect occurs. This leads to a maximal four-fold count N_{max}. In general, one records the four-fold coincidences $N_4(\tau)$ as a function of the imposed time delay τ, and compares it with the maximal coincidence $N_{max} = N_4(\tau \to \pm\infty)$. An example plot of N_4 as a function of τ is shown in Figure 5.1 (c).

In essence, the distinguishing information between the two interfered photons in the HOM setup can be introduced by other means than the time delay: e.g. polarization and spatial or spectral overlap. The main reason that the delay is the chosen parameter to vary in these experiments lies in the difficulty of temporally matching the two photons, thus scanning the delay achieves two goals at once: finding the zero delay and introducing distinguishability.

5.1.2 The setup

The setup we've just described requires two identical sources. Specifically to our case – two identical fibres. Unfortunately, manufacturers cannot guarantee the uniformity in PCFs, and we were concerned that two pieces of (even) the same fibre would differ in their dispersion properties to a degree high enough to impair the HOM interference. Indeed, Halder *et al.*[127] had to temperature control the fibre in order to match the phase-matching characteristics of two pieces. We opted to use one piece of fibre to implement the two sources. This is done by sending two pump beams into the fibre from the opposite ends, in a configuration called *Sagnac loop*. Like every HOM interference experiment, our setup – illustrated in Figure 5.2 – is comprised of pump preparation, photon-pairs generation, heralding arm and interference arm.

Pump

Our Titanium:Sapphire oscillator is generating 20 nm FWHM bandwidth at a repetition rate of 76 MHz. We centered its spectrum at $\lambda_p = 785$ nm. The laser beam is filtered down to a desirable bandwidth with the tunable filter. HWP1 rotates the pump polarization, setting the power transmitted through PBS1, thus constituting a power control. The reflection of PBS1 is blocked. HWP2 rotates the pump polarization.

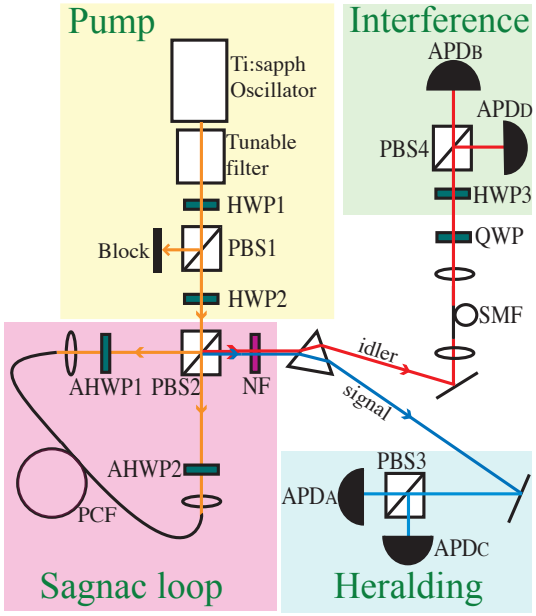


Figure 5.2 The polarization Hong-Ou-Mandel experimental setup. Pump power is controllably attenuated by HWP1 followed by PBS1. HWP2 rotates the polarization to split on PBS2. Achromatic half-wave plates (AHWP1 and AHWP2) align both pump beam polarizations with the fast axis of the PCF. PBS2 separates the sideband photons from the pump, sending the pump back towards the oscillator. A notch filter (NF) eliminates stray pump light. The signal and idler modes are separated using a prism. The signal arm is split on PBS3 and detected by APD_A and APD_C, while the idler photons are sent through a single-mode fiber (SMF). A quarter-wave plate (QWP) is used to restore the linearity of the polarization after SMF. HWP2 rotates the photons polarization to an angle θ, and then they interfere on PBS4. APD_B and APD_D counts events on the idler arm.

Sagnac loop

PBS2 splits the pump power to the clockwise and anti-clockwise direction (the power ratio is dictated by HWP2). Achromatic half-wave plates AHWP1 and AHWP2 align the clockwise and anti-clockwise pump polarization with the fast axis of the PCF. Achromatic lenses (microscope objectives $\times 40$) focus the pump beams into the fibre tips. Each of the counter-propagating pumps generate photon-pairs. The

pump beams emerge out of the fibre with the sidebands, are collimated by the achromatic lenses and pass through AHWP1 and AHWP2 that rotate their polarization. This rotation sets the polarization such that PBS2 sends both pump halves back towards the laser. In our case of PMI, since the signal-idler pairs are generated with polarization orthogonal to the pump, the photon-pairs are separated from the pump by PBS2 and sent to the free port. A notch-filter (NF) blocks stray pump light. The configuration implements two independent generations of photon-pairs: one is by the clockwise pump, generating pairs horizontally (H) polarized, while the anti-clockwise pump generates sidebands in the vertical (V) polarization. The signal and idler are separated spectrally using a prism which also ensures that only the bandwidth of the sidebands is coupled into our single-photon detectors (SPCM-AQ-4C). This rejects background contamination, especially Raman.

Heralding

Besides the fact that the Sagnac loop uses the same fibre for both sources, it has the advantage of inherently being robust to length-difference fluctuations between the two paths. Hence, no temporal delay exists between the two pairs, and ideally no spatial mismatch either. Thus, only the polarization distinguishes them. It is, therefore, convenient to use this configuration for the generation of polarization-entangled photons[87–89,91,117], which is the lowest order non-vacuum state coming out of the configuration. However, for the HOM interference, we herald the generation of both pumps having generated a photon-pair by detecting two orthogonally

polarized signal photons: PBS3 splits the two polarizations of the signal photons, which then coupled into multimode fibres connected to the detectors $\mathrm{APD_A}$ (H) and $\mathrm{APD_C}$ (V) to herald two orthogonally polarized idler photons.

Polarization HOM interference

The state of two (pure, but not necessarily identical) photons, orthogonally polarized, is generally

$$|\psi\rangle = a_H^\dagger b_V^\dagger |0\rangle \,, \tag{5.6}$$

where $a_q^\dagger$ and $b_q^\dagger$ are creation operators for horizontally ($q = H$) or vertically ($q = V$) polarized modes. Suppose we rotate the polarization of the state by 45^o. This rotation applies the transformation

$$\begin{aligned} a_H^\dagger &\to \tfrac{1}{\sqrt{2}} \left(a_H^\dagger + a_V^\dagger \right) \\ b_V^\dagger &\to \tfrac{1}{\sqrt{2}} \left(-b_H^\dagger + b_V^\dagger \right) \end{aligned} \tag{5.7}$$

and the resulting state is

$$\begin{aligned} |\tilde{\psi}\rangle &= \tfrac{1}{\sqrt{2}} \left(a_H^\dagger + a_V^\dagger \right) \tfrac{1}{\sqrt{2}} \left(-b_H^\dagger + b_V^\dagger \right) |0\rangle \\ &= \tfrac{1}{2} \left[\left(a_V^\dagger b_V^\dagger - a_H^\dagger b_H^\dagger \right) + \left(a_H^\dagger b_V^\dagger - b_H^\dagger a_V^\dagger \right) \right] |0\rangle \,. \end{aligned} \tag{5.8}$$

It follows then, that in the case where the two photons are indistinguishable, i.e. $a_q^\dagger = b_q^\dagger$, $|\tilde{\psi}\rangle = (1/2)({a_V^\dagger}^2 - {a_H^\dagger}^2)|0\rangle$ describes a state in which both photons are always found to have the same polarization. This rotation of the polarization is completely analogous to the interference on a beamsplitter, except here the spatial

modes are replaced with polarization modes.

Ideally, the two orthogonally polarized heralded photons produced by the Sagnac loop configuration are temporally and spatially overlapping, and a decrease in the polarization HOM interference effect is due to impurity, which is the very figure of merit we want to investigate here. In practice, however, it turns out that spatial mismatch between the orthogonal heralded photons does exist. We therefore couple the idler mode into a single-mode fibre (SMF) to ensure good overlap. The propagation in SMF manipulates and applies some (not *a priori* known) unitary transformation to the photons' polarization. A quarter-wave plate (QWP) partially restores the linearity of the polarization, leaving a residual ellipticity $\tan\eta$ – the ratio between the amplitudes of the principal axes of the elliptic polarization. HWP3 rotates to an angle θ the photons polarization. The photons interfere on PBS4 to implement a HOM-type interference. The two output arms of PBS4 are coupled into multimode fibres connected to $\mathrm{APD_B}$ and $\mathrm{APD_D}$.

The prism in the described setup disperses the beams spectrally. It is difficult to couple the correct wavelengths into the single- and multi-mode fibres of undetectable intensities. Fortunately, PCFs are highly nonlinear, and by increasing the pump power or bandwidth, the interaction generates light in a very broad spectrum, know as *white light generation*. We can therefore start the alignment with strong beams coming from the PCF to couple the correct wavelengths. It is in this high power regime that we could observe the spatial mismatch between the horizontal and vertical polarized beams generated by the nonlinear interaction in the fibre.

This mismatch exists despite the good overlap of the pump beams emerging out of the Sagnac loop. We therefore attribute this fault to chromatic aberrations of the microscope objectives, which are designed for the visible spectrum rather than the infra-red: the alignment is optimized for coupling the pump into the PCF by positioning the fibre tips at the objectives' focal plane. However, due to the chromatic aberrations, the fibre tips are displaced from the focal plane of the sideband wavelengths (which differ from the pump wavelength). This results in a spatial mismatch between the sideband photons emerging from *different* objectives.

Upon successful preparation of two orthogonal sideband pairs, the probability of a 4-fold coincidence detection (all four APDs fire), i.e., a coincidence of 2 signal heralding photon detections and two idler photons at the different output arms of PBS2, assuming no losses and 100% detection efficiency, is given by (see Appendix A):

$$P_4(\theta) = \frac{1}{2}\left[(1-p) + (1+p)\cos^2(2\eta)\cos^2(2\theta)\right], \tag{5.9}$$

where $p = Tr(\rho_V \rho_H)$ (the trace is taken over the spectral degree of freedom), ρ_H and ρ_V are the (spectral) density matrices of the heralded horizontal and vertical photons, respectively. In the case $\rho_H = \rho_V$, i.e. the photons are identical copies, p is the purity of the photons. Thus, from a fit to $P_4(\theta)$ we can find a lower bound on the purity. Figure 5.3 shows plots of $P_4(\theta)$ for $\eta = 0$ and various values of p.

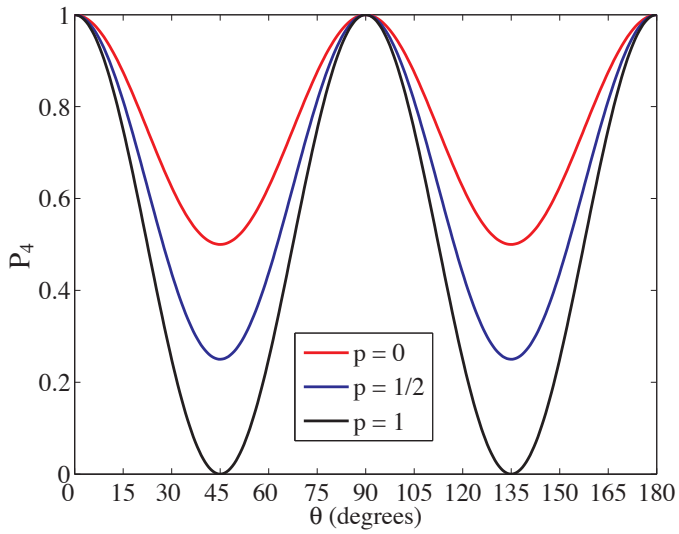


Figure 5.3 The 4-fold coincidence probability P_4 as a function of the rotational angle θ, assuming linearly polarized ($\eta = 0$) heralded (idler) photons, calculated for various values of p. Note that for $p = 1$, i.e. pure and identical interfered photons, this probability vanishes completely at $\theta = 45^o + m90^o$ for integer m (this is actually true also for $\eta \neq 0$).

5.2 Spectral characterization

We set the pump bandwidth to $\Delta\lambda_p = 8\,\text{nm}$ centered at $\lambda_p = 785\,\text{nm}$. The total power 1.4 mW is equally split between the counter-propagating paths in the Sagnac loop. The spectral output of this configuration is shown in Figure 5.4. The created signal and idler sidebands are centered at $\lambda_s = 720\,\text{nm}$ and $\lambda_i = 860\,\text{nm}$, respectively, with corresponding standard deviation bandwidths $\Delta\lambda_s = 3.4\,\text{nm}$ and $\Delta\lambda_i = 0.84\,\text{nm}$.

A spectral comparison between the generated photons along the counter propagating directions is also presented: we set the pump power to 0.7 mW and its polarization to H or V (using HWP2), producing signal-idler pairs with either V

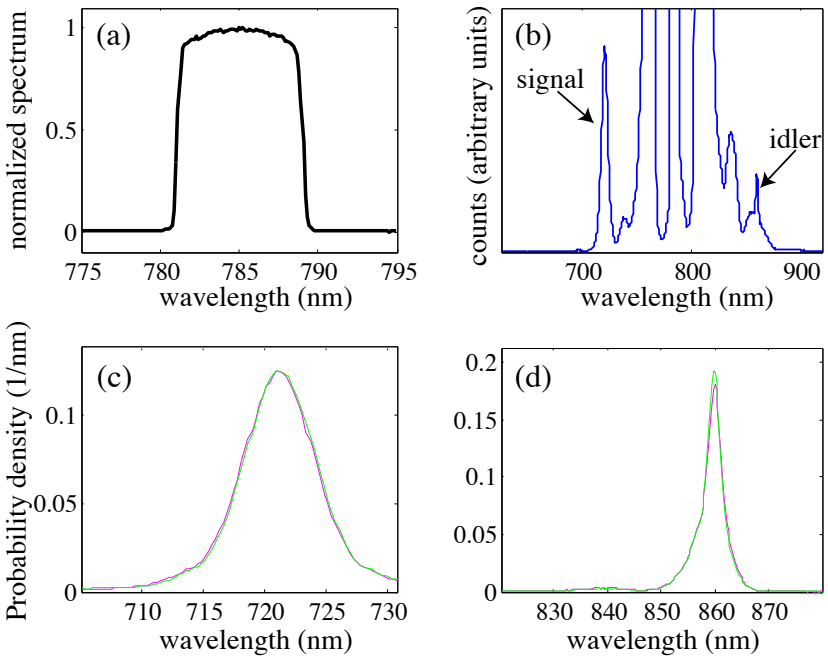


Figure 5.4 (a) Pump spectrum, centered at 785 nm with 8 nm bandwidth. (b) Full spectral output of the Sagnac-loop with 1.4 mW of total pump equally split between H and V polarizations. Note that although the idler is contaminated by Raman background, the signal is relatively clear and hence a detection of a signal photon heralds with high certainty an idler photon originating form SFWM. (c) and (d) The normalized spectral probability density for 0.7 mW of pump polarized with either V or H polarization, hence producing H (green) or V (red) polarized photon-pairs, respectively. (c) is the spectra out of the the Sagnac loop zoomed-in to the signal bandwidth, (d) shows the idler spectra as coming out of SMF in Figure 5.2.

or H polarization, correspondingly. Fig. 5.4 (c) shows the (normalized) spectral probability density $P_{sH}(\lambda)$ and $P_{sV}(\lambda)$ at the signal bandwidth for the H and V polarization, respectively. Fig. 5.4 (d) shows the spectral probability density $P_{iH}(\lambda)$ and $P_{iV}(\lambda)$ emerging out from the single-mode fiber (SMF) for the corresponding polarizations. A quantitative spectral comparison between the orthogonal polarizations is carried by defining wavefunctions with the same marginal spectrum as in

Figure 5.4 and flat phase:

$$|\phi_{\mu q}\rangle = \int d\lambda \sqrt{P_{\mu q}(\lambda)}|\lambda\rangle \ , \tag{5.10}$$

$\mu = s$ or i, $q = H$ or V, and $|\lambda\rangle$ is the state of a photon with wavelength λ. The overlap between the two signal spectra is defined by $|\langle\phi_{sH}|\phi_{sV}\rangle|^2$. Similarly, $|\langle\phi_{iH}|\phi_{iV}\rangle|^2$ defines the overlap between the two idler photons spectra. We find that the overlap of the signal photons is 99.98%, and it is 99.41% for the idler, suggesting that the generated photons in both pumping directions are, to high degree, identical copies.

5.3 Results

5.3.1 The HOM-interference

The output of the APDs were sent to a field-programmable gate array (FPGA) electronics connected to a computer. The FPGA was programmed to record, for a specified duration, the number of times each APD fired, as well as any coincident firing of more than one APD within a time window of 5 ns. The measured data of the singles, 2-fold and 4-fold counts as a function of the rotational angle θ is shown in Fig. 5.5. The total pump power is 1.4 mW, equally split at PBS2 using HWP2.

5.3.2 Normalization

Temperature variations affect the coupling efficiency into the PCF, and the 12 minute cycles in the singles counts is due to the laboratory temperature control and θ in-

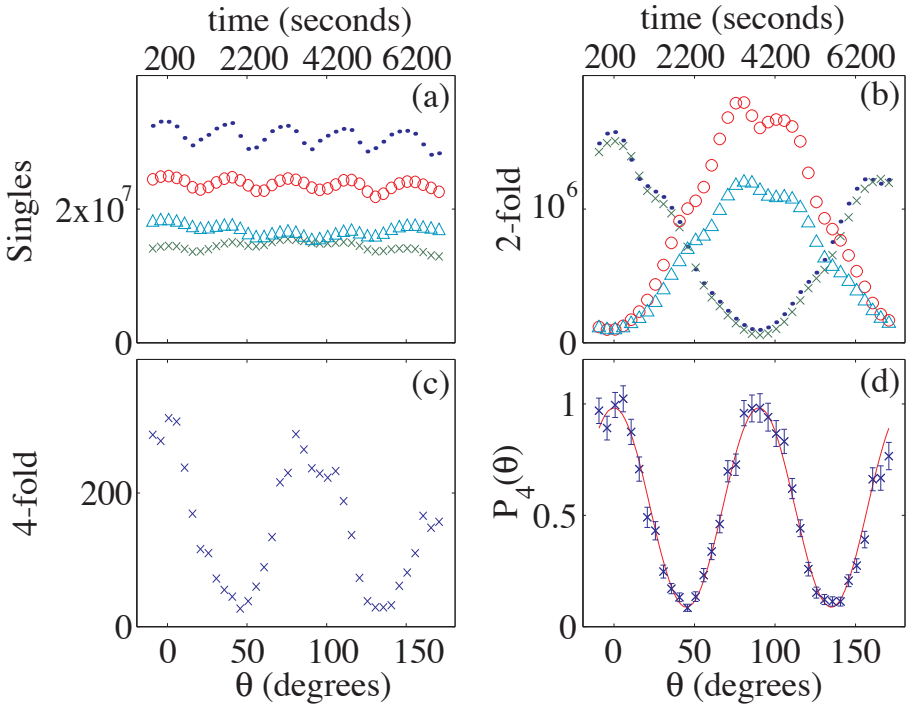


Figure 5.5 Measured counts in 100 s per data point for the polarization HOM experiment. (a) Singles counts of APDs A (·), B (×), C (○) and D (△). (b) Two-fold coincidence counts R_{AB} (·), R_{CD} (×), R_{AD} (○) and R_{BC} (△). (c) Raw four-fold coincidence counts. (d) Normalized four-fold coincidence counts with theoretical fit corresponding to purity $(82.1 \pm 1.6)\%$. Error bars represent propagated errors assuming Poissonian count statistics.

dependent. This variation in the coupling affects the generation rate. Hence, the 4-fold counts is given by

$$R_{ABCD} = F(\theta) P_4(\theta) \,, \tag{5.11}$$

where $F(\theta)$ is proportional to the number N_{trials} of pump pulses that where launched during the measurement, and also depends on the detection efficiency as well as the aforementioned generation efficiency. In order to deduce the influence of the HOM effect on the 4-fold counts, we need to normalize the results in a way that yields

the real probability of 4-fold event upon successful detection of all of the photons involved. This can be done by making use of the 2-fold counts: In the regime in which we're working, the probability that a non-vacuum sideband state emerges from the fibre is very low; looking at the singles count rates R_X ($X = A$, B, C or D in Figure 5.5), we find them to be on the order of 10^7 in 100 s. Considering the 76 MHz pulse repetition-rate, the number of pump pulses launched during this period is $N_{trials} \sim 10^{10}$, and the probability of generation is $R_X/N_{trials} \sim 0.001$. For such low probabilities, we can assume lowest order contribution when calculating coincident probabilities.

The two sources (i.e. the two counter-propagating pumps) produce photon pairs independently. The probability (per pump pulse) to generate horizontally polarized sidebands, herald an idler photon (by detection at $\mathrm{APD_A}$) and detect an idler at $\mathrm{APD_B}$ is R_{AB}/N_{trials}. Similarly, the probability of heralding a vertical idler sideband (detection at $\mathrm{APD_C}$) followed by a successful detection of idler at $\mathrm{APD_D}$ is R_{CD}/N_{trials}. Since these probabilities are independent, the chances to get coincident events of the two above detections, *in the absence of HOM interference*, is the product of the two probabilities $R_{AB} \times R_{CD}/N_{trials}^2$. Due to the polarization rotations, the 2-fold coincidence also occur between signal at $\mathrm{APD_A}$ and idler at $\mathrm{APD_D}$, or $\mathrm{APD_B}$ and $\mathrm{APD_C}$. The coincidence probability of these two events is $R_{AD} \times R_{BC}/N_{trials}^2$, and the total expected 4-fold probability, *if no bunching effect occurs*, is

$$P_{classical} = \frac{R_{AB} \times R_{CD}}{N_{trials}^2} + \frac{R_{AD} \times R_{BC}}{N_{trials}^2} \,. \tag{5.12}$$

Indeed, the above equation holds when the two interfered photons are distinguishable: in this case the two paths that separate the photons do not interfere and the coincidence is classical. Substituting $p = 0$ in Eq. (5.9), using Eq. (5.11), and equating to $P_{classical}$, we obtain

$$\frac{R_{AB} \times R_{CD}}{N_{trials}^2} + \frac{R_{AD} \times R_{BC}}{N_{trials}^2} = \frac{F(\theta)}{N_{trials}} \frac{1}{2} \left[1 + \cos^2(2\eta)\cos^2(2\theta)\right] . \tag{5.13}$$

Note that $P_{classical}$ is calculated from the experimental data, relying only on the 2-fold coincidences and sets the classical expectation for 4-fold counts ($P_{classical} \times N_{trials}$). The experimentally observed 4-fold probability (with the interference), is, however, given by R_{ABCD}/N_{trials}. Using Eqs. (5.9), (5.11) and (5.13), together with the experimental 4-fold probability, we derive the equation

$$\frac{R_{ABCD} \times N_{trials}}{[(R_{AB} \times R_{CD}) + (R_{AD} \times R_{BC})]} = 1 - p\frac{1 - \cos^2(2\eta)\cos^2\left(2(\theta + \theta_0)\right)}{1 + \cos^2(2\eta)\cos^2\left(2(\theta + \theta_0)\right)} . \tag{5.14}$$

Eq. (5.14) connects the experimental data (left-hand side) with the theoretical prediction (right-hand side), avoiding the cycling amplitude. A fit, with p, η and θ_0 as free parameters enables us to plot the normalized 4-fold coincidence given by Eq. (5.9) with the fitted parameters. Note that θ_0 is required as a free parameter because we do not know the exact polarization coming out of SMF followed by QWP.

The experimental normalized 4-fold is shown in Figure 5.5 together with the theoretical fit, which corresponds to a purity of $(82.1 \pm 1.6)\%$. The error bars are the propagating errors calculated assuming Poissonian distribution of the counts

(i.e. the error in R_{XY} is $\sqrt{R_{XY}}$ and in R_{ABCD} is $\sqrt{R_{ABCD}}$).

Chapter 6

Effect of experimental parameters

We have demonstrated the ability of our scheme to generate pure heralded photons. In this chapter we study theoretically and experimentally the influence of various parameters, which can be controlled in the laboratory, on the purity of the individual photons in the produced photon-pair.

6.1 Fibre length

In Chapter 3 it was discussed that one can enhance the purity of the heralded photons by extending the fibre length and narrowing the the pump bandwidth accordingly. Consequently, our model predicts purity of $p = 98.5\%$ with $L = 100\,\mathrm{m}$ and $\Delta\lambda_p = 0.32\,\mathrm{nm}$. In order to validate the dependency of the purity on the fibre length, we

repeated the HOM-interference experiment with a 1 m of the same model of PCF. This sample was purchased at a later time, and therefore we could not assume its similarity to the previously used PCF. Hence, we characterized the new sample by measuring the sideband wavelengths it generates as a function of pump wavelength, shown in Figure 6.1. The step-index model fit yields the parameters $d_{fast} \cong d_{slow} \cong 1.7442\,\mu$m, $r_{fast} = 51.2\%$ and $r_{slow} = 51.0\%$, predicting the GV-matching point at $\lambda_p = 785$ nm – slightly different from the prediction with the 40 cm fibre model (783 nm) plotted in Figure 4.4. The measurements show that the GV-matching wavelength, for this longer fibre, is at $\lambda_p \approx 786$ nm.

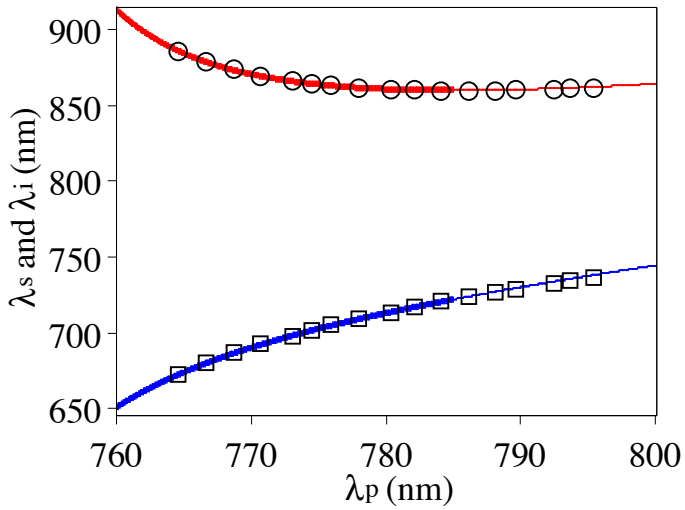


Figure 6.1 Measured signal (squares) and idler (circles) central wavelengths as a function of pump wavelength with 1 m of the PCF NL-1.8-750. The solid lines are the step-index model fit, thin sections indicate where factorability is possible. In particular, the join between the thick and thin lines is where the signal GV matches the pump.

Numerical calculations of the purity for $\lambda_p = 785$ nm and $\Delta\lambda_p = 6$ nm yielded $p = 90\%$. We set the experiment with $\lambda_p = 786$ nm, $\Delta\lambda_p = 6$ nm, and total pump

power 1.4 mW. Figure 6.2 shows the counts and coincidences in 200 s for each data point. The fit to the normalized 4-fold coincidences corresponds to $p = (85.9 \pm 1.6)\%$. Comparing with the purity ($p = 82.1\%$) obtained using the 40 cm PCF (see Figure 5.5), we confirm the increase in achievable purity with a longer fibre.

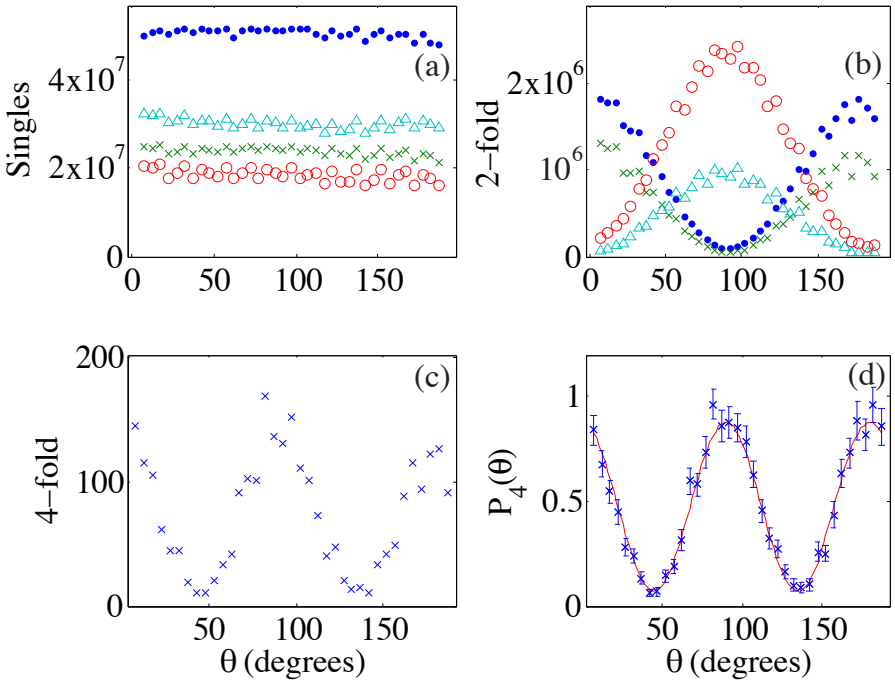


Figure 6.2 Measured counts in 200 s per data point for the polarization HOM experiment with 1 m of PCF. (a) Singles counts of APDs A (·), B (×), C (○) and D (△). (b) 2-fold coincidence counts R_{AB} (·), R_{CD} (×), R_{AD} (○) and R_{BC} (△). (c) Raw 4-fold coincidence counts. (d) Normalized 4-fold coincidence counts with theoretical fit corresponding to purity $(85.9 \pm 1.6)\%$ (compare with Figure 5.5). Error bars represent propagated errors assuming Poissonian count statistics.

6.2 Birefringence fluctuations

Our models assume uniform waveguides, meaning that the refractive index and the birefringence do not vary along the fibre. Nonetheless, nonuniformity is unavoidably

imposed both at the fabrication process and the conditions in the laboratory – mainly bends of the fibre. In our case, the main effect of the nonuniformity is expressed via birefringence *fluctuations*, giving rise to fluctuating phase-matching conditions, meaning that the central wavelengths at which the signal and idler produced jitter as the pump propagates through the fibre. We calculated the shift applied to these wavelengths when *additional* small birefringence δn is imposed. We found that for $\delta n = \pm 10^{-6}$ the sidebands central wavelengths shift by about 3 nm. For $\delta n = \pm 10^{-7}$ the shift is 0.3 nm. Considering our narrow bandwidth idler (less than 1 nm) birefringence fluctuations of the order of 10^{-7} (and obviously higher than that) can broaden it and potentially affect the joint spectral amplitude. Unfortunately, we don't have the means to measure such a tiny variation in the birefringence, and we do not know to what extent the fibre is uniform. The small differences between our two (same model of) fibres confirms our concern of nonuniformity between fibres, and suggest that nonuniformity within fibres also plays a significant role.

6.3 Pump power

As was mentioned before, the effect of the pump power through the nonlinear term in the phase-matching function is not clear. We tested the influence of pump power on the HOM-interference and the deduced purity. The pump bandwidth $\Delta\lambda_p = 8\,\text{nm}$ at $\lambda_p = 785\,\text{nm}$ implies pulse duration $\tau_p \approx 125\,\text{fs}$. The peak power $P_0 \sim \bar{P}/(\tau_p \times reprate)$ where $reprate = 76\,\text{MHz}$ is the repetition rate of the oscillator, and $\bar{P} \sim 1\,\text{mW}$ is the average pump power. The nonlinearity as reported by

Crystal-Fibre is $\gamma \approx 100\,[\mathrm{W\,km}]^{-1}$. Thus, the index shift imposed by the SPM and XPM is of the order of $\gamma P_0 \lambda_p / 2\pi \sim 10^{-6}$, which is an order of magnitude smaller than the birefringence, meaning that the main contribution to the phase-matching wavelengths is due to fibre birefringence. However, as we mentioned earlier, numerical calculations show that an additional induced index on the order of 10^{-6} can shift the sidebands wavelengths by 3 nm and the pump GV-matching wavelength by 1 nm. Therefore, if the nonlinear term estimates correctly the effect of SPM and XPM, then this effect is not neligible. We experimentally investigated the influence of pump power on the SFWM. First, the spectra of the sidebands for various pump power $(0.2 - 1.4)$ mW was taken. We found that their central wavelengths and the signal bandwidth (standard deviation) varied by ± 0.5 nm at most, as can be seen in Figure 6.3. It is difficult to decide how to measure accurately the idler bandwidth as it is contaminated by the Raman scattering (see Figure 5.4). In order to validate that the variations are indeed due to power and not a statistical error, we measured the above quantities for 10 shots with pump average power of 0.7 mW. We found that the fluctuations are less than 0.05 nm, which is negligibly small compared to the observed variations due to power change. Second, we measured the purity for total pump average power $(0.7 - 1.4)$ mW per source, and found that as long as $\bar{P} < 1$ mW the purity is not affected, but degrades at higher power. We attribute the degradation to either or all of the following: higher order terms in the FWM interaction (i.e. the production of more than one pair per source), the increase in the accidental coincidences of a signal detection with a Raman Stokes photon (i.e.

heralding a mixed state composed of SFWM idler and a Raman photon), as well as the time dependency of the SPM with XPM which creates time-varying phase-matched sidebands.

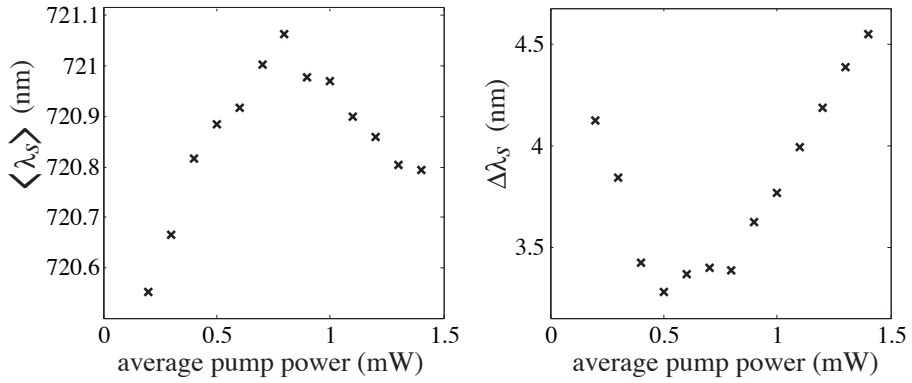


Figure 6.3 The experimentally measured average signal wavelength (left) and standard deviation bandwidth (right) as a function of average pump power with $\lambda_p = 785\,\text{nm}$.

6.4 Pump spectrum

Choosing correctly the pump characteristics is the key to implement the factorability scheme introduced in this thesis. We now investigate the sensitivity of the photons' purity to the pump spectrum:

6.4.1 Pump wavelength and bandwidth

The factorability scheme we use here employs the GV-matching between the signal and pump. It is therefore vital to centre the pump at the correct wavelength where this matching occurs. Moreover, although the general idea of the scheme requires a broad pump, the bandwidth has to be narrow sufficiently such that dispersion can be

neglected. In particular, as can be seen in Figure 4.5, the phase-matching function is not a straight line but rather curved due to second order contribution in the phase-mismatch. Therefore, the pump envelope needs to be narrow enough such that it's overlap with the curvature is minimal (note that while this argument is exact in the SPDC process, in SFWM one might be limited more strictly by the pump dispersion which was neglected and hence doesn't appear in the phase-matching function).

The trade-off between the two effects of pump bandwidths necessitates optimization in order to achieve the best purity that the scheme provides. We calculated numerically the purity of the photons produced in our 40 cm PCF model with pump shifted by 1 nm from the GV-matching wavelength. We found that the purity varied by about 1%. We also varied the pump bandwidth by 1 nm, resulting in purity variations of 1% at most. These theoretical calculations then predict a minor sensitivity of the purity to the exact selected pump. Experimentally, however, we found that such variations raised a degradation of the purity by $5\% - 10\%$. This implies that in effect one needs to accurately set the pump spectrum and not rely on a numerical optimization using the model. Indeed, the results shown in Figures 5.5 and 6.2 were obtained after experimental optimization had taken place.

6.4.2 Pump spectral envelope shape

Another assumption the scheme relies on is the approximated joint amplitude given by Eqs. (2.44), where the pump envelope was assumed to be Gaussian. However, this is not necessarily the case one realizes experimentally, and indeed, our im-

plementation uses a different pump envelope (the tunable filter has sharp edges). While it seems as if a Gaussian envelope is crucial in the cases of $0^o < \theta_{si} < 90^o$, the $\theta = 0^o, 90^o$ rely solely on a very narrow phase-matching function $\phi(\nu_s, \nu_i)$ and therefore the exact pump envelope is not significant. In practice, however, our phase-matching function is not that narrow (the bandwidth of the idler is only about 4 times narrower than the signal), and hence the shape of the pump envelope can take part in the factorability of the produced state.

We used the model to calculate the purity of the photons with a Gaussian pump envelope. We found that pumping 40 cm of the modeled PCF with bandwidth 6.8 nm (FWHM) generates photons with higher purity $p = 90\%$, and it reaches 93% with 1 m of the fibre with pump bandwidth of 3.8 nm. The joint spectral probability of this analysis is shown in Figure 6.4.

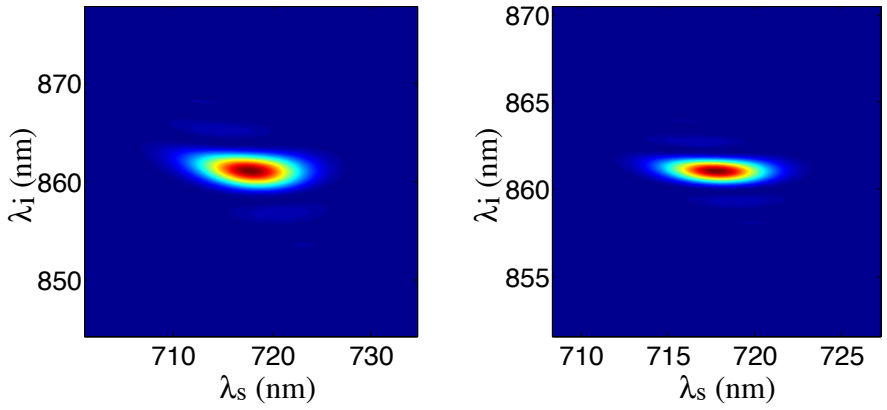


Figure 6.4 The joint spectral probability calculated for our model with $L = 40$ cm (left) and $L = 1$ m (right), and corresponding FWHM bandwidth of Gaussian pump envelope 6.8 nm and 3.8 nm. The calculations of the associated purity resulted in 90% and 93%, respectively.

We set out to test this prediction. As was mentioned, our experimental attempts

exhibited an appreciable sensitivity to the pump wavelength and bandwidth, and hence it was essential to implement the Gaussian spectral filter such that it was tunable. We did it by closing the slit in our tunable filter (Figure 4.1) to the minimal resolution, resulting in a wavelength tunable monochromator outputting a Gaussian spectral bandwidth of 0.5 nm FWHM. The bandwidth of the beam was adjusted by displacing the slit from the lens' focal plane, thus degrading the resolution of the monochromator and broadening the bandwidth to our desire.

We repeated the HOM-interference experiment with the 40 cm PCF and a Gaussian spectrum, taking measurements with various central wavelengths and bandwidths. Unfortunately however, the purity did not increase beyond the one obtained with the rectangular filter, and only matched it with $\lambda_p = 785\,\text{nm}$ and $\Delta\lambda_p = 4\,\text{nm}$ (FWHM). We may try to understand the origin of the discrepancy between the theoretical prediction and experimental data by looking at the marginal spectrum of the signal: Figure 6.5 shows the theoretical and experimental spectrum of the signal for fibre length of 40 cm and pump central wavelength chosen at GV-matching. The theory predicts Gaussian signal spectrum for Gaussian pump. For a rectangular filter, the model yields a signal spectrum with less than 93% overlap with a Gaussian having the same standard-deviation bandwidth. However, the experimental observation shows that in both cases the signal spectrum is Gaussian: taking the experimental signal spectrum in the case of rectangular filter, and calculating its overlap with a Gaussian bandwidth equal to the measured $\Delta\lambda_s = 3.4\,\text{nm}$ (standard deviation) yields 99.5% fidelity. This discrepancy between the theory and the ex-

periment suggests the existence of an additional mechanism that our theory does not account for. We believe this lies in birefringence variations along the fibre: very small birefringence fluctuations – on the order of 10^{-7} – can affect dramatically the joint spectral amplitude, and may be responsible for smoothing out its "hard edges" (see Figure 4.5). Unfortunately, measuring such tiny variations is very challenging. Moreover, the exact nature of the birefringence in PCFs is not well studied[128], making it difficult to model appropriately its effect.

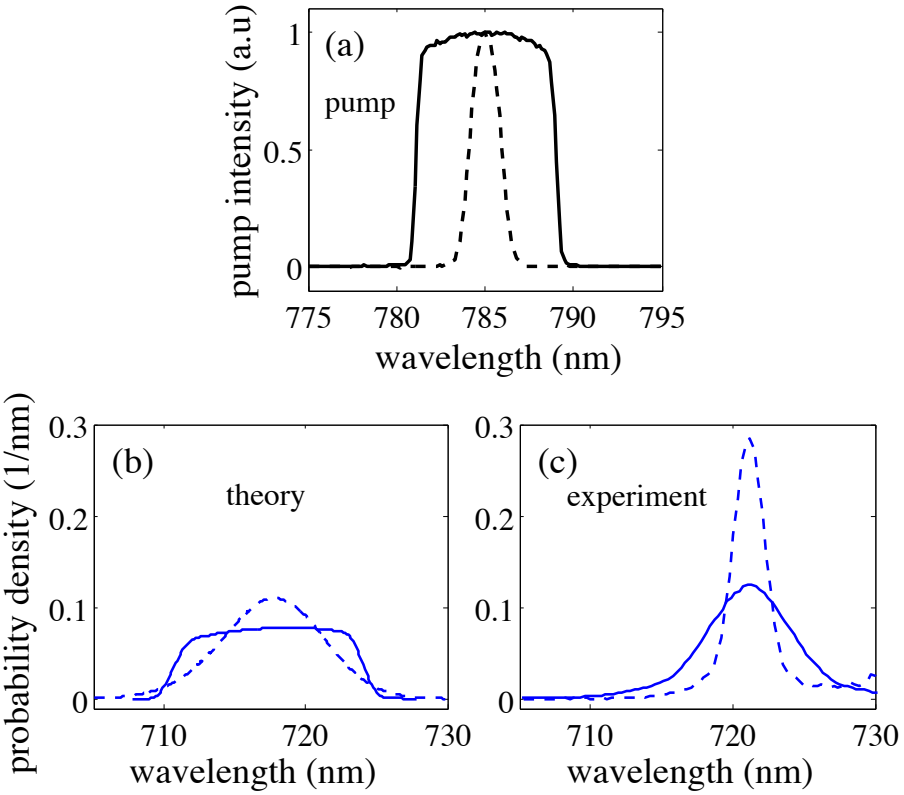


Figure 6.5 Experimental and theoretical specra. a) Measured pump spectra obtained by filtering the laser with a rectangular (solid curve, FWHM $\Delta\lambda_p = 8\,\text{nm}$) and Gaussian (dashed curve, FWHM $\Delta\lambda_p = 4\,\text{nm}$) filter. (b) theoretical spectra of the signal produced by a rectangular (solid) and Gaussian (dashed) pump spectrum. (c) experimental spectra of the signal, measured with rectangular (solid) and Gaussian (dashed) pump spectrum.

As the technique to generate pure heralded photons in optical fibres seems promising, further investigation of the obstacles that limit our source and tackling them may turn to be of great benefit. Particularly, uniformity along and between PCFs has to be addressed before such a source can fulfill its potential.

6.5 Signal to noise considerations

Spontaneous Raman scattering, which randomly generates photons at the idler port, acts as the main contamination to our photon-pair source. In this section we study how the signal to noise ratio is affected by the choice of pump power and bandwidth with appropriately selected fibre length (to maintain factorability).

The factorability condition given by Eq. (3.28) forms a linear relationship between the fibre length and pump pulse duration $\tau_p \sim 1/\sigma_p$. As has been stated and experimentally confirmed, the validity of this approximation enhances as both of these parameters get larger, increasing the purity of the heralded photons. We now study how they affect the contrast between the photon-pair generation to Raman background. First, let's calculate the dependency of the photon-pair generation probability on the various parameters we control or measure in the laboratory. Although these calculations can be carried out in the frequency domain using Eq. (2.36), it is more intuitive to carry them in the time domain: SFWM, being a local interaction, takes place at the pump location in the fibre. For a given time interval $[t, t + \Delta t]$, the probability to generate spontaneously a photon-pair within the interval $[z, z + \Delta z]$ along the fibre is the probability that two pump photons in

these intervals interact, which is proportional to the square of the number of pump photons within this volume. In other word, this probability is proportional to the square of pump energy inside these intervals. The pump power at point z and time t can be written as $P_p((z/v_p - t)/\tau_p)$, where P_p is the power temporal distribution in the fibre with a spread of τ_p around its peak value P_0. This power travels with the pump group velocity v_p. Hence,

$$P_{SFWM} \propto \int_0^{L/v_p} dt \int_0^{L} dz P_p^2 \left(\frac{z/v_p - t}{\tau_p} \right) , \tag{6.1}$$

where P_{SFWM} is the probability to generate a photon-pair by a single pump pulse. Carrying the integration assuming $v_p \tau_p \ll L$ (the pump pulse is much shorter than the fibre length), this probability is proportional to $L\tau_p P_0^2$. In practice, one usually measures the average pump power $\bar{P} \sim P_0 \tau_p \times reprate$ where $reprate$ is the laser repetition rate. Substituting the factorability condition $L \propto \tau_p$, we obtain:

$$P_{SFWM} \propto \left(\bar{P}/reprate \right)^2 . \tag{6.2}$$

Thus, the probability to generate a photon-pair in a pump pulse is quadratic with pump power over the laser repetition, and does not depend on the fibre length or pump bandwidth so long as the factorability constraint is maintained.

In the spontaneous Raman process, a single photon from the pump interacts with the medium and scattered inelastically. Thus, the probability P_{Stokes} of finding a Stokes photon generated by a pump pulse is proportional to the number of photons

in that pulse, i.e., the energy it carries. Hence

$$P_{Stokes} \propto \bar{P}/reprate \ . \tag{6.3}$$

Naively, for a fixed repetition rate, one would think that increasing the pump power increases the signal to noise ratio between the SFWM and Raman Stokes photons, as the first grows quadratically with the power while the latter only linearly. However, we are actually interested in the coincidences, and the Raman contamination adds to the false coincidences with a signal photon. The probability of detecting coincidentally a signal-idler pair originating from SFWM is $\eta_s \eta_i P_{SFWM}$ where η_s and η_i are the detection efficiencies of the signal and idler, respectively. The probability of false coincidence detection of signal and Stokes photons is $\eta_s \eta_{Stokes} P_{SFWM} P_{Stokes}$, where η_{Stokes} is the detection efficiency of the Stokes photon. Thus, the ratio of the false to true coincidence probabilities is

$$\frac{\eta_{Stokes}}{\eta_i} P_{Stokes} \propto \bar{P} \ . \tag{6.4}$$

It turns out, then, that the ratio of the Raman contamination to the coincidence increases linearly with power. We can understand this by making the following argument: once we detect a signal photon, we *know* there exists an idler photon, and the reason for failing to detect it is due to the inefficiency in the detection and does not depend on the power. The probability of a Raman photon to trigger the detector at the idler arm is not affected by the post-selection of the signal registration events,

therefore still depends on pump power. Hence, the overall false coincidence scales with the power of the pump – the lower the power, the lesser the false coincidence contamination. This result is unfortunate, as it restricts the maximal power we can use, and hence the pair-generation rate. It is therefore important to reduce the Raman noise by other means, such as engineering the source to satisfy the phase-matching conditions with higher detuning of sidebands from the pump. One way of obtaining this is by using a fibre with high birefringence.

Chapter 7

Standard fibres

So far we have concentrated on the use of PCFs as the waveguide in which factorable photon-pairs are generated. This is due to the high nonlinearity of these fibres that makes them a bright sources of photon-pairs, and because of the flexibility in manufacturing such fibres – supplying a wide selection with various characteristics to choose from. However, the PCF industry is relatively young, and the production of photon-pair states with tailored spectral properties requires this industry to address new challenges, such as the uniformity within and between fibres. Until this difficulty is overcome, the potential of PCFs to implement SFWM cannot be fully exploited.

Photon purity and indistinguishability is significant, particularly, for experimental setups relying on the HOM-type interference, such as implementations of LOQC schemes. This interference requires a good spatial overlap of the interfered photons – a difficult task to carry out in free-space. The fibre industry offers beamsplitters implemented by coupling two single-mode fibres. This implementation promises al-

most perfect mode overlap, and therefore is useful in a realization of two-photon interference. However, the use of any generated photons in fibre-network optical circuits requires the coupling of these photons into the network. The coupling efficiency is limited by the mode overlap between the photons and the network's guided modes, or, in the above case, between the photon-pair source and single-mode standard fibres. Recently, a good spatial mode overlap in the interface between PCFs and standard fibres has been demonstrated using end-tapered PCFs [129]. It is, however, advantageous to generate the photons in standard fibre sources, where the modes match the ones in the fibre networks, allowing maximal coupling and minimal losses. Moreover, the maturity and relative simplicity of the standard fibre fabrication technique, in comparison to its PCFs counterpart, raises the possibility that they are more uniform. One additional practical benefit in using standard fibres rather than PCFs is the cost: the latter is about 100 times more expensive than the former. The use of standard fibres can therefore lower setup expenses significantly, especially when multiple sources are incorporated (on the other hand, their lower nonlinearity requires higher pump power, which could increase costs).

This chapter presents theoretical study with experimental results demonstrating the potential to generate a factorable photon-pair state in standard birefringent fibres.

7.1 Model

The birefringence in silica optical fibres is introduced by inducing stress on the core. This is usually done by manufacturing the fibre with rods in the cladding that add asymmetric stress but do not take part in the guiding itself. Two types of such rods are commonly used, those are the "Panda" and "Bow-tie", see Figure 7.1.

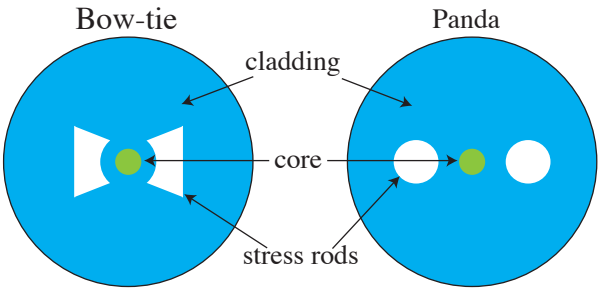


Figure 7.1 Polarization maintaining fibres. The rods induce stress on the core in an asymmetric way, giving rise to polarization dependent propagation, and hence birefringence.

A suitable model for the dispersion in any waveguide needs to consider both the dispersion of the materials of which it is fabricated and the geometry. Using Eq. (3.24), for pump wavelengths far from the ZGVD, the main contribution to the phase-matching wavelengths depends on the fibre's β_2 parameter. We write the effective wave-vector as the composition $k(\lambda) = k_M(\lambda) + k_W(\lambda)$, where k_M is the material dispersion – pure silica in our case – and k_W is the waveguide dispersion. Since the concentration of dopant in standard fibres is very low (typically $< 1\%$), k_W imposes only a minor correction to the fibre dispersion. Therefore, it is sufficient to approximate the dispersion as the one given by bulk silica. However, for pump close to λ_{ZGVD}, the waveguide and material contributions to β_2 become comparable, and

this approximation breaks[103].

Our model for standard birefringent fibres consists of the Sellmeier equation for pure silica to simulate the dispersion in silica waveguides. We assume a wavelength independent birefringence Δn added to one of the polarizations in the waveguide. Thus,

$$\begin{aligned} k_x(\omega) &= n_{silica}(\omega)\tfrac{\omega}{c} \,, \\ k_y(\omega) &= k_x(\omega) + \Delta n \tfrac{\omega}{c} \,, \end{aligned} \tag{7.1}$$

where k_x and k_y are the effective wave-vectors of the beams polarized along the waveguide's principal axes x and y, respectively.

7.2 Experimental validation

In order to check the validity of our model, we mapped the phase-matching contour of the standard birefringent fibre Fibercore HB750, see Figure 7.2. This is a "Bow Tie" style fibre with single-mode cutoff wavelength specified to lie within $(610 - 750)$ nm. The measured data were taken with the home-built spectrometer in which we could not identify the idler wavelength. We fitted the birefringence to the data and found $\Delta n = 3.4 \times 10^{-4}$, yielding a good agreement (less than 2 nm discrepancy), which demonstrates the reliability of the model.

Measurements of the phase-matching curve and joint spectral probability on another fibre (Fibercore HB800G) by Smith *et al.*[130] resulted as well in a good overlap with the above model, exhibiting its ability to predict accurately the photon-pair state generated in standard fibres.

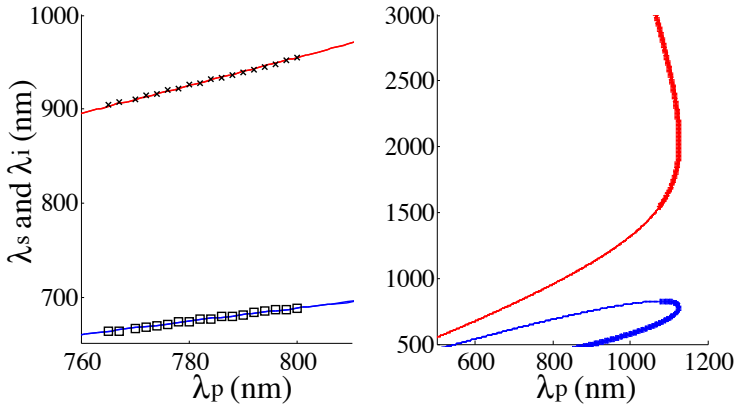


Figure 7.2 Phase-matching contour for the standard birefringent fibre Fibercore HB750. Left: the measured signal wavelength (rectangles) and inferred idler (X) wavelength by energy conservation. The solid lines correspond to the theoretical curve, assuming dispersion of pure silica and fitted birefringence $\Delta n = 3.4 \times 10^{-4}$. Right: a wider range of the phase-matching contour according to the model. Thin lines indicate the section where factorability is possible.

The phase-matching contour shows that factorability is possible at every wavelength in the scanned range, and according to the model also way beyond it. This means that one needs not to worry about the exact central wavelength of the pump, but rather only about the bandwidth *or* fibre length, making experimental optimization a lot easier compared to the GV-matching case.

7.3 Factorability in standard fibres

Using the fibre model (dispersion of pure silica) with the fitted birefringence, we calculate the purity of the heralded photons generated through SFWM. We find that for pump $\lambda_p = 700\,\text{nm}$ the signal and idler are generated at $\lambda_s = 616\,\text{nm}$ and $\lambda_s = 810\,\text{nm}$. The purity of the photons are found to be $p = 86\%$ for fibre length $L = 5\,\text{cm}$ and pump bandwidth $\Delta\lambda_p = 1\,\text{nm}$ (Figure 7.3). Again, by using bandpass

filters that transmit the main lobe of the joint spectral amplitude, one can increase the purity appreciably with little expense. For example, using a rectangular 2 nm bandwidth filter on the signal photon, the purity increases to $p = 95\%$ while reducing the total pair generation probability only by 6%, without affecting the heralding efficiency (provided that the signal is used as the heralding photon). These results mean that with a picosecond pump and few centimetres of fibre, one can achieve a factorable state. The use of a short fibre (compared to the about 50 cm of PCF that we have used) reduces the significance of non-uniformities.

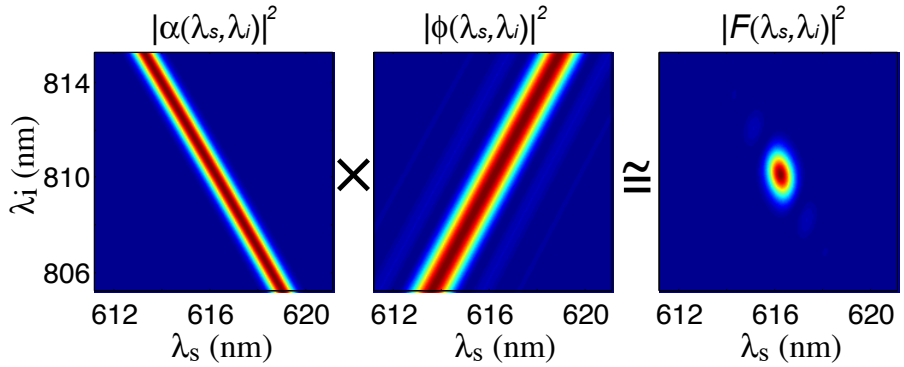


Figure 7.3 The pump envelope (left), phase-matching function (middle) and the joint spectral probability (right) calculated for $\lambda_p = 700\,\text{nm}$, $\Delta\lambda_p = 1\,\text{nm}$ (FWHM) and $L = 5\,\text{cm}$ with the birefringent standard fibre model assuming silica dispersion and birefringence of $\Delta n = 3.4 \times 10^{-4}$. The corresponding purity is $p = 86\%$

7.4 Towards measuring purity

An experiment testing the purity of the heralded photons generated in standard birefringent fibres is being conducted in collaboration with Christine Silberhorn's group at the Max Planck Institute for the Science of Light in Erlangen. This group

possesses a picosecond pulse duration 76 MHz laser that can be tuned down to $\lambda_p = 716\,\text{nm}$ with measured bandwidth (FWHM) $\Delta\lambda_p = 0.4\,\text{nm}$. Since the magnitude of the birefringence dictates the detuning of the sidebands from the pump, Smith *et al.*[130] measured the birefringence of numerous commercial fibres and studied the photon-pair properties generated in the fibre exhibiting the highest birefringence – Fibrecore HB800G. They found $\Delta n = 4.3 \times 10^{-4}$ for that fibre. The high birefringence provides a detuning of $\Omega_{si} = 65\,\text{THz}$, where the Raman gain is negligibly small (see Figure 2.7). The usage of pump wavelength around 700 nm guaranteed the idler photon to be within the detection bandwidth of silicon based APDs. The purity demonstration experiment is therefore carried with this fibre.

According to the described model, the signal and idler for $\lambda_p = 716\,\text{nm}$ are generated at $\lambda_s = 618\,\text{nm}$ and $\lambda_i = 851\,\text{nm}$, with bandwidths (FWHM) $\Delta\lambda_s = 0.32\,\text{nm}$ and $\Delta\lambda_i = 0.63\,\text{nm}$. Numerical optimization of the fibre length to produce the highest de-correlated pair yielded $L = 12\,\text{cm}$ with purity $p = 88.5\%$. A sharp edge bandpass filter with $\Delta\lambda_f = 0.7\,\text{nm}$ centered at the signal wavelength may transmit more than 95% of the signal and increase the purity to over 96%. Figure (7.4) presents the joint spectral probability for this case.

The proposed HOM setup to test the purity of the heralded photons is sketched in Figure (7.5). HWP1 with PBS1 control the total pump power. PBS2 clears the polarization. A short-wavelengths pass filter (SPF1, Thorlabs FES0800, cut-off at 800 nm) and long-wavelength pass filter (LPF1, Semrock LP02-664RS-25, cut-on at 664 nm) are used to clean the pump spectrum. HWP2 sets the power sharing be-

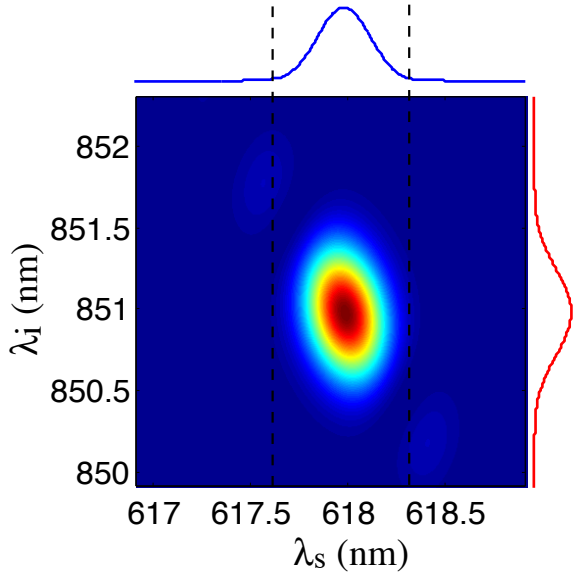


Figure 7.4 Theoretical joint spectral probability calculated for birefringent standard fibre with $\Delta n = 4.3 \times 10^{-4}$, pump launched on the slow axis at $\lambda_p = 716\,\text{nm}$ and bandwidth $\Delta\lambda_p = 0.4\,\text{nm}$ (FWHM). Fibre length is $L = 12\,\text{cm}$. The associated purity is $p = 88.5\%$. The curve at the top and the one to the right present the marginal spectra of the signal and idler, respectively. A filter transmitting the bandwidth (0.7 nm) enclosed by the dashed lines and rejecting the rest blocks only 5% of the signal flux and increases the purity to 96%.

tween the two photon-pair sources, and PBS3 splits the pump towards them. Arms A and B are identical, except arm A has an addition of variable delay. We first set-up arm B. HWP6 aligns the pump polarization with the slow axis of the birefringent single-mode fibre (BSMF2) used as the source. A microscope objective ×20 (L5) couples the pump into BSMF2. AHWP2 with PBS5 are used to filter the sidebands polarization and suppress pump and other background. The dichroic-mirror DM2 (Comar 700 BK 25, transition wavelength at 700 nm) separates the signal and idler wavelengths. The former is reflected. A bandpass filter BPF2 (Semrock FF01-617/73-25, 37 nm bandwidth centered at 607 nm) is used to suppress further the

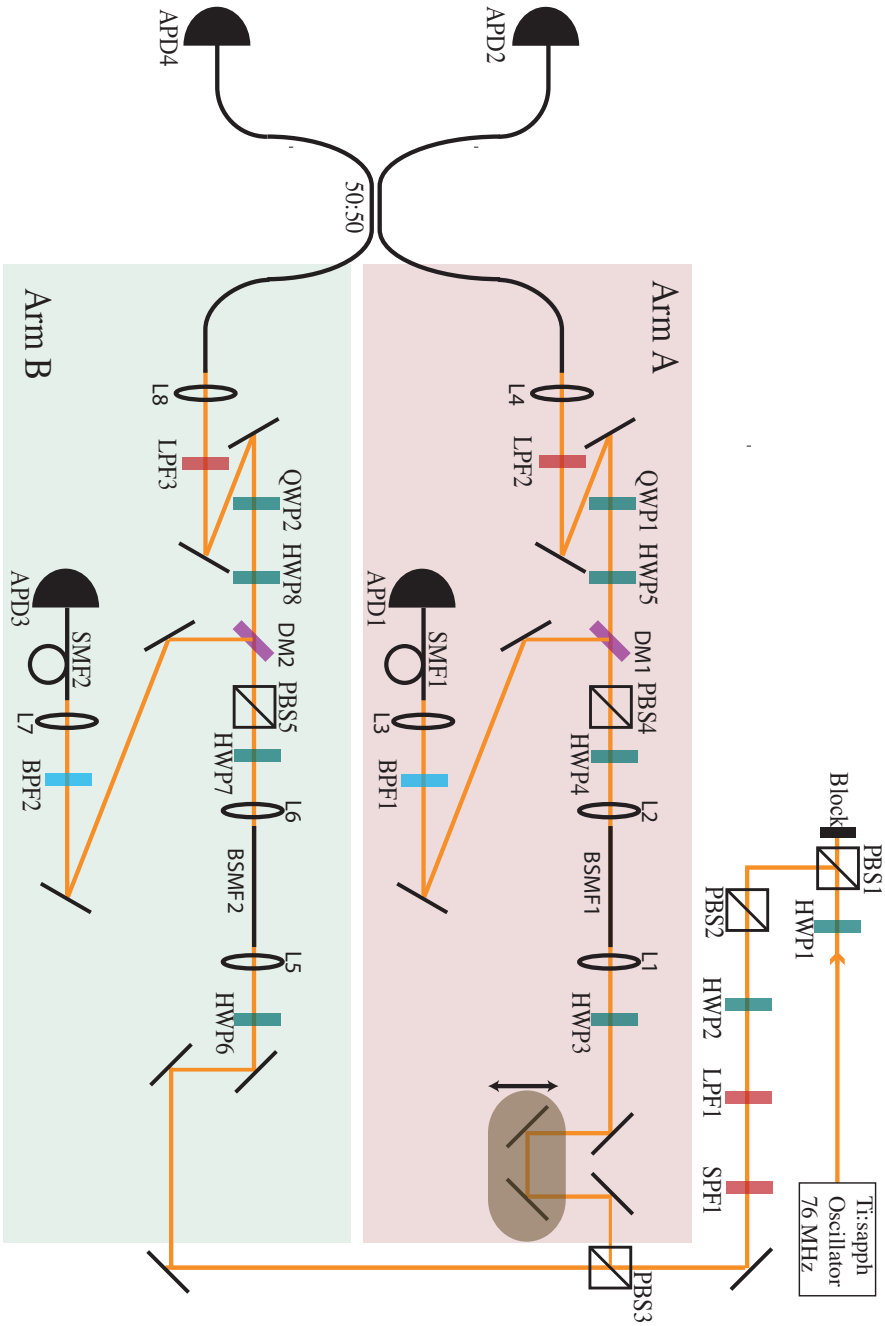


Figure 7.5 The proposed HOM setup for the purity test of the heralded photons in standard birefringent silica fibre.

pump and transmits the signal. An aspheric lens (L7) couples the signal into into a single-mode fibre (SMF2) connected to APD3. A detection heralds an idler photon, which is transmitted through DM2, then goes through a pre-compensating polarization control applied by HWP8 and QWP2. A long-wavelength pass filter (LP2, Semrock LP02-830RU-25, cut-on at 840.8 nm) is angle tuned such that it transmits the idler bandwidth and suppresses pump and Raman background at shorter wavelengths. It is then coupled into a single-mode fibre-coupler (FOC SWC). The HOM interference with a heralded idler at arm A occurs at this coupler. The polarization pre-compensation will be used to make sure both heralded photons arrive with identical polarizations at the interference point.

7.5 Observation of photon-pairs

We measured the spectrum of SFWM with pump average power $P = 50\,\mathrm{mW}$ (Figure 7.6). This was carried by coupling the output end of SMF2 to the spectrometer (Shamrock 163 spectrograph with 600 grooves/mm grating and attached Newton CCD camera) and merging with the measurement taken with one of the outputs of the fibre-coupler. The signal photon is produced at $\lambda_s = 619\,\mathrm{nm}$ and the idler at $\lambda_i = 848\,\mathrm{nm}$.

We then measured the counts rate of APD3 (S), APD4 (I) and their coincidences occurring within a time window of 5 ns (C), using an FPGA connected to a computer.

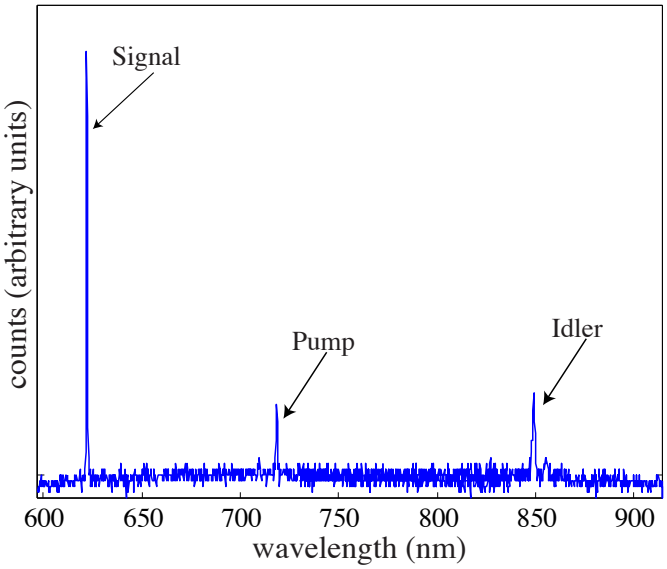


Figure 7.6 The SFWM gain in the fibre Fibercore HB800G, for $\lambda_p = 716\,\text{nm}$ with $\Delta\lambda_p = 0.4\,\text{nm}$ (FWHM). The signal and idler photons appear at $\lambda_s = 619\,\text{nm}$ and $\lambda_i = 848\,\text{nm}$, respectively.

We found:

$$\begin{aligned} I &= 33000\,\text{Hz} \\ S &= 22750\,\text{Hz} \\ C &= 975\,\text{Hz} \end{aligned} \tag{7.2}$$

and hence

$$g^{(2)} = \frac{C}{I \times S} \times (76\,\text{MHz}) = 98.7 \gg 1\,, \tag{7.3}$$

proving the high (non-classical) correlations between the signal and idler beams.

Setting up the experiment is in progress. The complete setup will provide experimental quantification of the indistinguishability between heralded photons from independent sources, without spectral filtering. The high birefringence provides high detuning of the sidebands from the pump, reducing and almost eliminating

the Raman background. Also, the generation in the single-mode fibre ensures high coupling efficiency into the single-mode fibres used to herald and interfere, raising the standard fibre as an excellent candidate for highly efficient heralded photons source.

Chapter 8

Summary

The generation of heralded photons in a pure wave-packet is a crucial source for many quantum optics experiments and applications. Most experiments to date use spectral and spatial filters to project mixed-state single-photons onto a pure state, and by doing so reject most of the photonic flux, hence degrading both the efficiency of experimental resources and reliability of the source as a true, on-demand or heralded, single-photon generator. In this thesis we demonstrated the realization of uncorrelated photon twins in optical fibres; spatial entanglement was avoided by the characteristics of the guided modes in fibres, and the spectral correlations were eliminated by the choice of the pump and fibre length, utilizing the dispersion of the fibre. We proved the low degree of spatial-temporal entanglement within the created photon-pair by a HOM-type interference experiment, which exhibited high purity of the heralded photons, with no spectral filters.

Since the first demonstration of a factorable photon-pair state generated in a

KDP crystal [93], the idea to employ GV-matching conditions to produce pure heralded photons has attracted a significant attention. While the results with bulk KDP exhibit a remarkably high purity, about 95%, spatial filtering is required to remove spatial correlations. Additionally, it is difficult to efficiently collect the photons produced in bulk crystals. Therefore, efforts have been focused on the production of uncorrelated photon-pairs in waveguides, where the support of only a single spatial mode eliminates the correlations within this degree of freedom. Experimental demonstrations of factorable photon-pair sources have been carried out with PCFs: in this thesis we report an achieved purity of $p \approx 86\%$ with a birefringent PCF [126]. Halder *et al.* reported $p \approx 76\%$ obtained by independent efforts [127], and Söller *et al.* demonstrated the generation of up to 82% decorrelated photon-pairs, with one at the telecom wavelength and the sibling at the visible bandwidth [123]. The current efforts with standard silica birefringent fibres, which take place at the Max Planck Institute for the Science of Light in Erlangen (with our collaboration), have so far yielded purity of at least 70%.

8.1 Outlook

8.1.1 Improving the source

While this thesis demonstrates the high potential and ability to tailor the joint spectrum of generated photon-pairs in waveguides, our PCF source posses several flaws: Raman contamination is still high, forcing us to use low enough pump power – and

thus low generation rate – in order to reduce its effect to negligible levels. Moreover, spatial differences between the PCF mode and the standard single-mode fibers degrade the coupling efficiency of the heralded photons to a fibre-network. We're therefore currently making efforts to extend the implementation of the technique to standard highly birefringent fibres: the large birefringence shifts the signal-idler pair farther from the pump to a detuning where this Raman contribution is insignificant. The usage of standard fibre sources supports high spatial mode overlap with the guided modes in optical fibre networks.

Another drawback of our experimental setup stems from chromatic aberrations in the microscope objectives used to couple in and out of the PCF in the Sagnac-loop configuration (see Figure 5.2). As a result of this, the counter propagating SFWM gain exit the interferometer with incomplete spatial overlap, and therefore it's impossible to optimize the coupling of the idler beam into a single-mode fibre for both polarizations simultaneously. If one wishes to use the full power of the generation technique, in terms of collection efficiency, it's better to spatially separate the two polarizations and couple them into a single-mode fibre independently. This lesson is being implemented in the new setup for standard fibres (see Figure (7.5)).

8.1.2 Other media – planar waveguides

Another interesting technique to implement optical networks is on a chip waveguide[30,131–133], a technology that allows the implementation of many small and stable interferometers. An obvious advantage in miniaturizing quantum-circuits is for

practical purposes. However, another gain obtained by the small scale of the circuits is in avoiding temperature and stress variations, which alter the refractive index locally. Thence, small networks tend to be more phase stable, which is a crucial feature required by any quantum-optical circuit. Again, in order to ensure good coupling of photons to such a network, it would be advantageous to generate the photons in similar waveguides.

Planar waveguides are usually made of three layers of materials with low optical loss. Normally, the two outer layers are identical, while the middle one is doped with UV sensitive atoms, and its refractive index may be higher than the outer layers. For example, common waveguides consist of pure silica outer slabs and germanium doped silica as the middle slab. The refractive index of germanium, being photosensitive, increases when exposed to UV light. Consequently, focused UV beam onto the doped layer writes the waveguide. As a result, just like silica fibres, the dispersion of this type of waveguides can be accurately modeled as of pure silica. Moreover, they may posses high birefringence due to the asymmetry in the geometry. A sketch of such a planar waveguide is shown in Figure 8.1.

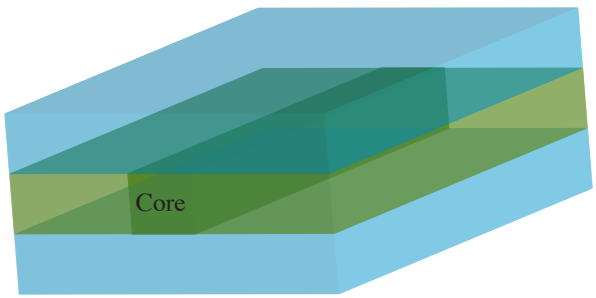


Figure 8.1 General schematic of a planar waveguide. The light is confined in the rectangular core which has the highest refractive index. The asymmetry of the configuration gives rise to birefringence.

8.1.3 Beyond the single photon

The FWM interaction may produce more than one pair of photons. The contribution to the generation of several photon-pairs is given by higher order expansion in the perturbation theory. Generally, the interaction *squeezes* the signal-idler modes; in the following we explain briefly the squeezing operation. The *squeezing operator*, or *squeezer*, is given by

$$S_{1mode}(\xi) = \exp\left[\xi {a^\dagger}^2 + \xi^* a^2\right] \ , \tag{8.1}$$

where ξ is the *squeezing parameter* and a is the annihilation operator. The above squeezing operator is the single-mode squeezer. If it acts on the vacuum, the resultant state, called *vacuum squeezed state*, is a superposition of even-number of photonic Fock-states.

The 2-mode squeezer is defined as:

$$S_{2modes}(\xi) = \exp\left[\xi a_s^\dagger a_i^\dagger + \xi^* a_s a_i\right] \ , \tag{8.2}$$

where a_s and a_i are the annihilation operators of two different (orthogonal) modes. Acting on the vacuum, it again generates photons in pairs, with equal number of signal (s) and idler (i) photons.

In the most general form, the multimode squeezer is

$$S = \exp\left[\int \left(\xi(\omega_s,\omega_i) a_s^\dagger(\omega_s) a_i^\dagger(\omega_i) + \xi^*(\omega_s,\omega_i) a_s(\omega_s) a_i(\omega_i)\right) d\omega_s d\omega_i\right] \ , \tag{8.3}$$

where we consider continuous modes labeled by ω_s and ω_i, e.g. light frequencies, which we assume here. The squeezing parameter $\xi(\omega_s, \omega_i)$ depends now on the joint spectrum. The Schmidt decomposition theorem guarantees that we can write this operator in the form

$$S = \exp\left[\sum_n \zeta_n \left(a_{s,n} a_{i,n} + a_{s,n}^\dagger a_{i,n}^\dagger\right)\right] , \tag{8.4}$$

where $\{\zeta_n\}$ are the Schmidt coefficients (hence real) and $a_{\mu,n}$ ($\mu = s, i$) is the annihilation operator associated with mode n. The orthogonality of the Schmidt modes implies the commutation relations

$$\left[a_{\mu,m}, a_{\mu,n}^\dagger\right] = \delta_{m,n} . \tag{8.5}$$

Thus, the multimode squeezing operator can be written as:

$$S = \prod_n \exp\left[\zeta_n \left(a_{s,n}^\dagger a_{i,n}^\dagger + a_{s,n} a_{i,n}\right)\right] . \tag{8.6}$$

Hence, any multimode squeezer can be decomposed into a set of 2-mode squeezing operators acting independently with their own squeezing parameter (ζ_n).

Acting with the multimode squeezer on the vacuum and filtering a particular Schmidt mode is equivalent to applying a 2-mode squeezing operator. Unfortunately, spectral filters can only block or attenuate specific wavelengths in a phase-insesitive way, while the Schmidt wave-packets are generally a superposition of frequency

modes with various phases, hence requiring a phase-sensitive filter to distinguish between them – a technology that does not exist to date.

The scattering operator Eq. (2.24) with Hamiltonian (2.29) is a multimode squeezer[134]. The time ordering in Eq. (2.24) prohibits us from first integrating over time and then expanding the exponent. Rather, since the Hamiltonian does not generally commute with itself at different times, each term in the perturbation needs to be ordered and integrated accordingly. The origin of this difficulty arises from the fact that although energy conservation has to be maintained at the end of the process, it can be violated for short times during the interaction (time-energy uncertainty): a pair of signal-idler with arbitrary frequencies can be created from two pump photons even if it violates the conservation of energy, provided this pair is annihilated shortly afterwards. Thus, in essence, the FWM need not conserve energy at the interaction instance. However, annihilating a just-created pair is a higher-order interaction term. In the perturbative regime, the contribution of every ascending order is only a small correction and occurs with low probability during the *whole* interaction. Hence, the case in which two interactions take place within a short time interval between them is highly unlikely to occur, leading us to assume the conservation of energy at each instance[98]. This approach, called the *rotating-wave approximation*, in essence means neglecting the time dependency in the interaction Hamiltonian (only terms with $\omega_{p1}+\omega_{p2}-\omega_s-\omega_i=0$ are considered), and the integration over time in Eq. (2.24) can be carried before the expansion of the exponent.

We conclude, then, that for the signal and idler modes, the FWM interaction acts as the squeezer

$$S = \mathbb{S}(+\infty, -\infty) = \exp\left[\xi \int d\omega_s d\omega_i f(\omega_s, \omega_i) a_s^\dagger(\omega_s) a_i^\dagger(\omega_i) + h.c.\right] , \tag{8.7}$$

where the typical squeezing parameter ξ depends, among others, on the pump power, fibre length and pump bandwidth, $f(\omega_s, \omega_i)$ is the joint spectral amplitude given by Eq. (2.38) which was developed for the one-pair generation. This is very convenient, as it means that the technique developed in this thesis to factorize the photon-pair state generated in SFWM actually creates a true 2-mode squeezer. We can increase the squeezing, and hence the probability to generate higher photon number states, by raising the pump power, without affecting the spectral properties of the squeezed modes. Such a source, then, opens the door to many more experiments and applications requiring 2-mode squeezed (vacuum) states, such as the generation of *heralded polarization-entangled photons* [135], *heralded NOON states* with $N > 2$ [136,137], and *continuous-variable entanglement-distillation* [138–140]. Here, one can see probably the most significant advantage of our factorizing scheme over the traditional spectral filtering method used to project the photons onto a pure mode: while the heralding efficiency does not degrade by spectrally filtering the heralding arm, the resulting state is not the squeezed vacuum, as the photon number correlations between the signal and idler ports is severely damaged by the rejection of many (typically most of the) photons at the filtered arm.

8.2 Comparing SFWM with SPDC

The main workhorse for generating pairs of photons has been so far the process of SPDC in bulk crystals. The second order susceptibility in nonlinear crystals is a lot more efficient than glass's third order susceptibility in mediating a nonlinear interaction. Nonetheless, when the latter is incorporated into a long propagation distance of interaction, in a guiding configuration, it can give rise to stronger nonlinear effects. Indeed, the generation rate of photon-pairs per pump power in PCFs is immensely higher than in bulk crystals.

Fibres can be manufactured with various dispersion properties and birefringence, and thus can be engineered to control the phase-matching wavelengths as well as the joint spectral characteristics. Crystals, on the other hand, are created by nature, hence cannot be manipulated to modify their dispersion properties, and one can only choose between the various existing crystals. Indeed, in Reference [93], which was the first to demonstrate photon-pairs production with factorable joint amplitude, the chosen crystal was KDP due to its dispersion curve and birefringence, although its nonlinearity is a lot weaker than highly nonlinear crystals such as BBO.

Another advantage in the generation in fibres is the specific spatial mode in which photons are created, avoiding any spatial correlations, while the photon-pair generated in bulk crystals do posses such correlations.

However, the $\chi^{(2)}$ interaction can be incorporated into a waveguide configuration, which extends the length of the interaction and confines the generation into a single spatial mode [141]. Moreover, this interaction has a freedom which is absent in the $\chi^{(3)}$

– *quasi phase-matching*[142,143]: since the three-wave mixing relies on the asymmetry of the medium to inversion, periodically poling the crystal implements a periodic sign flip of the susceptibility. The periodicity acts as an additional argument in the phase-mismatch, and engineering it manipulates the phase-matching wavelengths. It has been pointed out that periodically poled crystals in a waveguide configuration can produce photon-pairs where one of the photons is scattered in the backward direction[144]. This regime has been shown[145] to generate photons with highly factorable joint amplitude: the GV of the forward-scattered photon is very close to the pump respective to the huge GV mismatch with the backward-scattered photon (GVs with opposite signs), hence the phase-matching function is almost horizontal (or vertical, depending on the definitions). This type of interaction, which can conserve momentum thanks to the nonuniformity of the interaction (the periodic poling), is not strictly applicable to FWM as it symmetric under inversion. It has been demonstrated, however, that a periodically varying refractive index could manipulate the phase-matching solutions of FWM[146] in a way resembling the $\chi^{(2)}$ quasi phase-matching. Note that a scheme to generate factorable photon-pair states using quasi phase-matching requires a precise and uniform periodicity of the poling to avoid variations of the phase-matching wavelengths along the waveguide. Recent efforts have shown[147] that a factorable photon-pair state can be produced at the telecom wavelengths in waveguides without the requirement for the periodic poling.

8.3 Conclusions

In Chapter 1 we reviewed briefly some historical key advances in the field of quantum optics. We outlined some differences between the classical and quantum mechanical descriptions of light and experimental tests that distinguish the two theories, as well as the application of quantum mechanics to linear-optics quantum-computation. The importance of a single-photon generator was explained, and the various techniques to implement such a generator were reviewed. We described the alternative approach, which is the most commonly used to date: the heralded photon through SPDC or SFWM. The significance of pure photons, and hence the factorable photon-pair state, were explained.

Chapter 2 reviewed the SFWM interaction in fibres. The correlations in the photon-pairs generated via this process were outlined, and we showed the massive loss introduced by spectral filtering in attempt to remove these correlations.

In Chapter 3 we presented the theoretical study towards tailoring the joint spectral correlations between the photons generated through SFWM in fibres. We showed that by making use of fibre birefringence, factorable photon-pair state can be produced in PCFs within the detection bandwidth utilizing experimentally available resources.

The experimental tests of various PCFs by measuring the phase-matching curve were reviewed in Chapter 4. A suitable PCF with correct characteristics was identified and modelled by a birefringent version of the step-index model, to provide us with the approximate required pump bandwidth for the given PCF length.

The purity of the heralded photons was demonstrated by means of HOM interference in Chapter 5. The high interference visibility illustrates the strength of our scheme in realizing a source of uncorrelated photon-pairs.

Chapter 6 investigated theoretically and experimentally numerous conditions that can affect the two photon interference visibility. While we found that longer fibre has greater potential to produce pure heralded photons, theoretical study emphasized the importance of uniformity in the PCFs, a characteristic that to date is not studied or addressed by manufacturers [128].

The current efforts made to extend the application of the technique to birefringent standard fibres are presented in Chapter 7. It was shown that a useful photonic source could be realized with standard birefringent fibres – a promising resource for the generation of single photons for integrated photonic circuits. The developed standard fibre industry may find a way to solve the uniformity problem existing in PCFs.

Finally, in this Chapter, we summarized, concluded, and proposed future work, including the use of a factorable photon-pair source, such as the one we demonstrated in this thesis, for the application in many experiments with high number of photons.

Appendix A

The polarization HOM interference

In this appendix we derive the probability of the 4-fold coincidence for the HOM-setup, Figure 5.2, assuming the absence of losses. In such a case, a detection registered at $\mathrm{APD_A}$ and $\mathrm{APD_C}$ heralds two orthogonal linearly polarized photons. Let's denote their density matrices as ρ_H and ρ_V for the horizontally and vertically polarized photons, respectively. These matrices can be expressed in the diagonal basis as:

$$\begin{aligned} \rho_H &= \sum_n s_n |\psi_n\rangle\langle\psi_n| \,, \\ \rho_V &= \sum_m t_m |\phi_m\rangle\langle\phi_m| \,, \end{aligned} \tag{A.1}$$

where s_n and t_m are nonnegative numbers obeying the normalization $\sum_{n=1}^{\infty} s_n = \sum_{m=1}^{\infty} t_m = 1$, $\{|\psi_n\rangle\}$ and $\{|\phi_m\rangle\}$ are two orthogonal sets of spatial-temporal photonic wavefunctions. We can associate with them annihilation operators $a_{n\mu}$ and

$b_{m\mu}$ where $\mu = H, V$ specifies the polarization of the photon. Thus,

$$\begin{aligned} \langle\psi_n|\psi_k\rangle = \langle 0|a_{nH}a^\dagger_{kH}|0\rangle = \langle 0|a_{nV}a^\dagger_{kV}|0\rangle &= \delta_{n,k}\,, \\ \langle\phi_n|\phi_k\rangle = \langle 0|b_{nH}b^\dagger_{kH}|0\rangle = \langle 0|b_{nV}b^\dagger_{kV}|0\rangle &= \delta_{n,k}\,, \\ \langle\psi_n|\phi_k\rangle = \langle 0|a_{nH}b^\dagger_{kH}|0\rangle = \langle 0|a_{nV}b^\dagger_{kV}|0\rangle &\quad . \end{aligned} \tag{A.2}$$

The two-photon density matrix is:

$$\rho = \sum_{m\,n} s_n t_m a^\dagger_{nH} b^\dagger_{mV}|0\rangle\langle 0|a_{nH}b_{mV}\,. \tag{A.3}$$

After the idler photons travel through SMF in Figure 5.2 followed by QWP, their polarization experience a unitary transformation, leaving them in an elliptical polarization, but yet still orthogonal to each other. This transformation can be written as:

$$\begin{aligned} a_{nH} &\rightarrow \cos(\eta)a_{nH} + i\sin(\eta)a_{nV}\,, \\ b_{mV} &\rightarrow i\sin(\eta)b_{mH} + \cos(\eta)b_{mV}\,, \end{aligned} \tag{A.4}$$

where $\tan\eta$ is the ratio between the amplitudes of the principal axes of the ellipse. The above transformation is correct up to an overall rotation, and HWP4 is used to rotate the state to any desired angle θ. This transformation is given by:

$$\begin{aligned} a_{nH} &\rightarrow \cos(\theta)a_{nH} + \sin(\theta)a_{nV}\,, \\ a_{nV} &\rightarrow -\sin(\theta)a_{nH} + \cos(\theta)a_{nV}\,, \\ b_{mH} &\rightarrow \cos(\theta)b_{mH} + \sin(\theta)b_{mV}\,, \\ b_{mV} &\rightarrow -\sin(\theta)b_{mH} + \cos(\theta)b_{mV}\,. \end{aligned} \tag{A.5}$$

Thus, taking into account the ellipticity of the photons' polarization and after a rotation to an angle θ, the two-photon state is:

$$\begin{aligned}
\rho(\theta) \;=\; & \\
& \textstyle\sum_{m\,n} s_n t_m \times \\
& \Big[(\cos\eta\cos\theta + i\sin\eta\sin\theta)a^\dagger_{nH} + (\cos\eta\sin\theta - i\sin\eta\cos\theta)a^\dagger_{nV}\Big] \times \\
& \Big[-(\cos\eta\sin\theta + i\sin\eta\cos\theta)b^\dagger_{mH} + (\cos\eta\cos\theta - i\sin\eta\sin\theta)b^\dagger_{mV}\Big] \times \\
& |0\rangle\langle 0| \times \\
& [(\cos\eta\cos\theta - i\sin\eta\sin\theta)a_{nH} + (\cos\eta\sin\theta + i\sin\eta\cos\theta)a_{nV}] \times \\
& [-(\cos\eta\sin\theta - i\sin\eta\cos\theta)b_{mH} + (\cos\eta\cos\theta + i\sin\eta\sin\theta)b_{mV}] \;.
\end{aligned} \tag{A.6}$$

The probability $P_4(\theta)$ of having one photon in the H polarization and the other in V, given the state $\rho(\theta)$, is (in the absence of losses):

$$P_4(\theta) = \sum_{l\,k} \langle 0|a_{lH}a_{kV}\rho(\theta)a^\dagger_{lH}a^\dagger_{kV}|0\rangle \;, \tag{A.7}$$

where we used the completeness of the photonic space created by the $a^\dagger_{n\mu}$ operators. Thus

$$P_4(\theta) = |A(\eta,\theta)\langle\psi_l|\psi_n\rangle\langle\psi_k|\phi_m\rangle - B(\eta,\theta)\langle\psi_k|\psi_n\rangle\langle\psi_l|\phi_m\rangle|^2 \;, \tag{A.8}$$

where

$$\begin{aligned}
A(\eta,\theta) &= \left(\cos^2\eta\cos^2\theta + \sin^2\eta\sin^2\theta\right) \;, \\
B(\eta,\theta) &= \left(\cos^2\eta\sin^2\theta + \sin^2\eta\cos^2\theta\right) \;.
\end{aligned} \tag{A.9}$$

Expanding the above expression, using some laborious but straightforward alge-

bra with trigonometric identities, one finds

$$\begin{aligned} P_4(\theta) &= \textstyle\sum_{l\,k\,m\,n} s_n t_m \Big\{ \\ &\quad A^2(\eta,\theta)\langle\psi_l|\psi_n\rangle\langle\psi_k|\phi_m\rangle\langle\phi_m|\psi_k\rangle\langle\psi_n|\psi_l\rangle + \\ &\quad B^2(\eta,\theta)\langle\psi_k|\psi_n\rangle\langle\psi_l|\phi_m\rangle\langle\phi_m|\psi_l\rangle\langle\psi_n|\psi_k\rangle - \\ &\quad A(\eta,\theta)B(\eta,\theta)\left[\langle\psi_l|\psi_n\rangle\langle\psi_k|\phi_m\rangle\langle\phi_m|\psi_l\rangle\langle\psi_n|\psi_k\rangle + c.c.\right] \Big\} \\ &= \left(A^2(\eta,\theta) + B^2(\eta,\theta)\right) Tr(\rho_H)Tr(\rho_V) - \\ &\quad 2A(\eta,\theta)B(\eta,\theta)Tr(\rho_H\rho_V) \\ &= \tfrac{1}{2}\left(1+\cos^2\eta\cos^2\theta\right) - p\tfrac{1}{2}\left(1-\cos^2\eta\cos^2\theta\right) , \end{aligned} \tag{A.10}$$

where *c.c.* stands for complex-conjugate, $p = Tr(\rho_H\rho_V)$ and we used $Tr(\rho_H) = Tr(\rho_V) = 1$. Rearranging terms in the above equation, we finally arrive at Eq. (5.9):

$$P_4(\theta) = \frac{1}{2}\left[(1-p) + (1+p)\cos^2(2\eta)\cos^2(2\theta)\right] . \tag{A.11}$$

Bibliography

[1] M. Planck, *On the Law of Distribution of Energy in the Normal Spectrum*, Annalen der Physik, **4**, p. 553 (1901).

[2] A. Einstein, *Über einen die Erzeugung und Verwandlung des Lichtes betreffenden heuristischen Gesichtspunkt*, Annalen der Physik, **17**, pp. 132–148 (1905).

[3] E. Schrödinger, *An Undulatory Theory of the Mechanics of Atoms and Molecules*, Physical Review, **28**, p. 1049 (1926).

[4] H. J. Kimble, M. Dagenais, and L. Mandel, *Photon Antibunching in Resonance Fluorescence*, Physical Review Letters, **39**, pp. 691–695 (1977).

[5] R. Loudon, *The Quantum Theory of Light*, Oxford University Press, 3rd. edition (2000).

[6] C. K. Hong, Z. Y. Ou, and L. Mandel, *Measurement of subpicosecond time intervals between two photons by interference*, Physical Review Letters, **59**, pp. 2044–2046 (1987).

[7] D. Deutsch, *Quantum theory, the Church-Turing principle and the universal quantum computer*, Royal Society of London Proceedings Series A, **400**, pp. 97–117 (1985).

[8] P. M. Shor, *Algorithms for quantum computation: discrete logarithms and factoring*, in *35th Annual Symposium on Foundations of Computer Science*, pp. 124–134 (1994).

[9] G. J. Milburn, *Quantum optical Fredkin gate*, Physical Review Letters, **62**, pp. 2124–2127 (1989).

[10] E. Knill, R. Laflamme, and G. J. Milburn, *A scheme for efficient quantum computation with linear optics*, Nature, **409**, pp. 46–52 (2001).

[11] T. C. Ralph, A. G. White, W. J. Munro, and G. J. Milburn, *Simple scheme for efficient linear optics quantum gates*, Physical Review A, **65**, 012314 (2001).

[12] T. C. Ralph, N. K. Langford, T. B. Bell, and A. G. White, *Linear optical controlled-NOT gate in the coincidence basis*, Physical Review A, **65**, 062324 (2002).

[13] X. Zou, K. Pahlke, and W. Mathis, *Teleportation implementation of nondeterministic quantum logic operations by using linear optical elements*, Physical Review A, **65**, 064305 (2002).

[14] H. F. Hofmann and S. Takeuchi, *Quantum phase gate for photonic qubits using only beam splitters and postselection*, Physical Review A, **66**, 024308 (2002).

[15] R. Raussendorf and H. J. Briegel, *A One-Way Quantum Computer*, Physical Review Letters, **86**, pp. 5188–5191 (2001).

[16] N. Yoran and B. Reznik, *Deterministic Linear Optics Quantum Computation with Single Photon Qubits*, Physical Review Letters, **91**, 037903 (2003).

[17] M. A. Nielsen, *Optical Quantum Computation Using Cluster States*, Physical Review Letters, **93**, 040503 (2004).

[18] D. E. Browne and T. Rudolph, *Resource-Efficient Linear Optical Quantum Computation*, Physical Review Letters, **95**, 010501 (2005).

[19] A. J. F. Hayes, A. Gilchrist, C. R. Myers, and T. C. Ralph, *Utilizing encoding in scalable linear optics quantum computing*, Journal of Optics B: Quantum and Semiclassical Optics, **6**, pp. 533–541 (2004).

[20] A. Gilchrist, A. J. F. Hayes, and T. C. Ralph, *Efficient parity-encoded optical quantum computing*, Physical Review A, **75**, 052328 (2007).

[21] T. B. Pittman, B. C. Jacobs, and J. D. Franson, *Demonstration of Nondeterministic Quantum Logic Operations Using Linear Optical Elements*, Physical Review Letters, **88** (2002).

[22] K. J. Resch, J. S. Lundeen, and A. M. Steinberg, *Conditional-Phase Switch at the Single-Photon Level*, Physical Review Letters, **89**, 037904 (2002).

[23] T. B. Pittman, M. J. Fitch, B. C. Jacobs, and J. D. Franson, *Experimental controlled-NOT logic gate for single photons in the coincidence basis*, Physical Review A, **68**, 032316 (2003).

[24] J. L. O'Brien, G. J. Pryde, A. G. White, T. C. Ralph, and D. Branning, *Demonstration of an all-optical quantum controlled-NOT gate*, Nature, **426**, pp. 264–267 (2003).

[25] S. Gasparoni, J.-W. Pan, P. Walther, T. Rudolph, and A. Zeilinger, *Realization of a Photonic Controlled-NOT Gate Sufficient for Quantum Computation*, Physical Review Letters, **93**, 020504 (2004).

[26] Z. Zhao, A.-N. Zhang, Y.-A. Chen, H. Zhang, J.-F. Du, T. Yang, and J.-W. Pan, *Experimental Demonstration of a Nondestructive Controlled-NOT Quantum Gate for Two Independent Photon Qubits*, Physical Review Letters, **94**, 030501 (2005).

[27] P. Walther, K. J. Resch, T. Rudolph, E. Schenck, H. Weinfurter, V. Vedral, M. Aspelmeyer, and A. Zeilinger, *Experimental one-way quantum computing*, Nature, **434**, pp. 169–176 (2005).

[28] R. Prevedel, P. Walther, F. Tiefenbacher, P. Bohi, R. Kaltenbaek, T. Jennewein, and A. Zeilinger, *High-speed linear optics quantum computing using active feed-forward*, Nature, **445**, pp. 65–69 (2007).

[29] J. Chen, J. B. Altepeter, M. Medic, K. F. Lee, B. Gokden, R. H. Hadfield, S. W. Nam, and P. Kumar, *Demonstration of a Quantum Controlled-NOT Gate in the Telecommunications Band*, Physical Review Letters, **100**, pp. 133603–4 (2008).

[30] A. Politi, M. J. Cryan, J. G. Rarity, S. Yu, and J. L. O'Brien, *Silica-on-Silicon Waveguide Quantum Circuits*, Science, **320**, pp. 646–649 (2008).

[31] A. Cernoch, J. Soubusta, L. Bartuskova, M. Dusek, and J. Fiurasek, *Experimental Realization of Linear-Optical Partial swap Gates*, Physical Review Letters, **100**, pp. 180501–4 (2008).

[32] P. Kok, W. J. Munro, K. Nemoto, T. C. Ralph, J. P. Dowling, and G. J. Milburn, *Linear optical quantum computing with photonic qubits*, Reviews of Modern Physics, **79**, pp. 135–40 (2007).

[33] B. Julsgaard, J. Sherson, J. I. Cirac, J. Fiurasek, and E. S. Polzik, *Experimental demonstration of quantum memory for light*, Nature, **432**, pp. 482–486 (2004).

[34] C. W. Chou, H. de Riedmatten, D. Felinto, S. V. Polyakov, S. J. van Enk, and H. J. Kimble, *Measurement-induced entanglement for excitation stored in remote atomic ensembles*, Nature, **438**, pp. 828–832 (2005).

[35] T. Chaneliere, D. N. Matsukevich, S. D. Jenkins, S. Y. Lan, T. A. B. Kennedy, and A. Kuzmich, *Storage and retrieval of single photons transmitted between remote quantum memories*, Nature, **438**, pp. 833–836 (2005).

[36] C. A. Muschik, K. Hammerer, E. S. Polzik, and J. I. Cirac, *Efficient quantum memory and entanglement between light and an atomic ensemble using magnetic fields*, Physical Review A (Atomic, Molecular, and Optical Physics), **73**, pp. 062329–14 (2006).

[37] J. Sherson, A. S. Sorensen, J. Fiurasek, K. Mølmer, and E. S. Polzik, *Light qubit storage and retrieval using macroscopic atomic ensembles*, Physical Review A (Atomic, Molecular, and Optical Physics), **74**, pp. 011802–4 (2006).

[38] P. M. Leung and T. C. Ralph, *Quantum memory scheme based on optical fibers and cavities*, Physical Review A (Atomic, Molecular, and Optical Physics), **74**, pp. 022311–6 (2006).

[39] T. Opatrný, *Single-cell atomic quantum memory for light*, Physical Review A (Atomic, Molecular, and Optical Physics), **74**, pp. 043809–5 (2006).

[40] K. Honda, D. Akamatsu, M. Arikawa, Y. Yokoi, K. Akiba, S. Nagatsuka, T. Tanimura, A. Furusawa, and M. Kozuma, *Storage and Retrieval of a Squeezed Vacuum*, Physical Review Letters, **100**, pp. 093601–4 (2008).

[41] J. J. L. Morton, A. M. Tyryshkin, R. M. Brown, S. Shankar, B. W. Lovett, A. Ardavan, T. Schenkel, E. E. Haller, J. W. Ager, and S. A. Lyon, *Solid-state quantum memory using the* ^{31}P *nuclear spin*, Nature, **455**, pp. 1085–1088 (2008).

[42] J. Nunn, K. Reim, K. C. Lee, V. O. Lorenz, B. J. Sussman, I. A. Walmsley, and D. Jaksch, *Multimode Memories in Atomic Ensembles*, Physical Review Letters, **101**, pp. 260502–4 (2008).

[43] B. Zhao, Y.-A. Chen, X.-H. Bao, T. Strassel, C.-S. Chuu, X.-M. Jin, J. Schmiedmayer, Z.-S. Yuan, S. Chen, and J.-W. Pan, *A millisecond quantum memory for scalable quantum networks*, Nat Phys, **5**, pp. 95–99 (2009).

[44] R. Zhao, Y. O. Dudin, S. D. Jenkins, C. J. Campbell, D. N. Matsukevich, T. A. B. Kennedy, and A. Kuzmich, *Long-lived quantum memory*, Nat Phys, **5**, pp. 100–104 (2009).

[45] M. Afzelius, C. Simon, H. de Riedmatten, and N. Gisin, *Multimode quantum memory based on atomic frequency combs*, Physical Review A (Atomic, Molecular, and Optical Physics), **79**, pp. 052329–9 (2009).

[46] C.-H. Yuan, L.-Q. Chen, and W. Zhang, *Storage of polarization-encoded cluster states in an atomic system*, Physical Review A (Atomic, Molecular, and Optical Physics), **79**, pp. 052342–7 (2009).

[47] K. F. Reim, J. Nunn, V. O. Lorenz, B. J. Sussman, K. C. Lee, N. K. Langford, D. Jaksch, and I. A. Walmsley, *Towards high-speed optical quantum memories*, Nat Photon, **4**, pp. 218–221 (2010).

[48] S. Takeuchi, J. Kim, Y. Yamamoto, and H. H. Hogue, *Development of a high-quantum-efficiency single-photon counting system*, Applied Physics Letters, **74**, pp. 1063–1065 (1999).

[49] D. Achilles, C. Silberhorn, C. Śliwa, K. Banaszek, and I. A. Walmsley, *Fiber-assisted detection with photon number resolution*, Opt. Lett., **28**, pp. 2387–2389 (2003).

[50] M. J. Fitch, B. C. Jacobs, T. B. Pittman, and J. D. Franson, *Photon-number resolution using time-multiplexed single-photon detectors*, Physical Review A, **68**, 043814 (2003).

[51] E. Waks, K. Inoue, W. D. Oliver, E. Diamanti, and Y. Yamamoto, *High-efficiency photon-number detection for quantum information processing*, Selected Topics in Quantum Electronics, IEEE Journal of, **9**, pp. 1502–1511 (2003).

[52] D. Rosenberg, A. E. Lita, A. J. Miller, and S. W. Nam, *Noise-free high-efficiency photon-number-resolving detectors*, Physical Review A, **71**, 061803 (2005).

[53] B. Lounis and M. Orrit, *Single-photon sources*, Reports on Progress in Physics, **68**, pp. 1129–1179 (2005).

[54] A. Kuhn, M. Hennrich, and G. Rempe, *Deterministic Single-Photon Source for Distributed Quantum Networking*, Physical Review Letters, **89**, 067901 (2002).

[55] J. McKeever, A. Boca, A. D. Boozer, R. Miller, J. R. Buck, A. Kuzmich, and H. J. Kimble, *Deterministic Generation of Single Photons from One Atom Trapped in a Cavity*, Science, **303**, pp. 1992–1994 (2004).

[56] B. Darquié, M. P. A. Jones, J. Dingjan, J. Beugnon, S. Bergamini, Y. Sortais, G. Messin, A. Browaeys, and P. Grangier, *Controlled Single-Photon Emission from a Single Trapped Two-Level Atom*, Science, **309**, pp. 454–456 (2005).

[57] M. Hijlkema, B. Weber, H. P. Specht, S. C. Webster, A. Kuhn, and G. Rempe, *A single-photon server with just one atom*, Nat Phys, **3**, pp. 253–255 (2007).

[58] M. Keller, B. Lange, K. Hayasaka, W. Lange, and H. Walther, *Continuous generation of single photons with controlled waveform in an ion-trap cavity system*, Nature, **431**, pp. 1075–1078 (2004).

[59] P. Maunz, D. L. Moehring, S. Olmschenk, K. C. Younge, D. N. Matsukevich, and C. Monroe, *Quantum interference of photon pairs from two remote trapped atomic ions*, Nat Phys, **3**, pp. 538–541 (2007).

[60] T. BaschÈ, W. E. Moerner, M. Orrit, and H. Talon, *Photon antibunching in the fluorescence of a single dye molecule trapped in a solid*, Physical Review Letters, **69**, pp. 1516–1519 (1992).

[61] C. Brunel, B. Lounis, P. Tamarat, and M. Orrit, *Triggered Source of Single Photons based on Controlled Single Molecule Fluorescence*, Physical Review Letters, **83**, pp. 2722–2725 (1999).

[62] W. Patrick Ambrose, P. M. Goodwin, J. Enderlein, D. J. Semin, J. C. Martin, and R. A. Keller, *Fluorescence photon antibunching from single molecules on a surface*, Chemical Physics Letters, **269**, pp. 365–370 (1997).

[63] L. Fleury, J. M. Segura, G. Zumofen, B. Hecht, and U. P. Wild, *Nonclassical Photon Statistics in Single-Molecule Fluorescence at Room Temperature*, Physical Review Letters, **84**, pp. 1148–1151 (2000).

[64] B. Lounis and W. E. Moerner, *Single photons on demand from a single molecule at room temperature*, Nature, **407**, pp. 491–493 (2000).

[65] T.-H. Lee, P. Kumar, A. Mehta, K. Xu, R. M. Dickson, and M. D. Barnes, *Oriented semiconducting polymer nanostructures as on-demand room-temperature single-photon sources*, Applied Physics Letters, **85**, pp. 100–102 (2004).

[66] C. Kurtsiefer, S. Mayer, P. Zarda, and H. Weinfurter, *Stable Solid-State Source of Single Photons*, Physical Review Letters, **85**, pp. 290–293 (2000).

[67] A. Beveratos, R. Brouri, T. Gacoin, A. Villing, J.-P. Poizat, and P. Grangier, *Single Photon Quantum Cryptography*, Physical Review Letters, **89**, 187901 (2002).

[68] T. Gaebel, I. Popa, A. Gruber, M. Domhan, F. Jelezko, and J. Wrachtrup, *Stable single-photon source in the near infrared*, New Journal of Physics, **6**, pp. 98–98 (2004).

[69] B. Lounis, H. A. Bechtel, D. Gerion, P. Alivisatos, and W. E. Moerner, *Photon antibunching in single CdSe/ZnS quantum dot fluorescence*, Chemical Physics Letters, **329**, pp. 399–404 (2000).

[70] P. Michler, A. Kiraz, C. Becher, W. V. Schoenfeld, P. M. Petroff, L. Zhang, E. Hu, and A. Imamoglu, *A Quantum Dot Single-Photon Turnstile Device*, Science, **290**, pp. 2282–2285 (2000).

[71] G. Messin, J. P. Hermier, E. Giacobino, P. Desbiolles, and M. Dahan, *Bunching and antibunching in the fluorescence of semiconductor nanocrystals*, Opt. Lett., **26**, pp. 1891–1893 (2001).

[72] P. Michler, A. Imamoglu, M. D. Mason, P. J. Carson, G. F. Strouse, and S. K. Buratto, *Quantum correlation among photons from a single quantum dot at room temperature*, Nature, **406**, pp. 968–970 (2000).

[73] R. M. Thompson, R. M. Stevenson, A. J. Shields, I. Farrer, C. J. Lobo, D. A. Ritchie, M. L. Leadbeater, and M. Pepper, *Single-photon emission from exciton complexes in individual quantum dots*, Physical Review B, **64**, 201302(R) (2001).

[74] Z. Yuan, B. E. Kardynal, R. M. Stevenson, A. J. Shields, C. J. Lobo, K. Cooper, N. S. Beattie, D. A. Ritchie, and M. Pepper, *Electrically Driven Single-Photon Source*, Science, **295**, pp. 102–105 (2002).

[75] C. Santori, D. Fattal, J. Vučković, G. S. Solomon, and Y. Yamamoto, *Indistinguishable photons from a single-photon device*, Nature, **419**, pp. 594–597 (2002).

[76] V. Zwiller, P. Jonsson, H. Blom, S. Jeppesen, M.-E. Pistol, L. Samuelson, A. A. Katznelson, E. Y. Kotelnikov, V. Evtikhiev, and G. Bjrk, *Correlation spectroscopy of excitons and biexcitons on a single quantum dot*, Physical Review A, **66**, 053814 (2002).

[77] E. B. Flagg, A. Muller, S. V. Polyakov, A. Ling, A. Migdall, and G. S. Solomon, *Interference of Single Photons from Two Separate Semiconductor Quantum Dots*, Physical Review Letters, **104**, 137401 (2010).

[78] D. C. Burnham and D. L. Weinberg, *Observation of Simultaneity in Parametric Production of Optical Photon Pairs*, Physical Review Letters, **25**, pp. 84–87 (1970).

[79] M. Fiorentino, P. Voss, J. Sharping, and P. Kumar, *All-fiber photon-pair source for quantum communications*, Photonics Technology Letters, IEEE, **14**, pp. 983–985 (2002).

[80] J. Sharping, J. Chen, X. Li, P. Kumar, and R. Windeler, *Quantum-correlated twin photons from microstructure fiber*, Opt. Express, **12**, pp. 3086–3094 (2004).

[81] X. Li, J. Chen, P. Voss, J. Sharping, and P. Kumar, *All-fiber photon-pair source for quantum communications: Improved generation of correlated photons*, Opt. Express, **12**, pp. 3737–3744 (2004).

[82] J. Fan, A. Migdall, and L. J. Wang, *Efficient generation of correlated photon pairs in a microstructure fiber*, Opt. Lett., **30**, pp. 3368–3370 (2005).

[83] A. Y. H. Chen, G. K. L. Wong, S. G. Murdoch, R. Leonhardt, J. D. Harvey, J. C. Knight, W. J. Wadsworth, and P. S. J. Russell, *Widely tunable optical parametric generation in a photonic crystal fiber*, Opt. Lett., **30**, pp. 762–764 (2005).

[84] J. Rarity, J. Fulconis, J. Duligall, W. Wadsworth, and P. Russell, *Photonic crystal fiber source of correlated photon pairs*, Opt. Express, **13**, pp. 534–544 (2005).

[85] J. Fulconis, O. Alibart, W. Wadsworth, P. Russell, and J. Rarity, *High brightness single mode source of correlated photon pairs using a photonic crystal fiber*, Opt. Express, **13**, pp. 7572–7582 (2005).

[86] O. Alibart, J. Fulconis, G. K. L. Wong, S. G. Murdoch, W. J. Wadsworth, and J. G. Rarity, *Photon pair generation using four-wave mixing in a microstructured fibre: theory versus experiment*, New Journal of Physics, **8**, p. 67 (2006).

[87] X. Li, P. L. Voss, J. E. Sharping, and P. Kumar, *Optical-Fiber Source of Polarization-Entangled Photons in the 1550 nm Telecom Band*, Physical Review Letters, **94**, pp. 053601–4 (2005).

[88] J. Fan, M. D. Eisaman, and A. Migdall, *Bright phase-stable broadband fiber-based source of polarization-entangled photon pairs*, Physical Review A (Atomic, Molecular, and Optical Physics), **76**, 043836 (2007).

[89] J. Fulconis, O. Alibart, J. L. O'Brien, W. J. Wadsworth, and J. G. Rarity, *Nonclassical Interference and Entanglement Generation Using a Photonic Crystal Fiber Pair Photon Source*, Physical Review Letters, **99**, 120501 (2007).

[90] J. F. et al, *Quantum interference with photon pairs using two micro-structured fibres*, New Journal of Physics, **9**, 276 (2007).

[91] J. Chen, J. Fan, M. D. Eisaman, and A. Migdall, *Generation of high-flux hyperentangled photon pairs using a microstructure-fiber Sagnac interferometer*, Physical Review A (Atomic, Molecular, and Optical Physics), **77**, pp. 053812–5 (2008).

[92] A. B. U'Ren, C. Silberhorn, K. Banaszek, I. A. Walmsley, R. Erdmann, W. P. Grice, and M. G. Raymer, *Generation of pure-state single-photon wavepackets by conditional preparation based on spontaneous parametric downconversion*, Laser Physics, **15**, pp. 146–161 (2005).

[93] P. J. Mosley, J. S. Lundeen, B. J. Smith, P. Wasylczyk, A. B. U'Ren, C. Silberhorn, and I. A. Walmsley, *Heralded Generation of Ultrafast Single Photons in Pure Quantum States*, Physical Review Letters, **100**, 133601 (2008).

[94] P. J. Mosley, J. S. Lundeen, B. J. Smith, and I. A. Walmsley, *Focusing on factorability: space-time coupling in the generation of pure heralded single photons*, Journal of Modern Optics, **56**, pp. 179–189 (2009).

[95] R. W. Boyd, *Nonlinear Optics*, Academic Press, second edition (2003).

[96] R. J. Glauber, *Coherent and Incoherent States of the Radiation Field*, Physical Review, **131**, pp. 2766–2788 (1963).

[97] K. Garay-Palmett, H. J. McGuinness, O. Cohen, J. S. Lundeen, R. Rangel-Rojo, A. B. U'ren, M. G. Raymer, C. J. McKinstrie, S. Radic, and I. A. Walmsley, *Photon pair-state preparation with tailored spectral properties by spontaneous four-wave mixing in photonic-crystal fiber*, Opt. Express, **15**, pp. 14870–14886 (2007).

[98] W. P. Grice and I. A. Walmsley, *Spectral information and distinguishability in type-II down-conversion with a broadband pump*, Physical Review A, **56**, pp. 1627–1634 (1997).

[99] A. B. U'Ren, K. Banaszek, and I. A. Walmsley, *Photon engineering for quantum information processing*, QUANTUM INFORMATION AND COMPUTATION, **3**, p. 480 (2003).

[100] A. Yariv, *Optical Electronics in Modern Communications*, Oxford University Press, fifth edition (1997).

[101] N. Mortensen, J. Folken, P. Skovgaard, and J. Broeng, *Numerical aperture of single-mode photonic crystal fibers*, Photonics Technology Letters, IEEE, **14**, pp. 1094–1096 (2002).

[102] G. K. Wong, A. Y. Chen, S. Ha, R. Kruhlak, S. Murdoch, R. Leonhardt, J. Harvey, and N. Joly, *Characterization of chromatic dispersion in photonic crystal fibers using scalar modulation instability*, Opt. Express, **13**, pp. 8662–8670 (2005).

[103] R. Stolen and J. Bjorkholm, *Parametric amplification and frequency conversion in optical fibers*, Quantum Electronics, IEEE Journal of, **18**, pp. 1062–1072 (1982).

[104] A. K. Angelow and P. P. Kircheva, *Tunable four-wave mixing in low-mode-number optical fibers*, Appl. Opt., **33**, pp. 3203–3208 (1994).

[105] H. Tu, Z. Jiang, D. L. Marks, and S. A. Boppart, *Intermodal four-wave mixing from femtosecond pulse-pumped photonic crystal fiber*, Applied Physics Letters, **94**, pp. 101109–3 (2009).

[106] J. D. Harvey, R. Leonhardt, S. Coen, G. K. L. Wong, J. Knight, W. J. Wadsworth, and P. St. J. Russell, *Scalar modulation instability in the normal dispersion regime by use of a photonic crystal fiber*, Opt. Lett., **28**, pp. 2225–2227 (2003).

[107] B. Ainslie and C. Day, *A review of single-mode fibers with modified dispersion characteristics*, Lightwave Technology, Journal of, **4**, pp. 967–979 (1986).

[108] J. C. Knight, T. A. Birks, P. S. J. Russell, and D. M. Atkin, *All-silica single-mode optical fiber with photonic crystal cladding*, Opt. Lett., **21**, pp. 1547–1549 (1996).

[109] P. Russell, *Photonic Crystal Fibers*, Science, **299**, pp. 358–362 (2003).

[110] J. C. Knight, T. A. Birks, P. S. J. Russell, and J. P. de Sandro, *Properties of photonic crystal fiber and the effective index model*, J. Opt. Soc. Am. A, **15**, pp. 748–752 (1998).

[111] R. J. Kruhlak, G. K. Wong, J. S. Chen, S. G. Murdoch, R. Leonhardt, J. D. Harvey, N. Y. Joly, and J. C. Knight, *Polarization modulation instability in photonic crystal fibers*, Opt. Lett., **31**, pp. 1379–1381 (2006).

[112] G. P. Agrawal, *Nonlinear Fiber Optics*, Elsevier, fourth edition (2007).

[113] I. H. Malitson, *Interspecimen Comparison of the Refractive Index of Fused Silica*, J. Opt. Soc. Am., **55**, pp. 1205–1208 (1965).

[114] C. V. Raman and K. S. Krishnan, *A New Type of Secondary Radiation*, Nature, **121**, pp. 501–502 (1928).

[115] R. H. Stolen and E. P. Ippen, *Raman gain in glass optical waveguides*, Applied Physics Letters, **22**, pp. 276–278 (1973).

[116] Q. Lin, F. Yaman, and G. P. Agrawal, *Photon-pair generation in optical fibers through four-wave mixing: Role of Raman scattering and pump polarization*, Physical Review A (Atomic, Molecular, and Optical Physics), **75**, pp. 023803–20 (2007).

[117] K. F. Lee, J. Chen, C. Liang, X. Li, P. L. Voss, and P. Kumar, *Generation of high-purity telecom-band entangled photon pairs in dispersion-shifted fiber*, Opt. Lett., **31**, pp. 1905–1907 (2006).

[118] S. D. Dyer, M. J. Stevens, B. Baek, and S. W. Nam, *High-efficiency, ultra low-noise all-fiber photon-pair source*, Opt. Express, **16**, pp. 9966–9977 (2008).

[119] S. D. Dyer, B. Baek, and S. W. Nam, *High-brightness, low-noise, all-fiber photon pair source*, Opt. Express, **17**, pp. 10290–10297 (2009).

[120] R. H. Stolen, J. E. Bjorkholm, and A. Ashkin, *Phase-matched three-wave mixing in silica fiber optical waveguides*, Applied Physics Letters, **24**, pp. 308–310 (1974).

[121] R. Stolen, *Phase-matched-stimulated four-photon mixing in silica-fiber waveguides*, Quantum Electronics, IEEE Journal of, **11**, pp. 100–103 (1975).

[122] R. H. Stolen, M. A. Bosch, and C. Lin, *Phase matching in birefringent fibers*, Opt. Lett., **6**, p. 213 (1981).

[123] C. Söller, B. Brecht, P. J. Mosley, L. Y. Zang, A. Podlipensky, N. Y. Joly, P. S. J. Russell, and C. Silberhorn, *Bridging visible and telecom wavelengths with a single-mode broadband photon pair source*, Physical Review A, **81**, p. 031801 (2010).

[124] S. G. Murdoch, R. Leonhardt, and J. D. Harvey, *Polarization modulation instability in weakly birefringent fibers*, Opt. Lett., **20**, pp. 866–868 (1995).

[125] J. Fan and A. Migdall, *Generation of cross-polarized photon pairs in a microstructure fiber with frequency-conjugate laser pump pulses*, Opt. Express, **13**, pp. 5777–5782 (2005).

[126] O. Cohen, J. S. Lundeen, B. J. Smith, G. Puentes, P. J. Mosley, and I. A. Walmsley, *Tailored Photon-Pair Generation in Optical Fibers*, Physical Review Letters, **102**, pp. 123603–4 (2009).

[127] M. Halder, J. Fulconis, B. Cemlyn, A. Clark, C. Xiong, W. J. Wadsworth, and J. G. Rarity, *Nonclassical 2-photon interference with separate intrinsically narrowband fibre sources*, Opt. Express, **17**, pp. 4670–4676 (2009).

[128] Crystal Fibres, *personal communication.*

[129] A. Ling, J. Chen, J. Fan, and A. Migdall, *Mode expansion and Bragg filtering for a high-fidelity fiber-based photon-pair Source*, Opt. Express, **17**, pp. 21302–21312 (2009).

[130] B. J. Smith, P. Mahou, O. Cohen, J. S. Lundeen, and I. A. Walmsley, *Photon pair generation in birefringent optical fibers*, Opt. Express, **17**, pp. 23589–23602 (2009).

[131] B. J. Smith, D. Kundys, N. Thomas-Peter, P. G. R. Smith, and I. A. Walmsley, *Phase-controlled integrated photonic quantum circuits*, Opt. Express, **17**, pp. 13516–13525 (2009).

[132] G. D. Marshall, A. Politi, J. C. F. Matthews, P. Dekker, M. Ams, M. J. Withford, and J. L. O'Brien, *Laser written waveguide photonic quantum circuits*, Opt. Express, **17**, pp. 12546–12554 (2009).

[133] J. C. F. Matthews, A. Politi, StefanovAndre, and J. L. O'Brien, *Manipulation of multiphoton entanglement in waveguide quantum circuits*, Nat Photon, **3**, pp. 346–350 (2009).

[134] W. Wasilewski, A. I. Lvovsky, K. Banaszek, and C. Radzewicz, *Pulsed squeezed light: Simultaneous squeezing of multiple modes*, Physical Review A (Atomic, Molecular, and Optical Physics), **73**, pp. 063819–12 (2006).

[135] C. Śliwa and K. Banaszek, *Conditional preparation of maximal polarization entanglement*, Phys. Rev. A, **67**, p. 030101 (2003).

[136] A. E. B. Nielsen and K. Mølmer, *Conditional generation of path-entangled optical* $|N, 0> + |0, N>$ *states*, Physical Review A (Atomic, Molecular, and Optical Physics), **75**, 063803 (2007).

[137] P. Walther, M. Aspelmeyer, and A. Zeilinger, *Heralded generation of multiphoton entanglement*, Physical Review A (Atomic, Molecular, and Optical Physics), **75**, 012313 (2007).

[138] J. Eisert, D. E. Browne, S. Scheel, and M. B. Plenio, *Distillation of continuous-variable entanglement with optical means*, Annals of Physics, **311**, pp. 431–458 (2004).

[139] J. Eisert, M. Plenio, D. Browne, S. Scheel, and A. Feito, *On the experimental feasibility of continuous-variable optical entanglement distillation*, Optics and Spectroscopy, **103**, pp. 173–177 (2007).

[140] H. Takahashi, J. S. Neergaard-Nielsen, M. Takeuchi, M. Takeoka, K. Hayasaka, A. Furusawa, and M. Sasaki, *Entanglement distillation from Gaussian input states*, Nat Photon, **4**, pp. 178–181 (2010).

[141] M. Fiorentino, S. M. Spillane, R. G. Beausoleil, T. D. Roberts, P. Battle, and M. W. Munro, *Spontaneous parametric down-conversion in periodically poled KTP waveguides and bulk crystals*, Opt. Express, **15**, pp. 7479–7488 (2007).

[142] J. D. Bierlein, D. B. Laubacher, J. B. Brown, and C. J. van der Poel, *Balanced phase matching in segmented $KTiOPO_4$ waveguides*, Applied Physics Letters, **56**, pp. 1725–1727 (1990).

[143] C. J. van der Poel, J. D. Bierlein, J. B. B. Co., and S. Colak, *Efficient type I blue second-harmonic generation in periodically segmented $KTiOPO_4$ waveguides*, Applied Physics Letters, **57**, pp. 2074–2076 (1990).

[144] M. C. Booth, M. Atatüre, G. Di Giuseppe, B. E. A. Saleh, A. V. Sergienko, and M. C. Teich, *Counterpropagating entangled photons from a waveguide with periodic nonlinearity*, Physical Review A, **66**, 023815 (2002).

[145] A. Christ, A. Eckstein, P. J. Mosley, and C. Silberhorn, *Pure single photon generation by type-I PDC with backward-wave amplification*, Opt. Express, **17**, pp. 3441–3446 (2009).

[146] S. G. Murdoch, R. Leonhardt, J. D. Harvey, and T. A. B. Kennedy, *Quasi-phase matching in an optical fiber with periodic birefringence*, J. Opt. Soc. Am. B, **14**, pp. 1816–1822 (1997).

[147] Z. H. Levine, J. Fan, J. Chen, A. Ling, and A. Migdall, *Heralded, pure-state single-photon source based on a Potassium Titanyl Phosphate waveguide*, Opt. Express, **18**, pp. 3708–3718 (2010).